

Development of an On-Chip Microfluidic Model of Human Cardiac Tissue as a Platform
for the Study of Cardiovascular Diseases

by

Jaimeson Veldhuizen

A Dissertation Presented in Partial Fulfillment of
the Requirements for the Degree
Doctor of Philosophy

Approved November 2021 by the
Graduate Supervisory Committee:

Mehdi Nikkhah, Chair
David Brafman
Mo Ebrahimkhani
Raymond Migrino
Christopher Plaisier

ARIZONA STATE UNIVERSITY

December 2021

ABSTRACT

Cardiovascular disease (CVD) remains the leading cause of mortality, resulting in 1 out of 4 deaths in the United States at the alarming rate of 1 death every 36 seconds, despite great efforts in ongoing research. In vitro research to study CVDs has had limited success, due to lack of biomimicry and structural complexity of 2D models. As such, there is a critical need to develop a 3D, biomimetic human cardiac tissue within precisely engineered in vitro platforms. This PhD dissertation involved development of an innovative anisotropic 3D human stem cell-derived cardiac tissue on-a-chip model (i.e., heart on-a-chip), with an enhanced maturation tissue state, as demonstrated through extensive biological assessments. To demonstrate the potential of the platform to study cardiac-specific diseases, the developed heart on-a-chip was used to model myocardial infarction (MI) due to exposure to hypoxia. The successful induction of MI on-a-chip (heart attack-on-a-chip) was evidenced through fibrotic tissue response, contractile dysregulation, and transcriptomic regulation of key pathways.

This dissertation also described incorporation of CRISPR/Cas9 gene-editing to create a human induced pluripotent stem cell line (hiPSC) with a mutation in *KCNH2*, the gene implicated in Long QT Syndrome Type 2 (LQTS2). This novel stem cell line, combined with the developed heart on-a-chip technology, led to creation of a 3D human cardiac on-chip tissue model of LQTS2 disease.. Extensive mechanistic biological and electrophysiological characterizations were performed to elucidate the mechanism of R531W mutation in *KCNH2*, significantly adding to existing knowledge about LQTS2. In summary, this thesis described creation of a LQTS2 cardiac on-a-chip model,

incorporated with gene-edited hiPSC-cardiomyocytes and hiPSC-cardiac fibroblasts, to study mechanisms of LQTS2.

Overall, this dissertation provides broad impact for fundamental studies toward cardiac biological studies as well as drug screening applications. Specifically, the developed heart on-a-chip from this dissertation provides a unique alternative platform to animal testing and 2D studies that recapitulates the human myocardium, with capabilities to model critical CVDs to study disease mechanisms, and/or ultimately lead to development of future therapeutic strategies.

DEDICATION

To my loving and encouraging boyfriend, Elliott. I thank you for being so amazing these past years and for your endless support.

To my amazing family. I thank you for always being there for me and supporting me throughout these years. You have all provided an unbelievable support system that I have been beyond blessed to have.

ACKNOWLEDGEMENTS

I would like to acknowledge my doctoral advisor and committee chair, Dr. Mehdi Nikkhah. He has consistently supported my decisions throughout my doctoral research, providing great assistance to overcome the project challenges. I am grateful for his guidance, patience, and compassion throughout these years.

I would like to acknowledge my doctoral committee members: Dr. David Brafman, Dr. Mo Ebrahimkhani, Dr. Raymond Q. Migrino, and Dr. Christopher Plaisier, for graciously spending time with me to discuss my research plans and to provide invaluable advice and guidance. I would also like to acknowledge the SBHSE staff in their support and encouragements throughout the years.

I would like to thank all of the friends I have made, both my fellow lab members, as well as members in adjacent labs and fellow graduate students, who I am thankful to for the friendship and support over the years.

Lastly, I would like to acknowledge the funding sources: National Science Foundation CAREER Award #1653193, Flinn Foundation, 2021 Achievement Rewards for College Scientists Scholarship, and funding from ASU Graduate & Professional Student Association, the ASU Graduate College, and School of Biological and Health Systems Engineering.

TABLE OF CONTENTS

	Page
LIST OF FIGURES.....	viii
PREFACE.....	x
CHAPTER	
1 INTRODUCTION.....	1
1.1 Cardiovascular Disease.....	1
1.2 Animal and Animal-derived Models for Cardiac Research.....	4
1.3 Human PSC-CMs (Pluripotent Stem Cell-Cardiomyocytes) in 2D Monolayer Assays.....	8
1.4 Microengineering of 3D Cardiac Tissue Models.....	12
1.5 Application of 3D Microengineered Cardiac Tissues for Disease Modeling..	19
1.6 Thesis Aims and Overview.....	25
2 AIM 1: DEVELOP A NOVEL MICROFLUIDIC HEART ON-A-CHIP PLATFORM AND OPTIMIZE 3D CARDIAC TISSUE FORMATION WITH BOTH RAT-DERIVED AND HUMAN STEM CELL-DERIVED CARDIAC CELLS.....	28
2.1 Abstract.....	28
2.2 Introduction.....	29
2.3 Methods.....	35
2.4 Results and Discussion.....	44
2.5 Conclusion.....	68

CHAPTER	Page
3	AIM 2: INCORPORATE THE OPTIMIZED MICROFLUIDIC PLATFORM TO CREATE A MODEL OF CARDIAC ISCHEMIA ON-A-CHIP TO INVESTIGATE CELLULAR AND MOLECULAR RESPONSE OF MYOCARDIAL TISSUE UNDER HYPOXIA.....70
	3.1 Abstract.....70
	3.2 Introduction.....70
	3.3 Materials and Methods.....77
	3.4 Results.....87
	3.5 Discussion.....103
	3.6 Conclusion.....107
4	AIM 3: CREATE AN HIPSC LINE WITH A KCNH2 MUTATION, USING CRISPR/CAS9 GENE-EDITING, AND MODEL LONG QT SYNDROME TYPE 2 ON-A-CHIP WITHIN DEVELOPED MICROFLUIDIC PLATFORM.....109
	4.1 Abstract.....109
	4.2 Introduction.....110
	4.3 Materials and Methods.....116
	4.4 Results.....126
	4.5 Discussion.....140
	4.6 Conclusion.....142
5	CONCLUSIONS AND FUTURE DIRECTIONS.....144

CHAPTER	Page
5.1 Significance and Contributions.....	144
5.2 Project Challenges.....	149
5.3 Future Directions.....	151
REFERENCES.....	155
APPENDIX	
A SUPPLEMENTARY FIGURES FOR CHAPTER 2.....	183
B SUPPLEMENTARY FIGURES FOR CHAPTER 3.....	193
C SUPPLEMENTARY FIGURES FOR CHAPTER 4.....	197
D LIST OF SUPPLEMENTARY VIDEOS.....	200
E LIST OF SUPPLEMENTARY TABLES.....	202
F COPYRIGHT PERMISSIONS.....	204

LIST OF FIGURES

Figure	Page
1.1 Schematic of Healthy Adult Myocardium and Platforms Implemented for Cardiac Tissue Modeling.....	3
1.2 Three-dimensional Microengineered Models of Healthy Cardiac Tissue.....	14
1.3 Three-dimensional Microengineered Models of Cardiac Diseases.....	24
2.1 Microfluidic Device for 3D Cardiac Tissue Modeling.....	47
2.2 Optimization of Microfluidic Device Design Parameters with Neonatal Rat Cardiac Cells.....	50
2.3 Characterization of Cardiomyocytes (CMs) Differentiated from Both hESCs and hiPSCs.....	52
2.4 Structural Properties of Human Stem Cell-derived Cardiac Tissues Formed Within Microfluidic Devices with and without the Microposts.....	57
2.5 Gene Expression Analysis of Human Stem Cell-derived Cardiac Tissues in Monolayer and Microfluidic Devices.....	60
2.6 Comparison of Tissues Cultured in Devices with and Without Microposts.....	62
2.7 Functional Assessment of Human Stem Cell-derived Cardiac Tissues Within Devices with and Without Posts After 14 Days of Culture.....	66
3.1 Experimental Schematic of Modeling Myocardial Ischemia Within Microfluidic Device Platform and Formation of Aligned Cardiac Tissue Before Disease Modeling.....	77

Figure	Page
3.2 Viability and Alignment Assessment of Cardiac Tissues After Exposure to Varying Oxygen Levels.....	88
3.3 Assessment of Fibrotic Response in 3D Tissues Exposed to the Varying Oxygen Levels.....	90
3.4 Resultant Functional and Gene Expression Analysis of 3D Cardiac Tissues After Exposure to Different Oxygen Levels.....	96
3.5 Transcriptomic Analysis of Physioxic and Hypoxic Tissues.....	99
3.6 Visualization of Significant Genes Among Enriched Terms from Transcriptomic Analysis.....	101
3.7 Cardiac Tissue Response to Acute and Extended Reperfusion.....	103
4.1 Schematic of hERG Channel Structure. Overview of the Design of sgRNAs, hiPSC Transfection, and hiPSC Differentiation.....	128
4.2 Creation and Validation of hiPSCs with R531W Mutation in KCNH2.....	131
4.3 Characterization of Isogenic Cardiac Cells Differentiated from WT and Edited hiPSCs.....	133
4.4 Trafficking of hERG in Cardiomyocytes Differentiated from hiPSCs with R531W Mutation in KCNH2.....	135
4.5 Development of Long QT Syndrome Type 2 on-a-Chip.....	136
4.6 Pharmaceutical Testing of Long QT Syndrome Type 2 on-a-Chip.....	140

PREFACE

The dissertation herein includes original review and research articles prepared and published by the primary author. Chapter 1 details an introduction and background to the material of this thesis (Veldhuizen, Migrino, & Nikkhah, 2019). Chapter 2 details the creation of a microfluidic chip with innate microposts to establish cardiac tissue anisotropy for the formation of mature cardiac tissues (Veldhuizen, Cutts, Brafman, Migrino, & Nikkhah, 2020). Chapter 3 describes the use of the microfluidic model to study myocardial ischemia via induction of hypoxia. Chapter 4 describes the combination of gene-editing techniques within the microfluidic chip to create model of Long QT Syndrome Type 2.

CHAPTER 1

INTRODUCTION

1.1 Cardiovascular Disease

Cardiovascular diseases (CVDs) persist as the leading cause of mortality and morbidity, accounting for over 30% of deaths worldwide (Benjamin, 2017). Notably, CVDs have become the most expensive chronic disease in the United States, with \$318 billion in total direct medical costs in 2015 (Khavjou, 2016). Additionally, it is predicted that 45.1% of the U.S. population will suffer from CVDs by 2035 (Khavjou, 2016). Current research strategies employed in healthcare (e.g., pharmaceutical) industries to study CVDs and to develop new therapeutic drugs mainly involve conventional two-dimensional (2D) *in vitro* models, such as monoculture cellular assays, as well as *in vivo* animal models. However, these models have significant limitations in recapitulating human pathophysiology. 2D *in vitro* models are limited in simulating the pathophysiology of CVDs due to the high degree of complexity in structure and function of the myocardium. Specifically, these assays are unable to precisely recapitulate the complex cell-extracellular matrix (ECM), cell-cell, and tissue-level interactions. To address limitations in 2D assays, animal (e.g., mouse) models have been utilized as they are capable of complex tissue-level representation. To that end, we now have a greater understanding of the differences between mouse models and human disease, including alterations in gene expression that may affect translation of preclinical findings to human benefit (Blalock et al., 2005). However, there are many confounding factors involved in

animal models, imposing challenges with transferring disease-related knowledge from these models into human pharmaceutical testing (Rajamohan et al., 2013).

To improve therapeutic outcomes from CVDs, attempts at addressing limitations of current 2D and animal models include creation of intricate three-dimensional (3D) cardiac tissue constructs with enhanced recapitulation of native myocardium that are useful for mechanistic studies, therapeutic discovery, and testing (Acun, Vural, & Zorlutuna, 2017; Agarwal, Goss, Cho, McCain, & Parker, 2013; Alford, Feinberg, Sheehy, & Parker, 2010; Annabi, Selimovic, et al., 2013; Birla, Borschel, Dennis, & Brown, 2005; Boudou et al., 2012; Breckwoldt et al., 2017; L. L. Chiu, Janic, & Radisic, 2012; L. L. Y. Chiu & Radisic, 2013; Ellis, Acun, Can, & Zorlutuna, 2017; Engelmayr et al., 2008; Feinberg et al., 2012; Ghiaseddin et al., 2017; Lee, Razu, Wang, Lacerda, & Kim, 2015; Leung & Sefton, 2010; Mannhardt et al., 2016; Mathur et al., 2013; Mathur et al., 2015; Nunes et al., 2013; Pavesi et al., 2015; Radisic et al., 2006; Saini, Navaei, Van Putten, & Nikkhah, 2015; Sidorov et al., 2017; Tiburcy et al., 2017; Vandeburgh et al., 2008; G. Wang et al., 2014; D. Zhang et al., 2013). To date, a variety of techniques to create 3D cardiac tissue models have been proposed, each presenting with advantages over currently available models, including incorporation of highly controllable environments for cellular- and molecular-level studies. Recent *in vitro* research has also advanced the use of human-derived cardiac cells, made possible by wide availability of methods for cardiac differentiation of human stem cells to generate patient-specific and genetically-edited cardiac cells (Ameen et al., 2008). Additionally, significant emphasis on emerging biomaterials and micro-/nano- scale technologies has opened new

opportunities to enhance the functionalities of engineered cardiac tissues through precise control over cell-cell and cell-ECM interactions (Annabi, Tsang, et al., 2013; Nikkhah, Edalat, Manoucheri, & Khademhosseini, 2012; Saini et al., 2015). These models also incorporate intricacies of the native myocardium, including mimicry of anisotropic structure and accommodation of electrical and mechanical stimulation. Notably, 3D microengineered cardiac tissue models have been successfully utilized (Figure 1.1) to better understand the biological basis of disease progression and enhance the efficacy of pharmaceutical testing of candidate therapeutics.

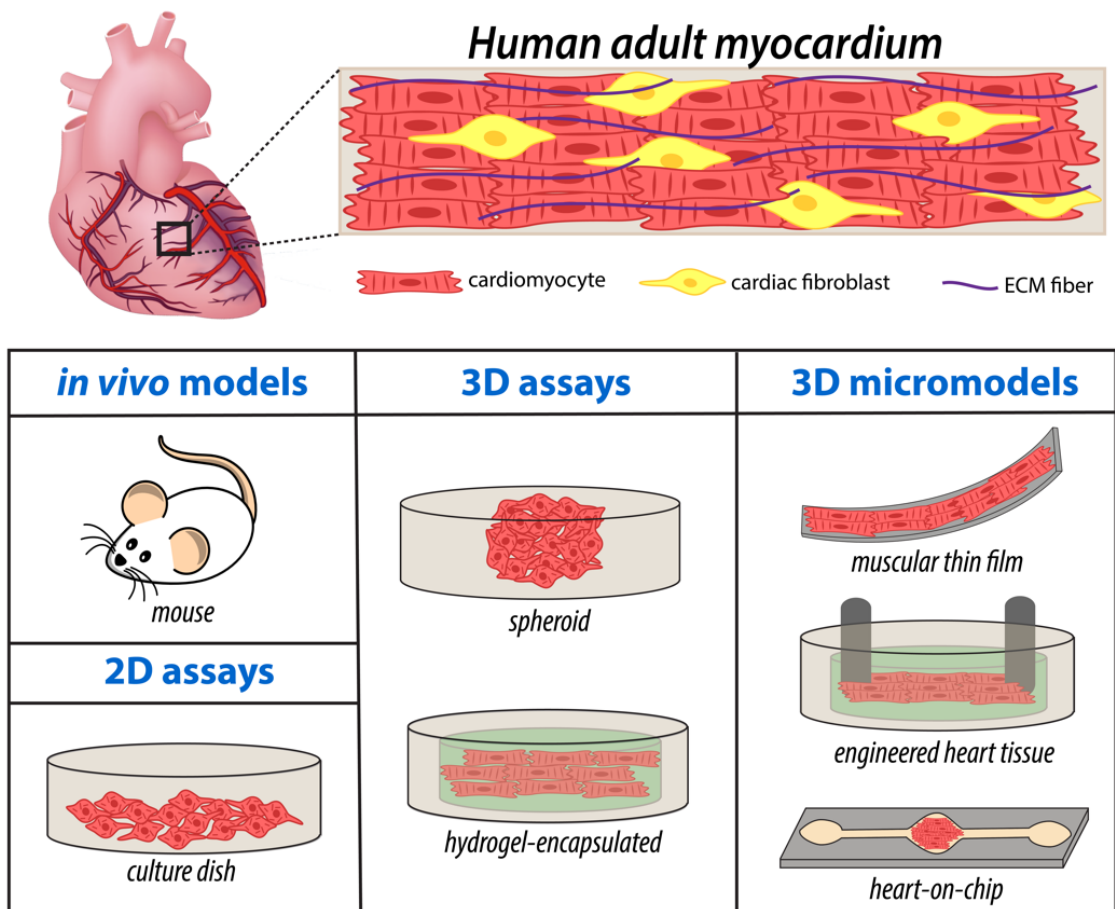


Figure 1.1: Schematic of healthy adult myocardium and examples of the different platforms implemented for cardiac tissue modeling.

In this chapter, we provide a brief assessment of conventional 2D assays and animal models that have been utilized for cardiac-related disease studies. We will further review the recent progress in microengineering technologies to create 3D cardiac tissue models. A summary of current 3D diseased cardiac tissue models, with specific advantages for mechanistic biological studies and therapeutic testing, will also be provided.

1.2 Animal and animal-derived models for cardiac research

1.2.1 In vivo models

The most implemented approach for subsequent studies of CVDs is through animal models (Brooks & Conrad, 2009; Duncker et al., 2015; Hofker, van Vlijmen, & Havekes, 1998; Y. B. Liu et al., 2003; McCauley & Wehrens, 2009; McLerie, 2003; Patten & Hall-Porter, 2009; Pilichou, Bezzina, Thiene, & Basso, 2011; Stengl, 2010; Stohr et al., 2013; Zaragoza et al., 2011). Such models range from small to large animals, and incorporate a variety of both environmentally and genetically derived diseases, to study corresponding cardiac pathophysiology. Specifically, environmentally-related diseases can be studied in animal models by delivery of physical, chemical, or metabolic insults, such as through extreme change in diet or chemical administration (Kumar et al., 2016; McCauley & Wehrens, 2009; Zaragoza et al., 2011). Particularly, the use of animal models to study environmentally-related diseases is advantageous in the ability to recapitulate whole organ-level response to such systemic insults, an aspect that is lacking in current *in vitro* models. For example, to model myocardial infarction (MI), Brooks et al. chronically administered isoproterenol to mice to induce MI-related symptoms, such as impairment of diastolic function and changes in heart size, allowing for study of

disease manifestation and related secondary injuries (Brooks & Conrad, 2009). Additionally, to model acute MI, left coronary artery (LCA) ligation has been established as a technique for arterial occlusion to induce myocardial infarction in multiple types of animal models (Kumar et al., 2016). Gao et. al. utilized this method to study heart remodeling and secondary pathways that occur after ligation-induced MI in mice. Significant alterations in echocardiographic characteristics, in addition to heart size and weight, were demonstrated in mice that experienced MI, thus demonstrating capabilities of animal models for systemic-level pathophysiology (Gao, Dart, Dewar, Jennings, & Du, 2000). On the other hand, the use of transgenic animal models allows the study of genetically-derived diseases to elucidate the role of specific genes in manifestation of corresponding pathology, and potential responses to pharmaceuticals. For example, to study atherothrombotic disease, transgenic mice with mutant apolipoprotein-E have been used to recapitulate the lipoprotein profile observed in hyperlipidemia patients, causing atherosclerotic lesions to develop (Hofker et al., 1998).

A particular advantage of use of animal models for study of CVDs is the ability to study diseases with systemic level pathology, and isolate the corresponding effects on cardiac function. For example, Fulop et. al. incorporated Zucker diabetic fatty (ZDF) rats to determine if development of Type 2 diabetes negatively affects CM function (Fulop et al., 2007). Their findings unveiled that contraction, relaxation, and calcium handling characteristics were impaired for CMs isolated from 22 week-old hyperglycemic ZDF rats as compared to both 6-week old hyperinsulinemic ZDF rats and healthy age-matched

controls. Thus, the use of the ZDF rat models delineated specific cardiac-related effects of diabetes.

In vivo animal models have provided fundamental knowledge into the biology of cardiac disease, and correspondingly have served as helpful models for the translation of observed pathology into potential pharmaceuticals (Brooks & Conrad, 2009; Duncker et al., 2015; Hofker et al., 1998; Y. B. Liu et al., 2003; McCauley & Wehrens, 2009; McLerie, 2003; Patten & Hall-Porter, 2009; Pilichou et al., 2011; Stengl, 2010; Stohr et al., 2013; Zaragoza et al., 2011). However, the inability for precise control at molecular and cellular levels hampers the amount of mechanistic information that can be gained from these models. Incorporation of cardiac tissues within *in vitro* models has enabled the direct mechanistic studies of CVDs that complement the knowledge gained from *in vivo* models for enhanced clinical translation of disease-related findings.

1.2.2 Neonatal rat cardiomyocytes in in vitro models

There have been a vast number of *in vitro* models to date utilizing neonatal CMs derived from animals for cardiac tissue engineering due to the ease of access and availability of these cells (Annabi, Tsang, et al., 2013; M. Kharaziha et al., 2013; M. S. Kharaziha, S.; Nikkhah, M.; Topkaya, S. N. ; Masoumi, N.; Dokmeci, M. R. ; Khademhosseini, A., 2014; Navaei et al., 2017; Navaei, Truong, et al., 2016; Rashid, Salacinski, Hamilton, & Seifalian, 2004; Saini et al., 2015; Zimmermann et al., 2002). For example, Zimmermann et. al. demonstrated the utility of mechanical stretch in an *in vitro* model to generate aligned cardiac tissue from neonatal rat CMs and collagen hydrogel that resembles the structure of the native myocardium (Zimmermann et al.,

2002). Saini et. al. developed cardiac micro-tissues, with variable geometrical features and CMs to cardiac fibroblast (CFs) ratios within gelatin methacrylate (GelMA) hydrogel, to assess the role of tissue confinement and cell ratios on the functionalities of the engineered tissues (Saini et al., 2015). Their findings demonstrated that supplementation of CMs with CFs enhanced the tissue structure and protein expression, in addition to the observation of the prominent role of surface topography on tissue formation. These *in vitro* models have also been advanced for elaborate cardiac tissue studies, with an emphasis on modeling CVDs (Ariyasinghe et al., 2017; He, Ma, Liu, & Wang, 2014; Horton et al., 2016; Katare, Ando, Kakinuma, & Sato, 2010; McCain, Sheehy, Grosberg, Goss, & Parker, 2013; Mosadegh et al., 2014; Parsa, Wang, & Vunjak-Novakovic, 2017; L. Ren et al., 2013; Sadeghi et al., 2017; Song, Zandstra, & Radisic, 2011; Spencer et al., 2016; van Spreeuwel et al., 2017). For example, Mosadegh et. al. created a 3D model for cardiac ischemia using rat neonatal CMs within a paper-based platform (Mosadegh et al., 2014). Incorporation of cell culture within this *in vitro* model allowed for establishment of an oxygen gradient and the subsequent study of its effect on encapsulated tissue. Particularly, CF migration was observed against the oxygen gradient, in response to signaling from CMs, providing pertinent information about the intercellular mechanisms that occur during ischemia. Despite the significance of tissue model systems developed using animal-derived cardiac cells, the discrepancies inherent between animal and human physiology significantly limits the translation of knowledge gained from these studies to implementation into the clinic (Rajamohan et al., 2013). To complement these models, *in vitro* models that provide a tunable microenvironment for

precise biological studies are utilized with incorporation of human-derived cells for further insight into CVD research for translational applications.

1.3 Human PSC-CMs (pluripotent stem cell-cardiomyocytes) in 2D monolayer assays

Due to difficulties inherent in the isolation of human adult cardiomyocytes (CMs), their use within *in vitro* assays to date has been limited. The advent of CM differentiation from human pluripotent stem cells (hPSCs), including induced pluripotent (hiPSCs) and embryonic (hESCs), has introduced a potentially unlimited source of human cardiac cells for use in *in vitro* assays for disease modeling (Braam et al., 2010; Brandao, Tabel, Atsma, Mummery, & Davis, 2017; Guo et al., 2011; Harris et al., 2013; Yokoo et al., 2009; M. T. Zhao et al., 2017). Cardiac diseases arise in one of the following ways: through genetic predisposition, acquired or both. Therefore, methods for disease modeling generally fall into one of the following categories to highlight the different methods of disease induction: 1) either diseased cardiac cells are directly incorporated into these *in vitro* models, or 2) healthy CMs are subjected to external insults to model the role of environmental impact in disease etiology. This chapter will focus on models derived via the former approach, through stem cell-based techniques that allow for derivation of patient-specific and/or genetically-edited cardiac cells for precise modeling of disease manifestation. Specifically, to generate such diseased cardiac cells, hPSCs are generally either reprogrammed from patient-derived fibroblasts, or genetically modified from wild-type (WT) hPSCs, to produce the cells with diseased genotype for CM

differentiation and subsequent incorporation into cardiac models (Denning et al., 2016). In the following sections, the use of these cells within 2D assays will be discussed.

1.3.1: Patient-derived hiPSC-CMs

Patient-derived hiPSC-CMs have provided enormous potential for a wide variety of disease modeling applications (Brandao et al., 2017). Long-QT syndrome (LQTS), a disease characterized by prolonged ventricular repolarization phase, often leads to sudden cardiac death in afflicted patients (Moss A., 2007; Schwartz P., 1975). Moretti et. al. identified a missense mutation (R190Q) in *KCNQ1*, a gene that encodes for ion channels that generate the slow outward potassium current I_{Ks} , among patients with LQTS type 1. In order to elucidate mutation-related mechanisms among afflicted cardiac cells, Moretti obtained skin fibroblasts from LQTS1 patients with this mutation, performed hiPSC reprogramming, and then differentiated these pluripotent cells into CMs. Electrophysiological analysis of these CMs highlighted altered activation and deactivation properties of potassium ion channels. Subsequent stimulation through isoproterenol demonstrated an increase in action potential duration, worsening the pathophenotype in LQTS1. This finding demonstrated a possible relationship between abnormal potassium current channels and onset of sudden cardiac death, corroborating the clinical finding that fatal arrhythmias are preceded by increased sympathetic tone in patients with LQTS1 (D., 2008; Vyas, Hejlik, & Ackerman, 2006). Pretreatment of these cells with propranolol (a nonselective beta-blocker) blunted the effects of isoproterenol, thereby serving to protect these diseased cells from catecholamine-induced

tachyarrhythmia (Moretti et al., 2010). Overall, this study highlighted the utility of patient-derived hiPSC-CMs in mechanistic level studies and potential therapeutic testing.

Pompe disease, a metabolic disorder defined by a mutation in the acid alpha-glucosidase (GAA) gene, results in heart failure in a majority of affected patients by 18 months of age (H. P. Huang et al., 2011). To study the relationship of this mutation with cardiac function, Huang et. al. obtained skin fibroblasts from patients with mutations in GAA, performed hiPSC reprogramming and subsequent CM differentiation, and incorporated these CMs into *in vitro* 2D modeling (H. P. Huang et al., 2011). The patient-derived hiPSC-CMs recapitulated classic Pompe disease phenotypes, such as high levels of glycogen and ultrastructural defects, and responded to administration of recombinant GAA, a treatment commonly prescribed for Pompe disease. However, the CMs failed to exhibit dramatic autophagic abnormalities, a major component of disease pathology in Pompe disease, which could potentially be attributed to absence of a 3D complex structure and microenvironment that exist in native myocardium.

Timothy syndrome (TS) is a specific form of long QT syndrome, a disorder defined by prolonged QT intervals arising from a missense mutation in the L-type calcium channel, $Ca_v1.2$, that leads to arrhythmia (Splawski et al., 2004). Yazawa et. al. derived hiPSC-CMs from TS patients, in junction with *in vitro* 2D culture, in order to study the molecular and cellular level properties of TS (Yazawa et al., 2011). The TS hiPSC-CMs demonstrated abnormal electrophysiological properties, including irregular calcium handling and prolonged action potential duration. To test potential therapies, the researchers supplied Roscovitine, a cycline-dependent kinase inhibitor shown to increase

voltage-dependent inactivation of $Ca_v1.2$ channel, and demonstrated that many of these abnormal characteristics were rescued. Despite these advancements, using patient-derived cells to study a disease makes it difficult to capture all of the various facets of the available disease phenotypes, with great interpatient heterogeneities that render study of mechanisms directly related to a genetic mutation difficult to accomplish.

1.3.2: Genetically-induced diseased hPSC-CMs

To bypass inter-patient heterogeneity and specifically identify the role of certain mutations/genes in disease pathology, gene editing, generally in the form of CRISPR (clustered regularly interspaced short palindromic repeats)/Cas9 technology, has been applied to hPSCs, which are then differentiated into CMs and incorporated into cardiac models for mechanistic investigations (Christdi E., 2018).

Type-2 Ryanodine receptors (RyR2) release calcium through a calcium-induced mechanism in the sarcoplasmic reticulum, and its mutation has been found in a majority of cases of catecholaminergic polymorphic ventricular tachycardia type 1 (CPVT1), with more than 150 associated mutations demonstrated [27]. For instance, Wei et. al. used CRISPR/Cas9 to introduce point mutations in WT RyR2 of hiPSCs, then differentiated these cells into CMs (Wei, Zhang, Clift, Yamaguchi, & Morad, 2018). Calcium handling and spontaneous beating properties were compared of the gene-edited cells to patient-derived hiPSC-CMs with the disease-associated mutation, F2483I. This approach enabled precise study of specific mutations among cells that are isogenic to specifically highlight the role of RyR2 in disease pathology, corroborating similar findings in patient-derived hiPSCs with mutated RyR2.

Additionally, gene editing techniques have been integrated with patient-derived hiPSCs to validate the pathogenicity of a genetic variant, through correction of the iPSCs through genome editing. For example, Liang et. al. derived hiPSC-CMs from patients with Brugada syndrome (BS), a disorder associated with ST-segment elevation that leads to ventricular fibrillation and sudden cardiac death, and analyzed the cardiac pathologies, such as abnormal calcium transients (Liang et al., 2016). To study the implication of the SCN5A variant, CRISPR/Cas9 was used to introduce correct SCN5A into the cells derived from BS patients. Correction of this genetic variant resolved many of the irregularities in the electrical profile of the CMs, such as improved peak-to-peak interval variability, highlighting the importance of this gene in pathological onset.

In summary, animal models and 2D *in vitro* assays constitute appropriate platforms for CVDs research. However, human native myocardium has additional structural and functional complexities, in regard to anisotropic architecture, ECM and cell-cell interactions, that are not replicated by 2D *in vitro* models. Incorporation of higher complexity models that better mimic human myocardium could potentially improve recapitulation of disease pathophysiology. In the next section, we will highlight some of the recent advances in development of 3D biomimetic cardiac tissue models through the use of microengineered technologies and advanced biomaterials.

1.4. Microengineering of 3D cardiac tissue models

There is now increased use of 3D cardiac models that provide greater freedom in complex tissue-level interactions in addition to the incorporation of critical physiologic conditions such as whole-tissue electrical stimulation and establishment of precise

gradients. Specifically, the integration of methods such as photolithography, soft lithography, and 3D printing along with advanced biomaterials and human CMs has enabled the emergence of various biomimetic 3D human cardiac tissue microengineered models (Acun et al., 2017; Agarwal et al., 2013; Alford et al., 2010; Annabi, Selimovic, et al., 2013; Birla et al., 2005; Boudou et al., 2012; Breckwoldt et al., 2017; L. L. Chiu et al., 2012; L. L. Y. Chiu & Radisic, 2013; Ellis et al., 2017; Engelmayer et al., 2008; Feinberg et al., 2012; Ghiaseddin et al., 2017; Horton et al., 2016; Lee et al., 2015; Leung & Sefton, 2010; Mannhardt et al., 2016; Mathur et al., 2013; Mathur et al., 2015; Nunes et al., 2013; Pavesi et al., 2015; Radisic et al., 2006; Saini et al., 2015; Sidorov et al., 2017; Tiburcy et al., 2017; Vandeburgh et al., 2008; G. Wang et al., 2014; D. Zhang et al., 2013). The complexity of these 3D microengineered models continues to advance for further physiological relevance, including methods to induce cardiac tissue maturation through use of co-culture of multiple cell types, incorporation of surface topography, and electrical and/or mechanical stimulation (Besser et al., 2018). Engineered cardiac tissue models within microfluidic platforms have the advantage of providing highly controllable fluid flow to model the vasculature within the native heart, in addition to increased throughput due to significant reduction in necessary reagents and cells through platform miniaturization (Verhulsel et al., 2014). Mathur et. al. incorporated hiPSC-CMs into an ECM-coated straight microfluidic channel, composed of polydimethylsiloxane (PDMS), with bordering arrays of microposts to serve as endothelial-like barriers for nutrient and drug diffusion (Mathur et al., 2015) (Figure 1.2A). To validate the model, therapeutic agents administered via the media channels served to model intravenous drug

administration and expected responses were observed from the aligned hiPSC-CM tissue layer, better modeling the tissue-scale response than other cellular-level studies. Recapitulation of cardiac response in addition to the ability to control external inputs such as drug administration, while measuring relevant output such as contractile response demonstrate the utility of this platform in 3D cardiac tissue modeling.

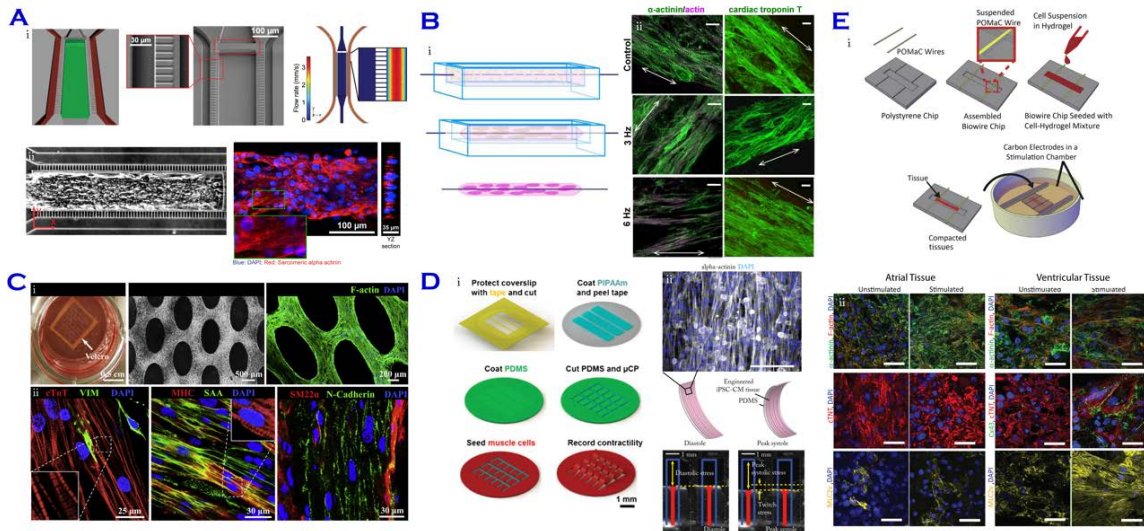


Figure 1.2: Three-dimensional microengineered models of healthy cardiac tissue.

(A) i: Microfluidic channel with endothelial-like borders for cardiac tissue culture. ii: Phase contrast and cardiac-specific marker immunofluorescent staining of cultured tissue within microfluidic platform, reprinted with permission from (Mathur et al., 2015). (B) i: Schematic of cardiac tissue culture around surgical suture. ii: Cardiac-specific marker immunofluorescent staining of tissues with and without electrical stimulation, reprinted with permission from (Nunes et al., 2013). (C) i: Phase contrast and cytoskeletal staining of cardiac tissue formed within engineered patch. ii: Cardiac-specific and other cell-specific marker immunofluorescent staining of 2-week old cardiac tissue patches, reprinted with permission from (D. Zhang et al., 2013). (D) i: Schematic of the process of

engineering MTFs, reprinted with permission from (Agarwal et al., 2013). ii: Cardiac-specific marker immunofluorescent staining of tissues cultured on MTFs and representation of tissue contractility measurements, reprinted with permission from (G. Wang et al., 2014). (E) i: Schematic of process for engineering Biowire II. ii: Cardiac-specific marker immunofluorescent staining of atrial and ventricular tissues, either under electrical stimulation or not, reprinted with permission from (Y. Zhao et al., 2019).

The electrophysiological, phenotypic, and genotypic signatures of CMs generated from differentiation of hPSCs demonstrate the immature state of these cells (Laflamme & Murry, 2011), therefore multiple strategies have been implemented to enhance their maturation to better model adult human cardiac cells. For example, electrical stimulation has been incorporated into 3D microengineered models to allow electrophysiological-related studies, as well as to promote maturation of cardiac tissue (Nunes et al., 2013; Ronaldson-Bouchard et al., 2018). Nunes et. al. cultured 3D hydrogel-encapsulated cardiac tissues along a surgical suture, and supplied electrical field stimulation, through submersion of tissue constructs within an external stimulation chamber, to enhance maturation of the cardiac tissues (Figure 1.2B). Stimulated cardiac tissues displayed greater maturation than their non-stimulated counterparts, as shown by increased myofibril ultrastructural organization and changes in both electrophysiological and calcium handling characteristics. Additionally, the Biowire models responded to physiological activation through β -adrenergic stimulation, as evidenced by increased frequency of spontaneous beating, thereby recapitulating clinical observations of the

native myocardium. These findings demonstrate the usefulness of electrical stimulation to mature hPSC-CM-derived tissue, enhancing the physiological relevance of the model.

Another method to enhance maturation of hPSC-CM tissue is through cellular alignment to mimic the highly anisotropic nature of native myocardium. Zhang et. al., through standard soft lithography, fabricated a tissue-engineered patch with surface topography, in the form of staggered hexagonal microposts of precise spacing and geometry, to induce alignment of hPSC-derived cardiac tissue (D. Zhang et al., 2013) (Figure 1.2C). The aligned, anisotropic structure of the encapsulated cardiac tissue, when compared to monolayers of isotropic tissue of identical cellular composition, demonstrated increased maturity as evidenced by a higher ratio of expressed MLC2v/MLC2a and longer striated sarcomeres. Various other works from this group have also demonstrated the merit of topographical features in creation of physiologically relevant human cardiac tissue constructs with enhanced maturation that better represent the native myocardium (Jackman, Carlson, & Bursac, 2016; Shadrin et al., 2017; D. Zhang et al., 2013).

To better study the functionality of engineered cardiac tissue, methods to allow for measurement of the contractility of the tissue have been explored [19, 40, 47, 52]. One technique, muscular thin films (MTFs), involves the use of a flexible PDMS thin layer that deflects into a 3D formation during contraction of cultured CMs (Denning et al., 2016; G. Wang et al., 2014), with distance of deflection reflecting force of contraction (Figure 1.2D). The layer is microcontact patterned with fibronectin to induce an anisotropic formation of the CM tissue that synchronously contracts uniaxially, causing

the deflection of the MTF in one direction, thus enabling the calculation of contractile force generation from the entire tissue. MTF technology has been incorporated with many cell types for tissue formation (Alford et al., 2010; Feinberg et al., 2012; Grosberg, Alford, McCain, & Parker, 2011; Grosberg et al., 2012), including cardiac, to elucidate alterations in tissue contraction from tissue-specific insults that influence contractile properties.

In another method to measure mechanical force of 3D cardiac tissue, the incorporation of elastic deformable silicone microposts allowed direct measure of force during tissue contraction (Mannhardt et al., 2016; Schaaf et al., 2011). Mannhardt et. al. produced highly anisotropic hESC-derived cardiac tissue around elastomeric silicone microposts with organized sarcomeres, denoted as engineered heart tissue (EHT). Through gene expression analysis, they demonstrated the physiological relevance of the model in the upregulation of cardiac markers, including MYH7, within the platform compared to cardiac-differentiated embryoid bodies. Additionally, they validated the ability of the EHTs to study the effect of various inotropic modulators, i.e. calcium, isoprenaline, and ryanodine, on tissue contractility through average contraction peaks and contraction kinetics. Calculation of these metrics after drug administration, clinically-relevant, expected changes in contractility were demonstrated. The ability of these models to study the contractility of engineered cardiac tissues presents a significant advantage in assessing function in addition to structural and biochemical changes. Correspondingly, various methods that are incorporated to mature stem cell-derived

cardiac tissues serve as a great advantage of these models over standard 2D *in vitro* assays for studies on CVDs.

A majority of available stem cell differentiation protocols result in generation of ventricular-specific CMs, that are usually incorporated in the aforementioned models. As the different chambers in the heart have largely different electrophysiological signatures (Grandi et al., 2011), there have been strides to incorporate both ventricular and atrial CMs within these models, through chamber-specific directed differentiation protocols. For example, Zhao et. al. demonstrated a chamber-specific cardiac tissue platform, denoted as Biowire II, with sustained electrical conditioning both to mature encapsulated cells and provide distinctive pacing regimes for the different types of CMs (Figure 1.2E) (Y. Zhao et al., 2019). Specifically, the Biowire II model incorporated flexible wires within an array of microwells for cardiac tissue attachment, cellular compaction, and alignment. Atrial and ventricular tissues were formed separately, and corresponding electrical conditioning was applied for an extended period (up to 42 days). The stimulated cardiac tissues were then analyzed with comparison to their non-stimulated counterparts. In the conditions with applied electrical conditioning, they found that the different chamber-specific tissues mapped to their corresponding cardiac region gene expression patterns. This platform demonstrated its physiologic relevancy to the human native myocardium, with incorporation of both atrial and ventricular CMs, in addition to enhanced maturation of CMs through sustained electrical conditioning.

1.5 Application of 3D microengineered cardiac tissues for disease modeling

In the past few years, significant progress in establishing a biomimetic, clinically relevant healthy 3D cardiac tissue models has been accomplished. In the next section, we will outline some of these currently available 3D cardiac microengineered platforms that have been successfully used for cardiac disease modeling.

To model heart failure caused by neurohumoral overstimulation, Tiburcy et. al. utilized EHT technology for hPSC-CM tissue formation, then administered either norepinephrine and/or endothelin-1 over 7 days (Tiburcy et al., 2017). Long-term administration of norepinephrine (NE), an adrenoceptor agonist, induced CM hypertrophy as demonstrated through contractile dysfunction of the engineered heart tissue, which proved unreceptive to rescue with isoprenaline in conditions with chronic application of 1 μ M NE. This finding demonstrates β -adrenergic desensitization of the hypertrophied tissues, thereby corroborating the clinical phenotype often observed in patients with heart failure. This study demonstrated the successful induction of a pathophenotype through chronic application of an external insult to a healthy 3D cardiac tissue.

Mutations in myosin-binding protein C cardiac isoform (MYBPC3), the accessory protein of the sarcomere A-band, have been found in various types of cardiomyopathy (Carrier et al., 1997), however the relationship between these mutations and disease onset remains unknown. To investigate the hypothesis that physiologic stress exacerbates disease symptoms in patients with these mutations, Ma et. al. generated cardiac tissues from CRISPR/Cas9-edited hiPSCs deficient in MYBPC3 to identify the gene-specific

response to mechanical stress (Ma et al., 2018). Specifically, two-photon polymerization was used to fabricate filamentous matrices of different sized parallel fibers, with thicker fibers exhibiting higher mechanical resistance. Cardiac tissues composed of WT hiPSC-CMs exhibited adaptation to mechanical load alterations through changes in contraction velocity and force, mimicking the behavior of the native myocardium. Although the structural properties of tissues composed of mutated MYBPC3-derived CMs appeared similar to the WT cardiac tissues (Figure 1.3D), when exposed to higher mechanical resistance, the mutated CMs exhibited increased probability of early after-depolarizations (EADs) than the WT counterparts. These results were in fact consistent with the clinical finding that patients with cardiomyopathy are more prone to EADs. Therefore, the incorporation of a substrate with adjustable stiffness enabled assessment of tissue-level response to mechanical stress, highlighting the possible connection between onset of cardiomyopathy and mutations in MYBPC3.

3D tissue models have been also integrated with genetically-edited human-derived cardiac cells to create complex 3D diseased tissue models. For example, hypertrophic cardiomyopathy (HCM) has been widely studied because of its heterogeneity, as evidenced by the fact that half of the patients with HCM have mutations in one or more of >20 sarcomeric genes (Cahill, Ashrafian, & Watkins, 2013). In order to better understand the role of various known mutations in HCM, Mosqueira et. al. produced 11 different variants of the HCM-causing mutation cC9123T-MYH7 in 3 different hPSC lines via CRISPR/Cas9 gene editing (Mosqueira et al., 2018) (Figure 1.3A). After CM differentiation, the cells were incorporated into EHT models and the

functionalities of the different variant-derived hPSC-lines were compared to their 2D counterparts. Through transcriptomics of the tissues, opposing trends were demonstrated between 2D and 3D culture formats. Specifically, there were decreases in expression of genes involved in calcium handling and less pronounced changes in apoptosis and autophagy in the 3D tissues as compared to 2D assays. Incorporation of these gene-edited hiPSC-CMs within EHTs also allowed measurements of tissue contraction, revealing reduced contraction force and increased contraction time in tissue formed from mutated hiPSC-CMs. This study demonstrated the merit of a 3D platform over conventional 2D for disease modeling applications. Additionally, the use of various gene-edited hiPSC-CMs enabled the study of cardiac function pathology that is directly attributable to specific mutations, an advantage over the genetic heterogeneity present in patient-derived CMs. However, many works tend to use both gene-edited and patient-derived hiPSC-CMs to understand both disease-specific and patient-specific mechanisms of disease progression at the tissue-level (Hinson et al., 2015; G. Wang et al., 2014).

Wang et. al. for instance investigated both patient-derived and genetically engineered hiPSC-CMs of Barth syndrome (BTHS), a syndrome characterized by mitochondrial myopathy from an X-linked mutation in tafazzin (TAZ). After assessment of structural irregularities in both types of diseased CMs, cells were incorporated into MTF technology to create a 3D cardiac tissue diseased model to highlight the specific contractile mechanisms that are affected in CMs with these mutations (G. Wang et al., 2014). Through electrical stimulation of the MTFs, they successfully calculated radii of curvature, diastolic and peak systolic stresses, and twitch stress to measure differences in

tissue contractility (Figure 1.3B). Both the BTHS-derived and the gene-edited heart tissues demonstrated significantly reduced twitch and peak systolic stresses than controls, recapitulating the BTHS myopathic phenotype in an *in vitro* model. They further studied whether the functionalities of the disease tissues could be restored through treatment with TAZ synthetic chemically modified mRNA (modRNA). Upon TAZ modRNA administration, they observed restoration of contractile function, demonstrating the utility of this approach in reversing myopathy disease phenotype. Particularly, incorporation of these cardiac cells within MTFs allowed the study of contractility to highlight cardiac dysfunction in BTHS in a highly controllable 3D format that is not possible in animal models or 2D *in vitro* assays. In a similar experimental format, a study by Hinson et. al., investigated the role of mutations of the sarcomeric protein, titin, in dilated cardiomyopathy using hiPSC-CMs from patients with titin-truncating variants (TTN_{trvs}) (Hinson et al., 2015). Incorporation of elastomeric microposts, known as microarray post detectors (mPADs), led to the formation of an aligned cardiac microtissue (CMT) (Boudou et al., 2012) (Figure 1.3C). The microposts contained embedded fluorescent microbeads that allowed for computerized cantilever deflection tracking, providing a quantitative, objective method to measure the contraction force generated by the CMTs. They further used CRISPR/Cas9 technology to induce similar mutations of the titin gene within CMTs. In both types (i.e., patient vs genetically-derived) of disease-derived CMTs, reduction in contractile force was observed when compared to CMTs generated from WT hiPSCs. However a more significant reduction (more than 50%) was found in patient-derived CMTs, raising the possibility that additional genetic variants affect the

function of titin and thus the emulation of pathophysiology. Similarly, there was an observed reduction in contractility of the genetically-edited CMs when compared to WT, however it was not as significant as the patient-derived CMs. The limited change in functionalities of the gene-edited CMs demonstrates the role of genetic background in the manifestation of cardiomyopathy. Similarly, Zhao et. al. incorporated the Biowire II model to study left ventricular hypertrophy (LVH), through generation of cardiac tissues with LVH patient-derived hiPSC-CMs (Y. Zhao et al., 2019). However, with the cause unknown for the underlying phenotype of LVH, chronic electrical conditioning protocols were also applied to the tissues to better mimic the clinically-observed increases in cardiac workloads in patients with hypertension. After 8 months of electrical conditioning, significant upregulation in gene expression for hypertrophy and heart failure were identified in biowires formed from LVH-patients in comparison to non-affected controls. Therefore, through use of both patient-derived cardiac tissues and external conditioning, recapitulation of pathophysiology was achieved within this 3D cardiac tissue model. Overall, the aforementioned studies demonstrate the utility of 3D diseased cardiac tissue models to recapitulate the corresponding pathophysiology, and their potential to serve as platforms for more precise cellular-level mechanistic studies.

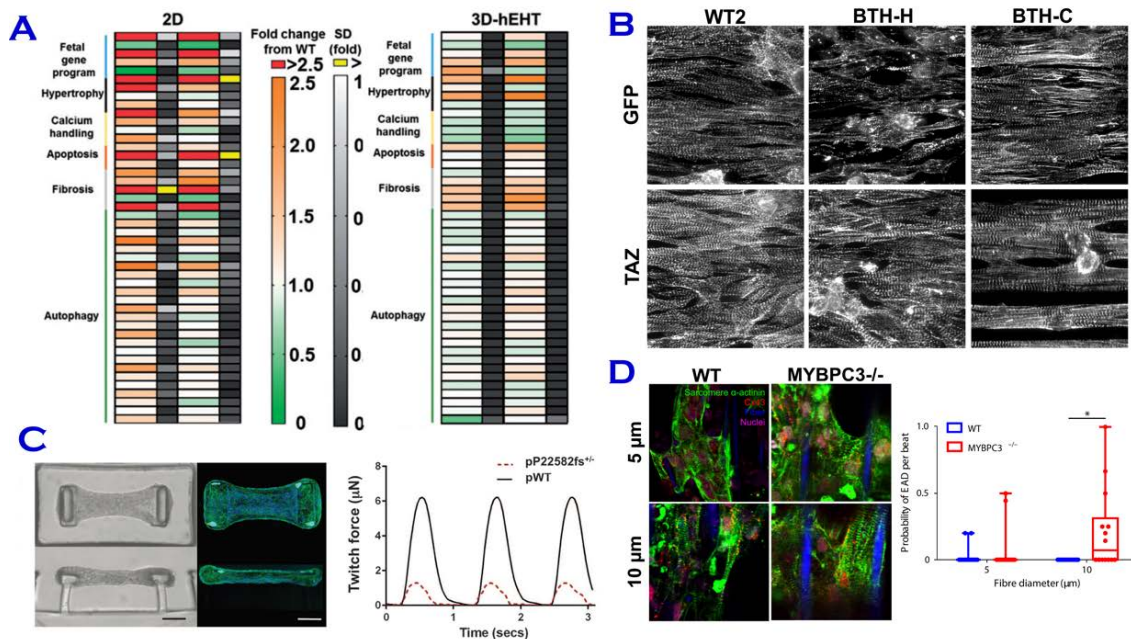


Figure 1.3: Three-dimensional microengineered models of cardiac diseases.

(A) Relevant gene expression changes in 2D and 3D-EHT cardiac tissue models of hypertrophic cardiomyopathy, reprinted with permission from (Mosqueira et al., 2018).

(B) Sarcomere organization of cardiac tissues from patient-derived and gene-edited cells for modeling of BTHS with response to TAZ restoration, reprinted with permission from (G. Wang et al., 2014).

(C) Representative image of CMTs and twitch forces of CMTs from WT and patient-derived cells to study dilated cardiomyopathy, reprinted with permission from (Hinson et al., 2015).

(D) Cardiac-related marker expression and electrical activity of WT and gene-edited cardiac tissues within constructs of different sized fibers, reprinted with permission from (Ma et al., 2018).

1.6 Thesis Aims and Overview

The limitations faced in cardiovascular disease research have been attributed to the lack of suitable *in vitro* models to supplement *in vivo* animal studies. Particularly, the advent of stem cell *in vitro* differentiation has enabled the abundant sourcing of human stem cell-derived CMs, however these cells present with a highly immature phenotype. The physiologic dissimilarities of these cells compared to healthy adult myocardium creates a hindering obstacle in the translation of *in vitro* research to clinical studies.

This thesis primarily aims to create a microfluidic heart on-a-chip model that can enhance the maturation state of stem cell-derived CMs, to serve as a suitable platform for *in vitro* cardiac tissue modeling. Furthermore, the engineered chip is utilized to model complex cardiovascular disease (CVD) to perform mechanistic biological studies on disease progression due to environmental and genetic factors. Specifically, in this work, we have developed a 3D microengineered heart on-a-chip platform with innate, precisely designed microposts that induce structural anisotropy of co-cultured cardiac tissue. We thoroughly study the formed cardiac tissue characteristics, and particularly investigate the role of mesoscopic-induced anisotropy on tissue maturation state. Upon validation of the microfluidic platform in its ability to promote formation of a 3D, mature, and anisotropic cardiac tissue composed of stem cell-derived CMs, this thesis further aims to examine the capability of the microfluidic platform to model complex CVD. Specifically, we primarily expose the microengineered cardiac tissues to hypoxic conditions to induce an ischemic response, and study the resultant tissue through transcriptomic profiling and contractile function. Moreover, we utilize gene-editing techniques to create an hiPSC line

with a mutation in *KCNH2*, then incorporate this line within the platform to model LQTS2 on-a-chip.

Completion of this study will be accomplished through the following specific aims:

1.6.1 Specific Aim 1

Develop a novel microfluidic heart on-a-chip platform and optimize 3D cardiac tissue formation with both rat-derived and human stem cell-derived cardiac cells. We will present the creation of a microfluidic heart on-a-chip model for 3D cardiac tissue formation and study the effect of micropost-induced anisotropy on cardiac tissue formation, structure, and function.

1.6.2 Specific Aim 2

Incorporate the optimized microfluidic platform to create a model of cardiac ischemia on-a-chip to investigate cellular and molecular response of myocardial tissue under hypoxia. Using our microfluidic model developed in Specific Aim 1, we investigate the effect of extended hypoxia on human stem cell-derived mature cardiac tissue. Particularly, through subsection of the tissue to varying levels of ischemic insult, we present a model of myocardial ischemia on-a-chip.

1.6.3 Specific Aim 3

Create an hiPSC line with a *KCNH2* mutation, using CRISPR/Cas9 gene-editing, and model Long QT Syndrome Type 2 on-a-chip within developed microfluidic platform. We will utilize CRISPR/Cas9 gene-editing to induce a missense

mutation in the gene *KCNH2* at base 1591 into hiPSCs to create a LQTS2 cell line. We will differentiate cardiomyocytes and cardiac fibroblasts from this line and incorporate the edited cardiac cells within the microfluidic device developed in Specific Aim 2 to model LQTS2 on-a-chip.

CHAPTER 2

AIM 1: Develop a novel microfluidic heart on-a-chip platform and optimize 3D cardiac tissue formation with both rat-derived and human stem cell-derived cardiac cells

2.1 Abstract

Despite significant efforts in the study of cardiovascular diseases (CVDs), they persist as the leading cause of mortality worldwide. Considerable research into human pluripotent stem cell-derived cardiomyocytes (hPSC-CMs) has highlighted their immense potential in the development of *in vitro* human cardiac tissues for broad mechanistic, therapeutic, and patient-specific disease modeling studies in the pursuit of CVD research. However, the relatively immature state of hPSC-CMs remains an obstacle in enhancing clinical relevance of the engineered cardiac tissue models. In this study, we describe development of a microfluidic platform for 3D modeling of cardiac tissues, derived from both rat derived- and hPSCs-CMs, to better recapitulate the native myocardium through co-culture with interstitial cells (specifically cardiac fibroblasts), biomimetic collagen hydrogel encapsulation, and induction of highly anisotropic tissue architecture. The presented platform is precisely engineered through incorporation of surface topography in the form of staggered microposts to enable long-term culture and maturation of cardiac cells, resulting in formation of physiologically relevant cardiac tissues with anisotropy that mimics native myocardium. After two weeks of culture, hPSC-derived cardiac tissue exhibited well-defined sarcomeric striations, highly synchronous contractions, and upregulation of several maturation genes, including HCN1, KCNQ1, CAV1.2, CAV3.1,

PLN, and RYR2. These findings demonstrate the ability of the proposed engineered platform to mature animal- as well as human stem cell-derived cardiac tissues over an extended period of culture, providing a novel microfluidic device with the capability for cardiac disease modeling and therapeutic testing.

2.2 Introduction

Heart disease remains the leading cause of mortality, despite abundant advancements in cardiovascular research (Heidenreich et al., 2011). Research involving animal models has contributed significantly to cardiovascular disease-related knowledge gathered to date, however challenges remain in translating preclinical findings to human conditions due to pronounced physiological differences (Rajamohan et al., 2013). Additionally, inherent difficulties in studying the heart *in vivo* at cellular and molecular levels hinder the discovery and extensive study of disease-specific mechanisms. In the past few years, synergistic *in vitro* models using human cells/tissue that enable detailed mechanistic studies of cell-cell and cell-environment interactions serve to complement *in vivo* preclinical findings (Guo et al., 2011; Liang et al., 2016; Mosqueira et al., 2018; Sun et al., 2012; G. Wang et al., 2014). *In vitro* research based on the use of human cardiac cells is now more accessible, due to advances in the development of robust and reproducible methods for directed differentiation of high yield human stem cell-derived CMs, from both human embryonic stem cells (hESCs) and human induced pluripotent stem cells (hiPSCs), referred to collectively as hPSCs (Lian et al., 2013). Particularly, methods to purify differentiated cardiac populations for cardiomyocytes (CMs) (Ban, Bae, & Yoon, 2017), including magnetic-activated cell sorting (MACS) (Uosaki et al.,

2011), fluorescence-activated cell sorting (FACS) (Dubois et al., 2011), and metabolic selection (Sharma et al., 2015), have enabled consistent yields of highly pure CM populations, that have been extensively used, among many other applications, to engineer *in vitro* human cardiac tissue models for mechanistic, disease-specific, and therapeutic research. However, although CMs comprise most of the volume, cardiac fibroblasts (CFs) constitute a majority of the cell population within the heart (Radisic et al., 2007), causing structural misalignment in the majority of *in vitro* studies that rely on mono-culture of hPSC-CMs. Some studies continue to use unpurified hPSC-CM populations to address the need for multi-culture populations (Ronaldson-Bouchard et al., 2018; D. Zhang et al., 2013), that include interstitial non-CM cells, such as fibroblasts, smooth muscle cells, and endothelial cells at differing ratios. However, CM purity and cellular composition have proven quite difficult to control during human stem cell differentiation, resulting in extensive variation in cellular composition of heart tissues in models that utilize mono-culture of unpurified hPSC-CMs. Therefore, there is a need for the incorporation of controlled and consistent co- or multi-culture ratios of purified CMs and supporting interstitial cells within *in vitro* platforms to better recapitulate the native architecture and function of human myocardium.

The complex cellular composition within intricate architecture in the native myocardium is necessary for highly synchronous organ-level contraction (Valderrabano, 2007). During myocardial development, CMs are exposed to physical, electrical, and mechanical stimuli that enhance alignment of overall tissue structure, promote cell elongation and increase cell length-to-width ratios, thereby influencing intracellular

contractile machinery, including alignment of sarcomeres and localization of gap junctions (Bray, Sheehy, & Parker, 2008). Due to these stimuli, the muscle fibers arrange in a parallel array, and the cells organize in an anisotropic manner, with electromechanical connections forming through intercalated discs at the perpendicular edges. To that end, it is crucial to recapitulate the native-like 3D tissue anisotropy within engineered *in vitro* tissue models for physiologically relevant cellular- and molecular-level studies. Previous studies have utilized numerous strategies to align cardiac tissue by simulating relevant stimuli that are experienced by the native myocardium, including environmental cues, such as micropatterned substrates (Agarwal et al., 2013) or surface topography (Shadrin et al., 2017; D. Zhang et al., 2013), mechanical tension and electrical stimulation (Agarwal et al., 2013; Nunes et al., 2013; Ronaldson-Bouchard et al., 2018; Schaaf et al., 2011).

However, a current obstacle for clinical translation of *in vitro* platforms is the relatively immature state of hPSC-CMs, evidenced by round cell morphology, lack of mature contractile machinery, and gene expression profiles resembling fetal CMs (Binah et al., 2007; Ivashchenko et al., 2013; Jiang, Park, Hong, & Ban, 2018; Lundy, Zhu, Regnier, & Laflamme, 2013; Snir et al., 2003; Veerman et al., 2015; X. Yang, Pabon, & Murry, 2014). To enhance clinical relevance and future translation of stem cell-derived CMs, a multitude of techniques have been investigated to aid in their maturation (X. Yang et al., 2014). These methods range from applied stimulation, i.e. electrical or mechanical (Nunes et al., 2013; Y. Zhao et al., 2019); culture variation, i.e. long-term culture (Lundy et al., 2013), media supplementation (Chattergoon et al., 2012), or co-

culture with non-CMs (C. Kim et al., 2010); or environmental cues, i.e. extracellular matrix (Herron et al., 2016), mesoscopic architecture (Shadrin et al., 2017; D. Zhang et al., 2013), or micropatterned substrates (Saini et al., 2015). The CM populations that result from these methods exhibit more mature structure and function, evidenced through enhanced morphology, function, protein and gene expression, and electrophysiology. Recent *in vitro* studies have utilized some of these maturation techniques to model more adult-like cardiac tissues from hPSC-derived CMs within complex biomimetic platforms (Veldhuizen et al., 2019). Such platforms include 3D anisotropic patches (Shadrin et al., 2017), flexible thin films (Agarwal et al., 2013), electrically-stimulated biowires (Nunes et al., 2013), engineered heart tissues (EHT) suspended between micropillar arrays (Schaaf et al., 2011), as well as heart-on-a-chip tissues within microfluidics (Ellis et al., 2017; Mastikhina et al., 2019; Mathur et al., 2015). Among these engineered cardiac tissues, incorporation of microfluidic technology retains certain advantages for organ modeling, mainly due to precise control over diffusion of gradients (i.e. drug or chemical) and cell culture environment, low cost and ease of manufacture, and requirement for minimal quantity of tissues and corresponding reagents (Ellis et al., 2017; Mastikhina et al., 2019; Mathur et al., 2015). Due to the minimal cell and low-cost requirements involved in manufacture of each microfluidic device, a multitude of devices can be incorporated simultaneously to facilitate high throughput experimentation. This allows for a single batch of differentiated stem cell-derived CMs to be utilized for the same set of experiments, reducing variability from interdifferentiation population differences (Laco et al., 2018) that may obscure underlying biological results.

To date, notable progress has been made in engineering *in vitro* cardiac tissue models using microfluidic platforms (Bergstrom, Christoffersson, Schwanke, Zweigerdt, & Mandenius, 2015; Ellis et al., 2017; Mathur et al., 2015). Similar to macroscale approaches, microfluidic cardiac tissues have also been formed both with and without scaffolds. The related advantages and disadvantages of scaffold-based vs scaffold-free approaches that have been discussed extensively (Zuppinger, 2019) can also be applied to tissues created at the microscale. Despite significant findings of both approaches using microfluidics, many *in vitro* platforms have incorporated mono-culture of hPSC-CM derived populations to specifically model 3D myocardial tissue. In addition, the majority of these studies have characterized the functionalities of the engineered micro-tissues through immunofluorescence, drug responsiveness, and force generation, to provide important information about the engineered tissue structure and function. To further enhance these findings, it is critical to additionally perform extensive molecular-level studies, including protein or gene expression analyses, in comparison to age-matched cell populations. Such validation of the resultant tissues generated within microengineered models is crucial for their effective translation in future disease-specific and therapeutic studies. Furthermore, as the anisotropic architecture of the myocardium is pertinent for its proper function, some of these microfluidic models utilize extracellular matrix (ECM) coating and confined features to create aligned cardiac tissues (Mathur et al., 2015). To better mimic the inherent 3D extracellular matrix and fibers of the native myocardium, there is a need for incorporation of aligned 3D cardiac tissues within microfluidic platforms.

In this study, we demonstrate the development of a novel microfluidic platform precisely designed and further characterized with three distinct cell types, to induce anisotropy of co-cultured 3D hydrogel-encapsulated cardiac tissues, while enabling enhanced nutrient diffusion through the creation of repeated elliptical pores throughout the tissue (Bian, Liau, Badie, & Bursac, 2009). Specifically, surface topography was incorporated within the central 3D tissue region of the microfluidic platform, in the form of staggered microposts, to mimic the anisotropic structure of the human native myocardium, serving to further enhance physiological relevance of our model. In addition, to better control the composition and reduce variation among cardiac tissues from different differentiation batches, we utilized a metabolic purification protocol to select for high percentages of CMs from hPSC-derived populations. The highly pure CM populations (85.5[±]/.5.3% cTnT⁺) were co-cultured with human CFs at a consistent ratio (4:1 CM:CF), encapsulated in a hydrogel, and housed within the 3D microfluidic device to generate biomimetic myocardial tissue. The microfluidic nature of the platform enabled establishment of exact temporal and spatial gradients for possible future drug-related studies, while maintaining a minimal cell (i.e. <35,000 cells per device) and reagent requirement for optimal experimental design. Cardiac tissues formed within the designed microfluidic chip were reproducibly generated from three distinct cell types, and present with enhanced mature cellular structure, protein expression, gene expression and tissue function.

2.3 Methods

2.3.1 Microfluidic device fabrication

Photolithography and replica molding technique were used to create the microfluidic devices, consistent to our previous work (Nagaraju, Truong, Mouneimne, & Nikkhah, 2018; Peela, Barrientos, Truong, Mouneimne, & Nikkhah, 2017; Truong et al., 2016; D. D. Truong et al., 2019), composed of staggered elliptical microposts within the main channel, bordered by arrays of trapezoidal microposts. Briefly, SU8 2075 was spin-coated to 200 μm on a 4" silicon wafer. The wafer was exposed to ultraviolet light through a transparent mask of the microfluidic channel design (created in AutoCAD). After development of the SU8, the wafer was prepared for polydimethylsiloxane (PDMS, Essex Brownell) replica molding via silanization, using methyltrichlorosilane (MTCS) of the surface to reduce attraction between cast PDMS and SU/8 features. PDMS base and crosslinker were mixed at a 10:1 ratio and poured on the master silicon wafer. After 1.5 hours of curing at 80°C, the PDMS mold was peeled and holes for the inlets and outlets of the tissue and media channels were made with biopsy punches (1 mm for tissue channel and 1.5 mm for media channels). The PDMS channels were then bonded to 18x18 mm coverslips with oxygen plasma (PDC-32G, Harrick Plasma), and baked at 80°C overnight to secure bonds. The devices were sterilized via two cycles of autoclave, first through liquid cycle and then through gravity cycle. The devices were baked at 80°C overnight to ensure dehydration before use in cell culture experiments.

2.3.2 Diffusion analysis through the 3D cardiac tissue region

Simulation of diffusion of 10kDa FITC-Dextran through the 3D cardiac tissue region was performed with COMSOL Multiphysics. With the assumption that the gel is uniform in the z-direction, simulation of diffusion was only performed in the x-y region (Truong et al., 2016). Using the Stokes-Einstein equation $D=(kT)/(6\eta\pi R)$ (Kothapalli & Honarmandi, 2014) where D is diffusion coefficient, R is stokes radius (69 angstroms), T is temperature (310.15K), K is the Boltzmann coefficient ($1.38*10^{-23}$ J/K), and η is the dynamic viscosity of media at 37°C ($0.78*10^{-3}$ N*s/m²) (Wang, Lu, & Schwartz, 2012), the value for the diffusion coefficient of 10 kDa of FITC-Dextran in media at 37°C was found to be $4.22*10^{-12}$ m²/s. In order to determine the diffusion coefficient of the tissue region, the diffusion hindrance coefficient was determined as 0.94 with the main hydrogel component as collagen type 1 (2 mg/mL), therefore the diffusion coefficient for media was multiplied by 0.94 (Truong et al., 2016), to find the diffusion coefficient of the hydrogel to be $3.97*10^{-12}$ m²/s. The concentration of dextran within the media channels was set to 10 µg/mL, and the tissue channel at t=0 to be 0 µg/mL.

2.3.3 Neonatal rat cardiac cell isolation and culture

Neonatal ventricular rat-derived cardiomyocytes (rCMs) and cardiac fibroblasts (rCFs) were obtained from two-day old neonatal rats based on a well-defined protocol approved by Institution of Animal Care at Arizona State University, as demonstrated in our earlier work (Navaei et al., 2017; Navaei et al., 2019; Navaei, Saini, et al., 2016; Navaei, Truong, et al., 2016; Saini et al., 2015). The thorax of the rats was opened and the heart was surgically removed. Upon removing the atria, the hearts were cut into 3-4

medium sized pieces and placed in 0.05% trypsin solution (without EDTA; Gibco) prepared in Hank's balanced salt solution (HBSS; Gibco) for 14–16 h at 4 °C with continuous gentle agitation. After trypsination, the heart pieces were neutralized in cell culture media and further subjected to collagenase treatment to digest the ECM and isolate the cells, comprised mainly of rCMs and rCFs. The cell suspension was preplated and the cells left to attach for an hour. The suspended cells were collected, as the rCMs, and the attached cells were isolated as the rCFs. The rCMs and rCFs were immediately used for device culture. Both cell types were suspended for a final density of 30×10^6 cells/mL and mixed to desired ratio (i.e. 1:0, 8:1, or 4:1 CM:CF), then this cell mixture was mixed with bovine thrombin, bovine fibrinogen, and rat tail collagen type 1 (Corning), for a final concentration of fibrin (2 mg/mL) and collagen (1 mg/mL) at a ratio of 85:15. The cell:hydrogel solution was injected into the microfluidic device, flipped and polymerized at 37°C for 18 minutes, then media (DMEM 1X, 10% FBS, 1% Pen/strep, 1% L-glutamine) was added to the side channels. Media was changed daily.

2.3.4 Human stem cell culture

hESCs, that were edited through delivery of a plasmid encoding GFP under the hTNNT2 promoter, were received as a generous gift from Dr. David Brafman's lab (ASU). hiPSCs (cell line: SCVI20) were purchased from Stanford Cardiovascular Institute Biobank. Pluripotency of hPSC lines was continually validated through immunofluorescence of SOX2 and Nanog (Appendix Figure A.1). Both hESCs and hiPSCs were cultured with defined Essential-8 (E8) media (made in house) on Matrigel (Corning)-coated plates. Media was changed daily, and cells were passaged every 3-4

days depending on confluency. For passaging, 0.5 mM EDTA (Corning) was used, and E8 media was supplemented with 5 μ M Y27632 (Stem Cell Technologies) for 24 hours to enhance cell survival. Cells were cryopreserved in 90% FBS and 10% DMSO.

2.3.5 Human cardiac fibroblast (CF) culture

Human ventricular cardiac fibroblasts (hCFs) were purchased from Lonza and were grown in DMEM supplemented with 10% FBS (Thermo), 1% Penicillin/streptomycin (Thermo), and 1 ng/mL bFGF (PeproTech). hCFs were passaged with 0.05% Trypsin-EDTA (Thermo), and used for experiments from passage 4-10. hCFs were characterized for protein expression of vimentin and CX43, and validated for lack of differentiation to myofibroblasts, through α -smooth muscle actin (α SMA) expression (Appendix Figure A.2).

2.3.6 Human cardiomyocyte (CM) differentiation

The differentiation protocol used for ventricular-specific CMs from hPSCs involved the use of small molecule induction (Lian et al., 2013) and CM selection through glucose starvation (Sharma et al., 2015; Tohyama et al., 2013). Specifically, after culture of hPSCs in E8 media until near confluency (~80%), the differentiation protocol was initiated by media change to RPMI+B27 minus insulin (RPMI, 2% B27 minus insulin, 1% Pen/strep), and activation of the Wnt pathway, through inhibition of the Glycogen Synthase Kinase-3 (GSK) pathway, with 12 μ M CHIR99021 (BioVision) on Day 0 (D0). After 24 hours of Wnt activation (D1), the media was changed to simply RPMI+B27 minus insulin to allow for cell recovery. At D3, half of the media was

removed, and the rest of the media was resupplied as conditioned media, and the Wnt pathway was inhibited with 5 μ M IWP-2 (Sigma). At D5, the media was changed to RPMI+B27 minus insulin for cell recovery. Then, D7 and D9, the media was changed to RPMI+B27 plus insulin (RPMI, 2% B27 plus insulin, 1% Pen/strep) to support cardiac maturation. At D11 and D14, the media was changed to RPMI without glucose +B27 plus insulin, supplemented with 4 mM sodium lactate and 1% pen/strep, to purify the population for CMs (Sharma et al., 2015). Then, on D17 for cell recovery, the media was switched back to RPMI+B27 plus insulin. At D19, the purified CMs were replated, with TrypLE Express (LifeTech) to lift cells onto new Matrigel-coated plates, to remove dead cells and cell debris. At this point, the CMs were characterized (i.e., via flow cytometry and IF; Appendix Figure A.3) and were then used for the formation of the 3D cardiac tissue within the microfluidic platform.

2.3.7 Formation and culture of 3D hPSC-CM tissue within the microfluidic platform

After differentiation and purification of hPSC-CMs, the CMs were prepared for use in experiments. Specifically, the wells were washed with 1X DPBS (Dulbecco's phosphate buffered solution), and the cells were lifted off with TrypLE Express (LifeTech) incubation following 37°C for 10 minutes. Then, the cells were mechanically dissociated through pipetting up and down against the culture vessel, and the enzyme was buffered with RPMI + B27 + insulin. CMs were centrifuged at 300g for 3 minutes. The supernatant was aspirated, then the cell pellet was resuspended in RPMI+B27+insulin. Similarly, in parallel, CFs were trypsinized and collected for device loading. CMs were mixed with CFs at a 4:1 ratio (as determined through a series of optimization, and thus

used for all subsequent experiments), mixed with collagen (final concentration 2 mg/mL), and 20% Matrigel, rendering the final cell density as 35×10^6 cells/mL. Cell-embedded hydrogel solution was mixed and subsequently injected into tissue region of microfluidic platforms (3 μ L per device). Devices were flipped and incubated at 37°C for 18 minutes for hydrogel polymerization, then RPMI+B27+insulin was injected into the flanking media channels. Media was changed everyday. Similarly, 4:1 CM:CFs were plated in Matrigel-coated 24-well plates for age-matched monolayer experimental setting.

2.3.8 Microscopy

Phase contrast and fluorescence images were acquired using Zeiss Axio Observer Z1 equipped with Apotome2 (Zeiss) and ZenPro software. Throughout the cell culture period, samples were imaged every other day using phase contrast at a 10X objective. Time-lapse imaging was recorded at 10X objective for 30 seconds at 37°C on Day 14 to analyze spontaneous contraction of the 3D tissue inside the chip. To calculate inter-beat interval variability, the contraction peaks were extracted, and the time between beats was calculated using custom written Matlab codes, adapted from (S. B. Kim et al., 2011). The standard deviation of the inter-beat interval was calculated and deemed the measure of inter-beat interval variability.

2.3.9 Immunofluorescence (IF)

For IF staining, samples were fixed in 4% paraformaldehyde (PFA) at Day 14 of culture. The devices were incubated at 37°C for 15 minutes. Afterwards, the cells were rinsed with PBS-glycine 2X for 10 minutes of incubation each at room temperature. The

final wash was with PBS-Tween-20 ((PBS-Polyoxyethylene (20) sorbitan monolaurate) (0.05% (v/v) Polyoxyethylene (20) sorbitan monolaurate in PBS) for 10 minutes at room temperature. Then, the cells were permeabilized with 0.1% Triton-X-100 for 30 minutes at room temperature. To inhibit non-specific binding of the antibodies, blocking was then performed with 10% goat serum solution for one hour at room temperature. To stain for cardiac-specific markers, the primary antibodies were diluted in 10% goat serum and added to the samples at 4°C overnight. The following primary antibodies were used for immunofluorescence staining: rabbit anti-Sox2 (Cell Signaling, 1:100), mouse anti-Nanog (Abcam, 1:200), rabbit anti-Connexin 43 (Abcam, 1:200), mouse anti-Sarcomeric α -actinin (Sigma, 1:200), rabbit anti- α smooth muscle actin (Abcam, 1:100), mouse anti-cTnT (Thermo, 1:200), mouse anti-von Willebrand Factor (Santa Cruz, 1:200), and rabbit anti-Vimentin (Cell Signaling, 1:250).

Upon addition of the primary antibodies, the following day, the samples were washed with PBS-Tween-20 three times for 20 minutes each at room temperature. Then, the secondary antibodies were diluted in PBS-Tween-20 (1:500), centrifuged at 14K RPM for 10 minutes, then added to the samples. After 30 minutes-1 hour, the samples were washed with PBS-Tween-20 three times for 10 minutes each at room temperature. To stain for the actin cytoskeleton and the nucleus, Alexa Fluor488- or Alexa Fluor647-Phalloidin (1:40) and 4',6-diamidino-1-phenylindole (DAPI) (1:1000) were added to the samples and left at 4°C overnight. Then the samples were washed with PBS-Tween-20 three times for 20 minutes each at room temperature. Finally, the samples were imaged using fluorescence microscopy (Zeiss Axio Observer Z1 with the Zen Pro software suite)

equipped with Apotome2 at 10X, 20X, and 40X objectives and Z-stacked images were captured and reconstructed to form representative 3D images. Alternatively, samples were imaged with the Leica SP8 Confocal Microscope at 40X and 63X objectives, with z-stacked images captured and reconstructed to form representative 3D images.

2.3.10 Analysis of 3D cardiac tissue alignment

Tissues stained for F-actin and DAPI were used for assessment and calculation of cellular alignment. F-actin images were measured with FIJI software for Fast Fourier Transform (FFT), and DAPI images were used to quantify nuclei alignment (Raymond, Ray, Kaur, Singh, & Wan, 2016). Specifically, for calculation of alignment, images were rotated based on phase contrast to set alignment axis at 0°. DAPI images were thresholded, processed through the Watershed plugin, and the nuclei were analyzed through the Analyze Particles Plugin. Proportion of nuclei at each angle was calculated and graphed in a histogram with bins spanning 10°.

2.3.11 Quantitative real-time reverse transcription-PCR (qRT-PCR)

Gene expression was performed on hESC-derived cardiac tissues for up to n=4 experiments. Specifically, tissues within microfluidic chips were digested with 1 mg/mL collagenase type I (Alfa Aesar), and cells were collected from devices. Total RNA was extracted from cell suspension with Total RNA Microprep kit (Zymo). RNA quality and concentration were assessed with High Sensitivity RNA tapes, and Regular Sensitivity RNA tapes. cDNA was synthesized from total RNA using iScript Reverse Transcriptase Supermix (BioRad). iTaq Universal SYBR Green Supermix (BioRad) was used to

perform qPCR on synthesized cDNA, with 18S as the housekeeping gene. Primers were validated via melt curve analysis and PCR product size verification. For qPCR, 8 μ M dilution of forward and reverse primers was used for 10 μ L reactions within 384-well plates, with 0.1 μ L per of cDNA. The qPCR plates were analyzed with CFX384 Touch Real-Time PCR Detection System (BioRad).

2.3.12 Epinephrine testing

After spontaneous contractions were recorded as the baseline for day 14 of hiPSC-derived cardiac tissue culture within devices with and without posts, tissue responsiveness to epinephrine was evaluated. Specifically, epinephrine was first resuspended in 0.5M HCl at 0.1 mg/mL, then it was diluted in RPMI + B27 + insulin at a final concentration of 0.2 μ g/mL and administered to the devices for 5 minutes at 37°C (Birla et al., 2005). Then, tissues were transferred to the Zeiss microscope for 30 second video recordings at 37°C. Using the custom-written Matlab code, BPM and inter-beat interval variability were extracted for both baseline contraction and in response to epinephrine. The change in BPM and inter-beat interval variability in response to epinephrine dosing for each tissue was calculated.

2.3.13 Calcium transients

To assess calcium (Ca^{2+}) transients within engineered cardiac tissues, calcium indicator dye, Fluo-4AM assay kit (LifeTech), was used. Specifically, on day 14 of culture, tissues in devices both with and without posts were incubated with calcium indicator solution (50 μ g of Fluo-4AM in 50 μ L of Pluronic F127), in a dilution of 10 μ L

in 1mL of DPBS 1X, for 40 minutes at 37°C. Then, devices were washed with media (RPMI +B27+insulin) to wash solution for 25 minutes at 37°C, then 10 µM of blebbistatin was diluted in Tyrode's solution and incubated for 5 minutes to reduce motion artifacts. Then, tissues were transferred to the microscope, maintained at 37C, and imaged with Zeiss fluorescent microscope (at 25.23 frames/sec) at 488nm wavelength. Movies were recorded for a duration of 30 seconds, and calcium concentration changes were calculated by normalizing the fluorescent dye intensity (F) during cells' contractions to the background intensity (F₀) and plotted over time (Navaei, Saini, et al., 2016).

2.3.14 Statistical analysis

Paired, two-sided t-tests were used for statistical analysis of calculated final CM:CF ratios, inter-beat interval variability, and beats per minute for each condition using R. For gene expression data, two-way ANOVA was performed on the DCT values from qPCR data, using GraphPad Prism. Two-way ANOVA was performed using GraphPad Prism on the tissue alignment and thickness analysis.

2.4 Results and Discussion

2.4.1 Development of a microfluidic platform for generation of 3D aligned cardiac tissue

The 3D anisotropic architecture of the myocardium is highly correlated to its function; a key component that is missing in most of the microfluidic platforms. Throughout development, the human myocardium experiences a complex myriad of stimuli that induce transcriptional, electrophysiological, and structural changes, resulting

in aligned tissue architecture (C. Kim et al., 2010; Martherus et al., 2010; X. Yang et al., 2014). Although the exact sequence of events and related mechanisms that occur during development to induce tissue-level anisotropy are unknown, electrical and mechanical stimulation have been demonstrated *in vitro* to affect cardiac alignment. Similarly, micropatterning in the form of ECM printing and surface topography also enhances tissue-level alignment. Particularly, microposts have been demonstrated to serve as mesoscopic topographical cues that induce cell elongation and alignment similar to that seen in the native developing myocardium when implemented in 3D cell culture (Bian et al., 2009). Despite this, none of the existing microfluidic platforms for hPSC-CM culture have incorporated microposts as topography within the main tissue region to induce 3D cellular anisotropy. To that end, we incorporated and optimized staggered microposts within the central tissue chamber of the fabricated microfluidic platform to provide a highly controllable environment that favors induction of 3D cardiac tissue anisotropy. Through formation of repeated elliptical pores that force cells via passive tension to shape around the pore boundaries (Bian, Jackman, & Bursac, 2014), the model serves to replicate the highly anisotropic nature of the human myocardium (Figures 2.1A, B). The 3D tissue region was surrounded by media channels to allow for nutrient and oxygen diffusion. Specifically, the tissue region was separated from the flanking outer channels through borders of trapezoidal posts, that contain the hydrogel while allowing media diffusion (C. P. Huang et al., 2009), regularly spaced at 100 μm with heights and lengths of 100 μm and 200 μm , respectively. Simulation of diffusion of 10 kDa FITC-conjugated Dextran was performed with COMSOL Multiphysics to ensure proper diffusion of

molecules applied from the flanking media channels throughout tissue (Figure 2.1C). Simulation results demonstrated that the array of trapezoidal posts around the hydrogel allowed diffusion across the interface of the media channels and the 3D hydrogel-encapsulated tissue, creating a concentration gradient that levels out 3 hours after supplementation. In order to evaluate possible functionalities of the enclosed microfluidic device with perfusable media on diffusion of nutrients through the encapsulated cardiac tissue, we further performed simulation 10 kDa FITC-conjugated Dextran (Appendix Figure A.4) under constant fluid flow through the media channels. Compared to stagnant media supplementation, it appears that continuous media exchange results in enhanced diffusion to the tissue region by the 3 hour time point. Thus, further targeted studies utilizing this platform could take advantage of the intrinsic properties of its microfluidic nature to establish dynamic culture conditions, and study effects of enhanced nutrient supplementation on cardiac tissue function. However, the scope of this manuscript herein is the creation, optimization, and extensive characterization of the proposed novel microfluidic device with innate microposts to culture engineered cardiac tissue, therefore media was set to be stagnant and changed every 24 hours. Additionally, stagnant media supplementation necessitates a much simpler set up as it does not require extensive pumping or tubing, thus rendering the use of device easier and more adaptable for several biological studies.

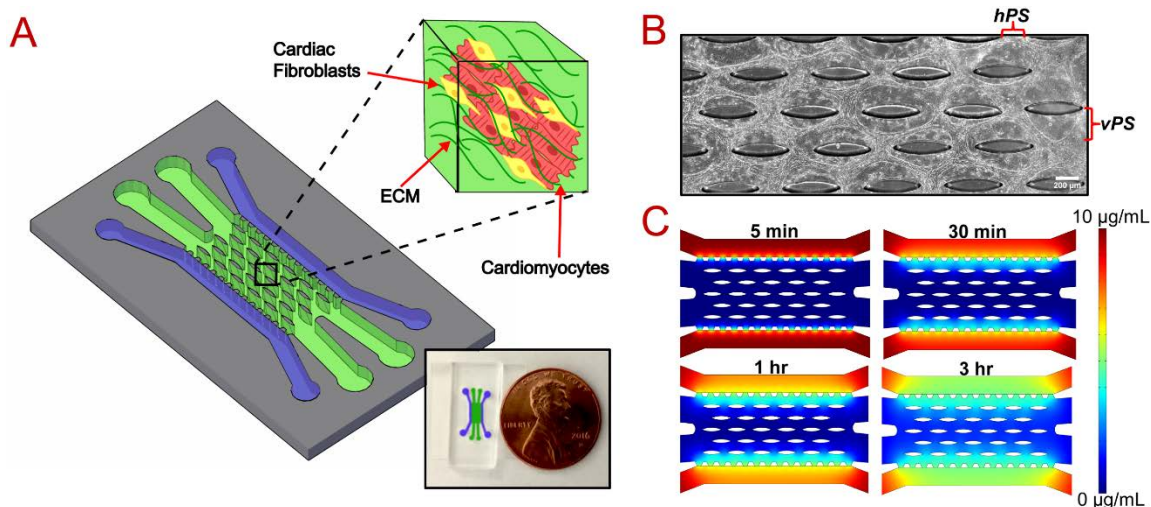


Figure 2.1: Microfluidic device for 3D cardiac tissue modeling.

(A) Schematic of microfluidic platform with inset of US penny for scaling. (B) Phase contrast image of cardiac tissues formed in device, with horizontal post spacing (hPS) and vertical post spacing (vPS) defined. (C) Simulation of 10kDa dextran diffusion from media to tissue channels, demonstrating the concentration gradient over time.

2.4.2 Generation of 3D aligned neonatal rat cardiac tissue within the microfluidic chip

We hypothesized that the 3D co-culture of hydrogel-encapsulated cardiac cells, within a microfluidic platform with precise architecture to induce tissue anisotropy over extended culture, would serve to mature the cardiac tissue. In order to test this, we performed our initial experiments using neonatal rat cardiac cells. To form the tissue, we specifically utilized co-culture of rat ventricular cardiomyocytes (rCMs) and cardiac fibroblasts (rCFs), as the co-culture of these cells better mimics the composition of the myocardium, through coordination of electrical and mechanical signal propagation and ECM deposition (Radisic et al., 2007). The co-culture of rCMs and rCFs was

incorporated within various microfluidic device designs to determine optimal parameters for the formation of 3D mature cardiac tissue, including hydrogel composition, cellular co-culture ratio, culture time, and precise device architecture (i.e., channel size and width, micropost geometry and distance). Specifically, hydrogel compositions that were tested include mixtures of fibrin, collagen, and Matrigel®. Co-culture ratios tested were 1:0, 8:1, and 4:1 CM:CFs. In order to isolate the optimal architecture of the microfluidic platform, in addition to different micropost shapes (elliptical vs hexagonal), the sizes of the microposts (200-800 μm long, 100-300 μm wide), and the staggering of the microposts (vertical post spacing: 100-300 μm , horizontal post spacing: 100-300 μm) were further studied. Within the microfluidic platforms with innate microposts, the 3D encapsulated cardiac tissues compacted the hydrogel and formed elliptical pores around the designated microposts, that varied in size and shape along with varying device design parameters. Formation of these pores induced high cell alignment around the pore boundaries, while enhancing cell elongation and nutrient diffusion across the tissue region (refer to Figure 2.1B).

Based on a series of initial experiments to enhance cell elongation and tissue formation, the optimal hydrogel composition and co-culture ratio for rCMs were found to be 85:15 of fibrin (2 mg/mL): collagen (1 mg/mL), and 4:1 CM:CF, respectively (data not shown). Dimensions of the microposts identified as optimal for tissue anisotropy were 500 μm long and 100 μm wide, with horizontal post spacing (hPS) as 150 μm . With determined hydrogel, co-culture ratio, and micropost dimensions remaining constant, iterations of device designs were tested, by varying the micropost geometry (i.e.,

elliptical vs. hexagonal) as well as vertical post spacing (vPS) (Figure 2.2A). Co-culture of cardiac cells encapsulated within a fibrin:collagen hydrogel was injected into designs with hexagonal or elliptical microposts, with varying vPS of 150 or 200 μm , and tissue architecture and function after two weeks of culture were assessed. Specifically, width of tissues, alignment of cells, and spontaneous contractions were analyzed throughout the culture period (14 days). The width of aligned tissues between microposts for each design remained consistent from Day 8 to Day 14 of culture, however the vPS had a significant effect on width of resultant tissues (Figure 2.2B). The designs with 200 μm vPS exhibit tissue bundles with the largest widths (Designs 1 and 3), while the designs with 150 μm vPS exhibit smaller width tissues (Designs 2 and 4). Nuclear alignment analysis of immunostained tissues at Day 14 highlighted a significant increase in proportion of cells aligned along the alignment axis from 0-10° in Design 1, than all other designs (Figure 2.2C), as corroborated through cytoskeletal F-actin fiber staining of cardiac tissues and corresponding Fast Fourier Transform (FFT) analysis (Figure 2.2D, Appendix Figure A.5A). Particularly, the devices with elliptical microposts (Designs 1 and 2) formed tissues with enhanced integrity, demonstrated through denser tissue bundles in IF of F-actin, than the devices with the hexagonal posts (Designs 3 and 4). In addition, anisotropic tissues formed within Design 1 (device with elliptical posts and 200 μm vPS) also demonstrated more synchronous contractile patterns on Day 14, as identified through signal extraction via a custom written Matlab code from spontaneous beating videos (Figure 2.2E, Appendix Movies A.1-4). Correspondingly, highly aligned sarcomeric striations and abundant connexin 43 (CX43) expression (Figure 2.2F,

Appendix Figure A.5B) were identified to a greater degree in this design than in tissues formed within other designs. Therefore, the particular dimensions of the innate micropost array within Design 1 induced formation of anisotropic co-cultured cardiac tissues, with corresponding enhanced cardiac-marker expression and spontaneous contractile behavior. To that end, Design 1 was chosen as the optimal microfluidic chip design for the formation of human-derived 3D cardiac tissues and all subsequent experimental studies.

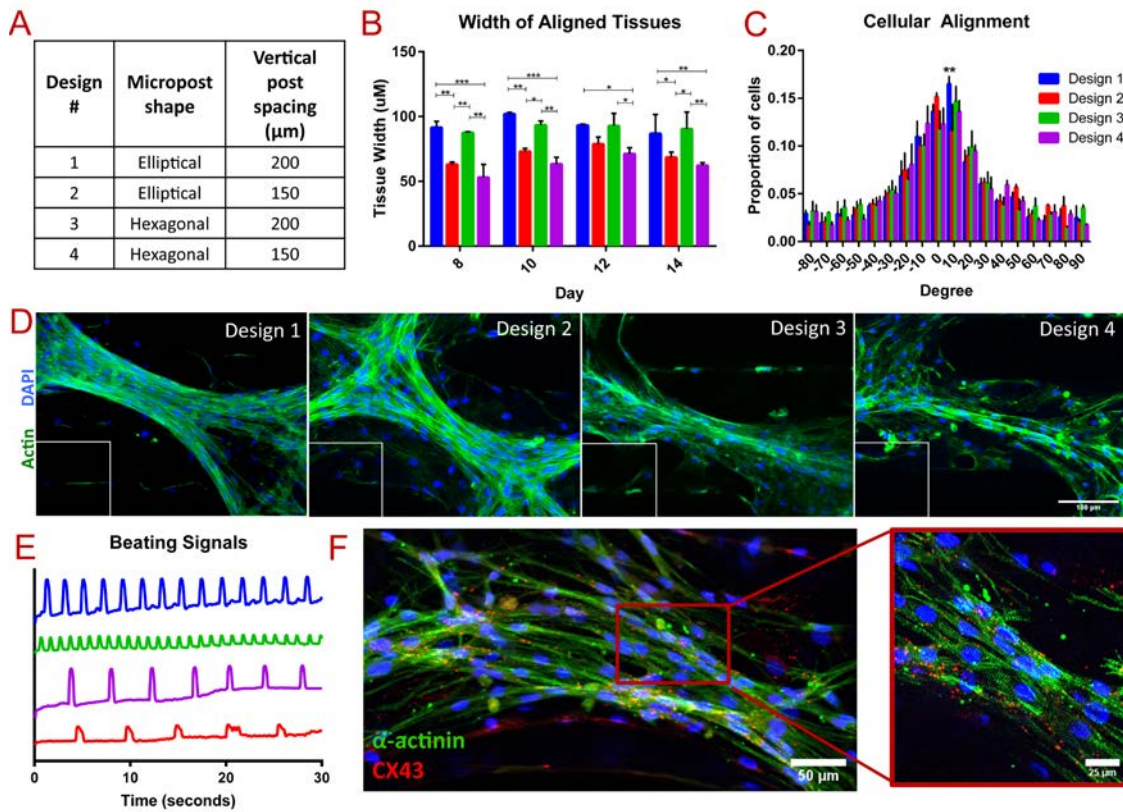


Figure 2.2: Optimization of microfluidic device design parameters with neonatal rat cardiac cells.

(A) Table of microfluidic devices designs with differing post dimensions. (B-F) Characterization of neonatal rat cardiac tissue within each design. (B) Tissue width, (C)

cellular alignment, (D) immunostaining of actin and DAPI with inset as FFT, and (E) representative beating signals from tissues formed within each device. (F) Cardiac-specific marker staining of tissues in Design 1, demonstrating aligned sarcomeres (green) and abundant, localized CX43 (red), with 40X magnification to right. Statistics performed on two-way ANOVA of B) n=2 experiments and C) n=3 experiments.

2.4.3 Cardiomyocyte differentiation and purification from hESCs and hiPSCs

For the formation of 3D cardiac tissues within the optimized design, we differentiated human cardiomyocytes (hCMs) from monolayers of both hESCs and hiPSCs. The differentiation was performed through activation of the canonical Wnt signaling pathway by inhibition of GSK β followed by sequential inhibition of Wnt (Lian et al., 2013). Typically, spontaneous beating initiated from D7-11 of culture. Metabolic selection, based on glucose starvation, was performed from D14-D20 to enrich for hCMs (Sharma et al., 2015). After metabolic selection, the hCMs were replated to eliminate dead cells and debris. Flow cytometry analysis reveals high percentages of hCMs, with a representative flow cytometry histogram in Figure 2.3A showing a cardiac differentiation at 90.8% cTnT⁺, and an average overall differentiation efficiency of 85.5% cTnT⁺ cells. This data was further corroborated with high GFP expression in CMs differentiated from transduced hESCs with GFP linked under the cTnT promoter, and IF staining for cTnT among hiPSC-CMs (Appendix Figure A.3). hCMs differentiated from hESCs and hiPSCs reveal indistinguishable morphologies and protein expression as demonstrated in Figures 2.3B-D. The resultant tissue populations reveal islands of dense hCM populations

(SAA⁺), with surrounding populations of isolated non-myocytes (Vimentin⁺). IF characterization of the non-CMs, consistent with previous work (D. Zhang et al., 2013), reveals 65.86% CFs (vWF⁻/Vim⁺) and 31.24% ECs (vWF⁺/Vim⁺). The combined strategy for differentiation and purification led to consistent, highly pure hCM populations, that were subsequently incorporated into the optimized microfluidic chip.

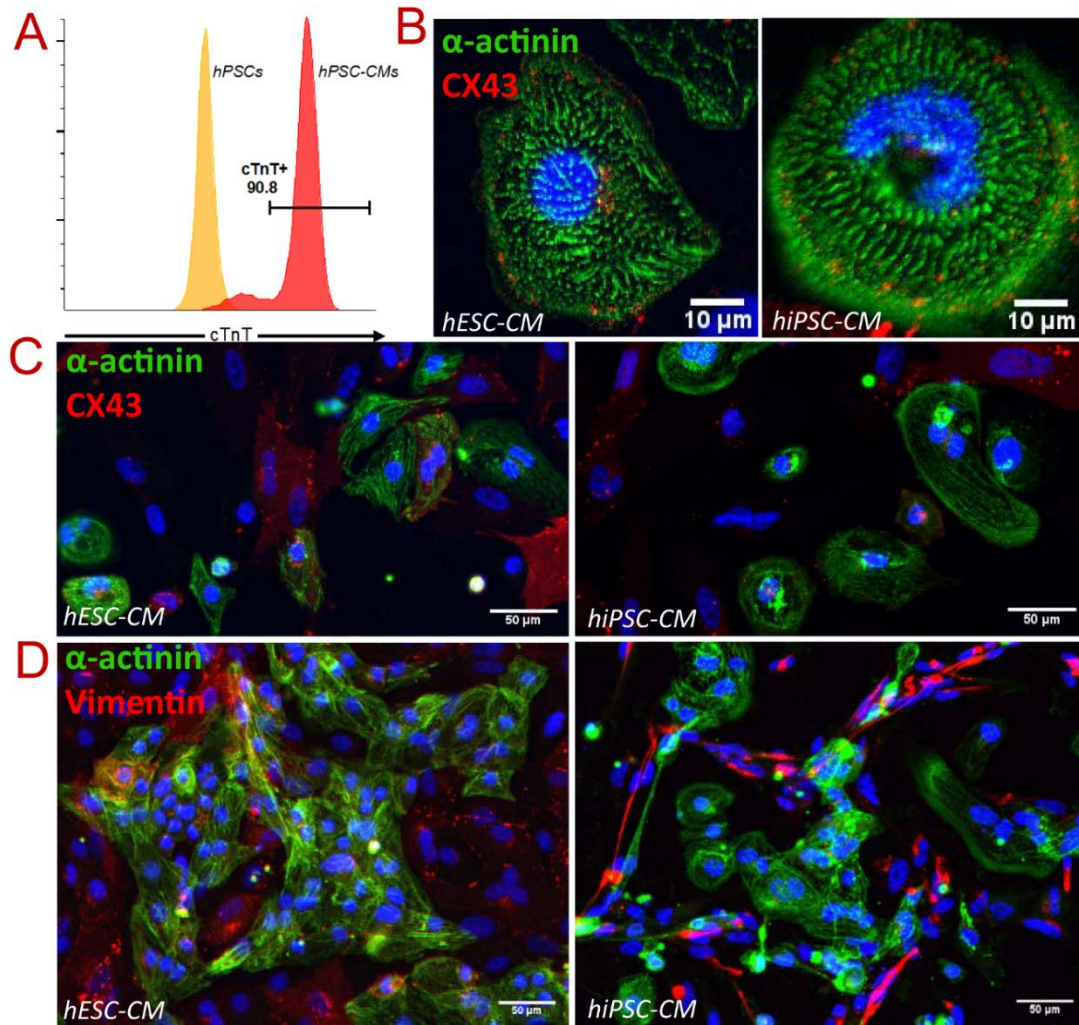


Figure 2.3: Characterization of cardiomyocytes (CMs) differentiated from both hESCs and hiPSCs.

(A) Flow cytometry plot of differentiated CM population, showing >90% cTnT expression. (B) Cardiac-specific expression of hESC (left) and hiPSC (right) differentiated CMs at 40X, and at 20X in (C). (D) Immunostaining of sarcomeric α -actinin (green) and vimentin (red) for identification of cardiomyocytes and non-cardiomyocytes, respectively.

2.4.4 Generation of 3D organized cardiac tissues from human stem cells

To test formation of 3D human cardiac tissue within the microfluidic chip, the differentiated and purified hCMs were mixed with human CFs (hCFs; as characterized in Appendix Figure A.2), embedded into fibrin:collagen hydrogel, and injected into the optimized microfluidic device of Design 1. The optimal conditions for 3D tissue formation, as identified with rat cardiac cell culture, were initially tested for the creation of human cardiac tissue from hPSC-CMs. Specifically, the culture duration and device design values were kept consistent. The co-culture ratio was again validated with hPSC-CMs, demonstrating enhanced alignment with tissues formed with 4:1 CM:CF over 8:1 and 1:0 CM:CF (Appendix Figure A.6). To that end, our data strongly suggests that the co-culture ratio of 4:1 CM:CF optimized with rat tissues was equally optimal for human cardiac tissue formation, and was thus sustained for all subsequent experiments. However, due to low gel compaction and significant variation in gelling times, the hydrogel formulation was changed to a mixture of collagen type I (2 mg/mL) and Matrigel® at a ratio of 80:20 as it showed highest cell elongation, consistency and easier handling, and better represented the adult myocardium, as its main ECM component is

collagen (Guyette et al., 2016). In addition, cell density was slightly increased (from 30 to 35×10^6 cells/mL). Apart from devices embedded with microposts, devices of identical design, except lacking the microposts, were fabricated in order to serve as 3D co-culture controls, to specifically isolate the effect of micropost presence on tissue formation, alignment, and function.

After two weeks of culture, immunofluorescent (IF) staining of cardiac tissues within both types of devices (i.e. with and without the posts) was performed, to assess cardiac tissue composition, integrity, and structure, as well as individual cell structure (Figure 2.4). The tissues formed within devices without the posts exhibit random, unorganized structure in both hESC- and hiPSC-derived cardiac tissues, as demonstrated through F-actin cytoskeletal staining and corresponding FFT analysis (Figure 2.4A). Additionally, cardiac-specific marker staining revealed round hCMs with disarrayed sarcomeres and non-localized CX43 in these no-post devices (Figure 2.4B), a phenotype consistent with immature hCMs (X. Yang et al., 2014). However, the tissues formed within devices with the posts notably exhibited highly aligned structure, as demonstrated from F-actin staining and FFT analysis (Figure 2.4C). Additionally, two weeks of culture within the device was sufficient in attaining a similar degree of anisotropy as when culture was extended to three weeks, as level of tissue alignment within each respective condition (i.e., with or without posts) is sustained. This confirmed that the Day 14 experimental time point was appropriate to achieve the high level of anisotropy within the device with posts to perform functional and molecular-level analyses. In addition,

tissues formed in devices with posts at both time points were significantly more aligned than either time point of no post conditions (Appendix Figure A.7).

Further analysis of anisotropic tissues formed within devices with the posts revealed that the cells present with organized cytoskeletons, elongated structure, abundant striated sarcomeres, and localized CX43 expression along the cell border (Figures 2.4D-F), regardless of location among posts. Notably, tissues within the vertical spacing of posts were highly aligned and condensed (Appendix Figure A.8A), in contrast with the formation of nodes of cardiac tissue in the horizontal spacing between posts (Appendix Figure A.8B). To determine the composition of the cardiac populations at day 14, IF was performed to distinguish the CFs/non-CMs from the CMs, through positive staining for vimentin and sarcomeric α -actinin, respectively. hCFs were identified throughout the tissue within both types of devices, moreso than in 2D space-limited monolayer conditions. Specifically, cell population composition of cardiac tissues was quantified based on IF in each condition and lower CM:CF ratios were demonstrated in devices with and without posts (Appendix Figures A.9A-D, p-value for posts to 2D as 0.1201, p-value for posts to no posts as 0.1338, p-value for no posts to 2D as 0.3328). Additionally, IF revealed that hCFs had proliferated onto the surrounding glass and PDMS, both within the tissue region and in the inlet/outlet ports of both types of devices (Appendix Figures A.9B-C). These values were omitted in CM:CF ratio quantification, as only the areas of the device with the hydrogel-encapsulated cardiac tissue were imaged and considered.

The reason for resultant decreased CM:CF ratio within the 3D device conditions, and maintenance of CM:CF ratio in age-matched 2D culture after the two-week period, can be hypothesized to be due to multiple factors. First, the cell population is cultured at maximum confluency in 2D, thereby it is expected that the fibroblasts undergo contact inhibition and arrest their proliferation (Eagle & Levine, 1967), leading to maintenance of initial cell composition. Secondly, fibroblasts are sensitive to mechanical stress and may respond to stretch within the 3D ECM in device conditions, which in turn activates various pathways, leading to proliferation, deposition of ECM, and release of growth factors (Camelliti, Borg, & Kohl, 2005). Thirdly, CMs have also been demonstrated to release growth factors in response to stretch, that in turn induce fibroblast responses, normally attributed to CF response to mechanical stimulation, such as proliferation, ECM deposition, and gene expression regulation (Camelliti et al., 2005; MacKenna, Summerour, & Villarreal, 2000). Therefore, the CFs may be experiencing multiple stimuli within the 3D culture environment of the microfluidic platform which upregulate their proliferation, while the CFs in 2D experience contact inhibition and halt proliferative processes, leading to the observed decrease in CM:CF ratio in 3D, and, on the other hand, maintained cellular ratio in 2D upon two weeks of culture.

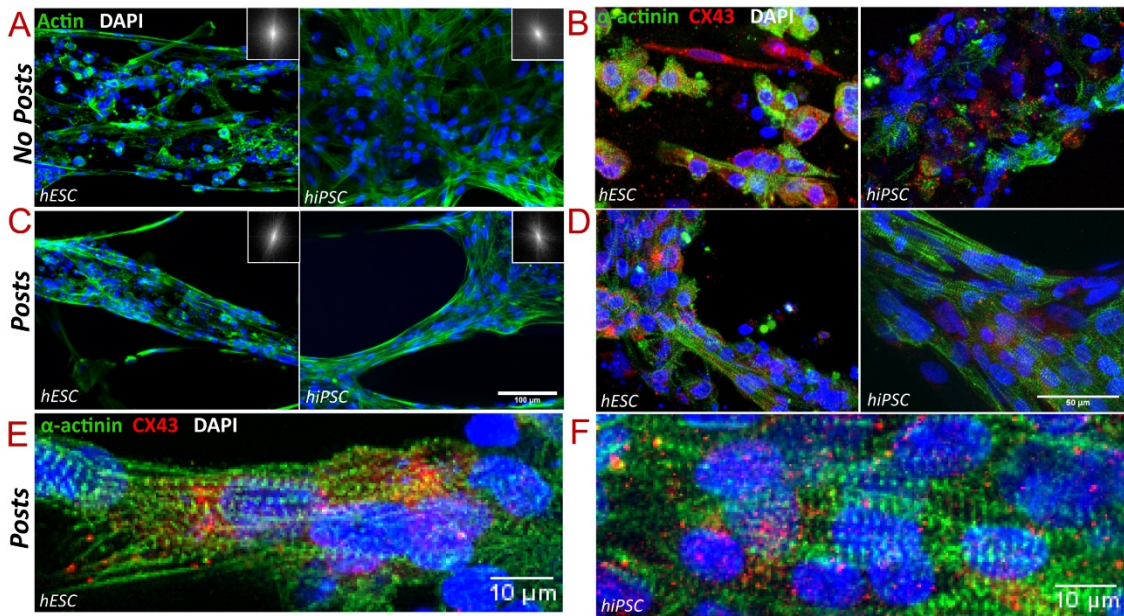


Figure 2.4: Structural properties of human stem cell-derived cardiac tissues formed within microfluidic devices with and without the microposts.

(A, B) Tissues in devices without the posts, showing cytoskeleton through immunostaining of actin and DAPI (A) and cardiac-specific markers through immunostaining of sarcomeric α -actinin and CX43 (B). (C-E) Tissues in devices with the posts, showing cytoskeleton (C) and cardiac-specific markers (D-E). (E) Magnified view of sarcomere alignment and CX43 expression of tissue within devices with posts.

2.4.5 Gene expression analysis of human cardiac tissues

Upon formation and assessment of the phenotype of 3D human tissue within the microfluidic chip, gene expression analysis was performed to assess changes in tissue-level transcription, as an indicator for maturation state, due to extended culture within each condition. To serve as a population control, gene expression values were compared

to the respective cardiac cell population immediately before insertion (deemed as D0). In addition, monolayers of 4:1 CM:CF were cultured in standard Matrigel®-coated 2D plates for the experimental period (i.e., 14 days) to serve as age-matched 2D comparison to the tissues formed within devices (Figure 2.5A). The panel of genes that were assayed includes those important for cardiac tissue function and structure. The genes were broadly classified as involved in either calcium handling, structural, or conduction, in order to isolate the biological processes that may be affected. Incorporated in this panel were maturation-specific genes, deemed as those demonstrated with significantly higher expression in adult over fetal hearts and hPSC-CMs, including: ACTN2, ATP2A2, CASQ2, CAV1.2, CAV3.1, HCN1, HCN4, KCNQ1, MYH7, PLN, RYR2, S100A1, TNNT2, and TNNT2 (Jiang et al., 2018; X. Yang et al., 2014). Average values of fold change from D0 of tissues from devices with posts, without posts, and age-matched 2D monolayers were plotted in an expression heatmap, with row z-score displayed (Figure 2.5B). Overall, the 3D tissues formed within the microfluidic chip, both with and without posts, demonstrate more upregulation of genes than those in the 2D monolayer, suggesting that 3D hydrogel and co-culture with CFs over two weeks influences genes important in cardiac function. Specifically, tissues in age-matched 2D monolayers only displayed a significant upregulation of MLC2V (Figure 2.5C). This result coincides with the findings that co-culture of CMs with CFs, as well as extended culture time, promote a more mature CM phenotype (Parrag, Zandstra, & Woodhouse, 2012).

Within devices without posts in comparison to D0, tissues demonstrated an upregulation in some cardiac-related genes, with significant upregulation in the

conduction marker KCNQ1, calcium handling marker CAV1.2, and structural marker TNNI3 (Figure 2.5D). In order to investigate the additional effect of anisotropy on cardiac tissues within identical 3D hydrogel culture and CF presence, gene expression of tissues formed within the microfluidic chip with posts, in comparison to D0, was further analyzed. These highly aligned cardiac tissues within our microfluidic chip exhibited extensive significant upregulation, particularly in “maturation-specific” genes (Figure 2.5E). These genes included HCN1, KCNQ1, CAV1.2, CAV3.1, PLN, and RYR2 (Jiang et al., 2018), which participate in calcium handling and conduction-specific processes. Therefore, the engineered cardiac tissues within our 3D microfluidic chip demonstrated an upregulation in both calcium handling and conduction processes, with significant trends demonstrated particularly for maturation-specific genes. These results correspond to the exhibited enhanced cell and tissue structure due to induction of 3D tissue anisotropy, revealing the capability to mature hPSC-derived cardiac tissue within our microfluidic chip. Additionally, expression levels of some structural-specific genes were significantly upregulated, including GJA5 and α MHC. GJA5 translates CX40, which has been demonstrated between CF:CF and CM:CF junctions (Johnson & Camelliti, 2018), therefore upregulation of GJA5 may signify higher presence of hCFs in 3D device conditions, which is corroborated with presence of more fibroblasts/non-myocytes through IF staining of vimentin and the resultant decrease in calculated CM:CF ratio in 3D conditions (Appendix Figures A.9B-D). In contrast, α MHC expression decreases during heart development, which is inconsistent with our model, as well as many other *in vitro* models, highlighting the future need to investigate myosin isoform switching, and

how it can be better replicated *in vitro* (Ivashchenko et al., 2013; Lundy et al., 2013). On the other hand, we demonstrate an average elevated expression in devices with posts of β MHC (not significant).

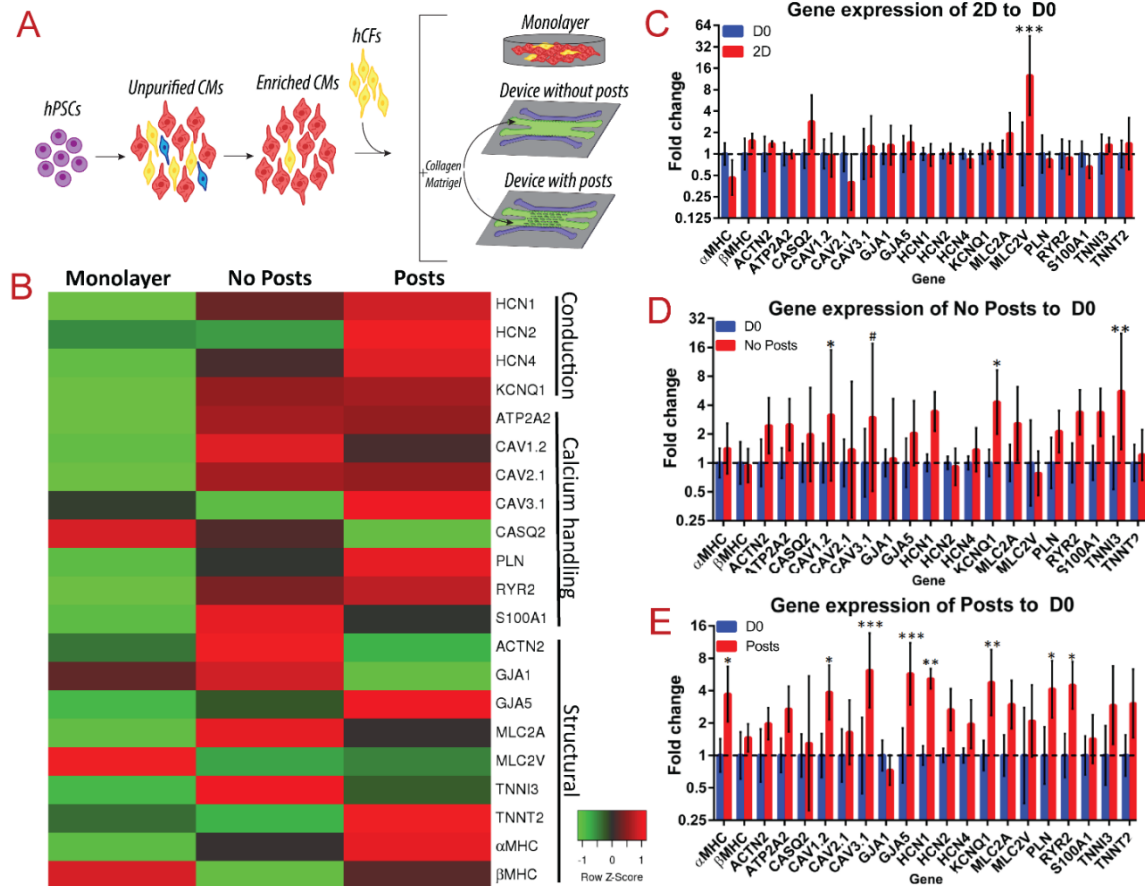


Figure 2.5: Gene expression analysis of human stem cell-derived cardiac tissues in monolayer and microfluidic devices.

(A) Schematic of formation of tissues within devices and age-matched monolayer. (B) Heatmap of fold changes of all conditions to D0, with z-score displayed. (C) Gene expression of 2D age-matched monolayers compared to before insertion. (D) Gene expression of tissues in devices without posts compared to before insertion (D0). (E)

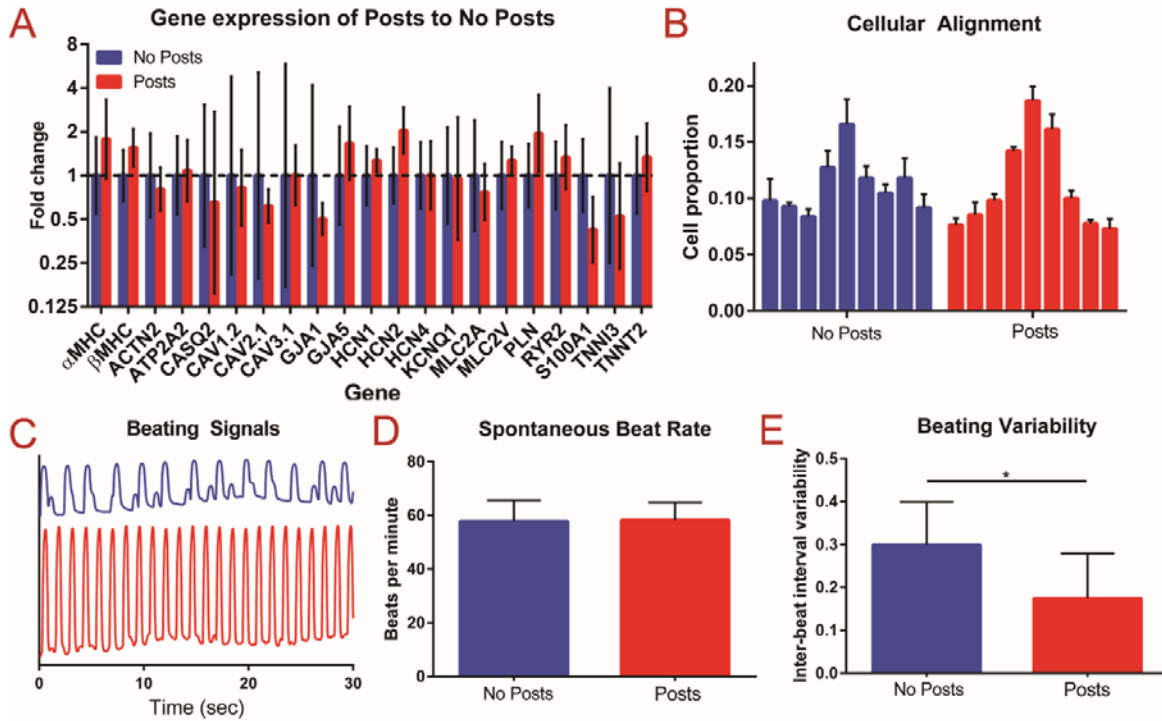
Gene expression of tissues in devices with posts compared to before insertion (D0).

Statistics performed on ANOVA of DCT values of $n \leq 4$ experiments, with P-values:

* <0.05 , ** <0.01 , *** <0.001 .

In order to specifically identify effect of microposts on tissue function, tissues grown in devices with and without the posts were directly compared. Although more genes are significantly upregulated in the post condition than in no posts condition in comparison to D0, gene expression between devices with and without posts was not significantly different for the chosen panel when the device conditions are directly compared (Figure 2.6A). However, tissues in the devices with posts demonstrate a more normal distribution of cell alignment around the alignment axis (at 0°) than the no post condition, suggesting a higher degree of cell alignment in tissues formed within devices with posts (Figure 2.6B), due to the formation of repeated pores throughout the tissue that also enhance media and thus nutrient/oxygen diffusion. The enhanced cell and tissue structure and corresponding protein expression reveal that although the microposts do not appear to affect expression of the genes that were analyzed, they reveal a pertinent role in cardiac tissue structure and formation that may affect tissue function. To that end, we further investigated spontaneous beating signals as a characteristic of tissue function from real-time videos of tissues in post and no post conditions (Figure 2.6C, Appendix Movies A.5-7). The peaks of tissue contraction from these signals were extracted to determine spontaneous beat rate and inter-beat interval variability, deemed a measure of spontaneous contraction synchronicity. Tissues grown within both types of chips (i.e., with and without the posts) exhibit similar physiologically relevant beating rates,

regardless of chip design (Figure 2.6D). However, significantly larger inter-beat interval variability, or more inconsistent contraction patterns, was demonstrated in tissues grown in devices without posts in comparison to those with posts (p-value of 0.03002) (Figure 2.6E). This finding demonstrates that the contractile function of these tissues differs



based solely on microchip design.

Figure 2.6: Comparison of tissues cultured in devices with and without microposts.

(A) Gene expression, (B) cellular alignment, (C) representative spontaneous beating signals, (D) spontaneous beating rate, and (E) beating variability, calculated by inter-beat interval variability, of tissues grown for two weeks in devices with and without posts.

Statistics performed on ANOVA of hESC and hiPSC tissues for B) n=5 experiments and for D) and E) n=10 experiments, with * denoting p-value<0.05.

To further investigate the tissue functionality, spontaneous calcium transients were recorded and analyzed for hPSC-derived 3D cardiac tissues formed after two weeks of culture within the microfluidic devices with and without posts. Within each recorded tissue area, the fluorescent intensity of calcium spikes (F) for five regions of interest was divided by background intensity (F_0) and plotted over a period of 30 seconds (Figures 2.7A, B). The resultant calcium transients revealed highly variable calcium release patterns for tissues within devices without posts, that were asynchronous among the different subregions (Figure 2.7A, Appendix Movie A.8). On the other hand, tissues developed within devices with posts demonstrated extremely consistent calcium transients, that were synchronous to the calcium spikes of all other subregions (Figure 2.7B, Appendix Movie A.9). These findings further confirm that this microfluidic device promotes enhanced cell-cell communication and electrical signal propagation. Specifically, in direct comparison to an isotropic 3D control, engineered tissues demonstrated calcium handling properties and spontaneous contractions with enhanced synchronicity, revealing the particular effects of topography-induced alignment on tissue maturation.

Furthermore, the responsiveness of the engineered cardiac tissues was tested through administration of the β -adrenergic agonist, epinephrine (i.e., adrenaline), to probe the physiological relevancy of the 3D formed tissue within the platform and its capabilities for drug response studies. Both tissues formed within devices with and without the posts demonstrated a positive chronotropic effect to epinephrine dosing (Figure 2.7C), however tissues within the posts condition exhibited more organized

spontaneous contraction patterns in response to epinephrine in comparison to tissues within devices without posts. Additionally, the tissues developed within the demonstrated microfluidic device with posts responded to epinephrine dosing with a significantly higher change in BPM than tissues in the no posts condition (p-value of 0.04056) (Figure 2.7D), further demonstrating enhanced clinical relevancy of the proposed microfluidic model.

Therefore, tissues grown in devices with posts exhibit enhanced synchronicity, presenting more connected and thus augmented electrophysiological function, which may be due to the enhanced localization of gap junctions and coordinated tissue structure. This suggests that the cells in devices with posts undergo mechanotransduction, initiated from the interaction with the microposts, inducing changes either a) of translational and/or post-translational levels of particular proteins, or b) of the transcription of alternative genes that were not studied herein and require further analysis. The cells that comprise tissues formed among the microposts demonstrated elongated shape, therefore it is also plausible that pathways involved in physiologic hypertrophy are activated (Jaalouk & Lammerding, 2009; Stansfield et al., 2014). Likewise, as focal adhesions connect the ECM to the cytoskeleton and are involved in promoting and directing myofibril assembly (Bray et al., 2008; Jaalouk & Lammerding, 2009), the presence of extensive sarcomere alignment in chips with the microposts suggests that processes involving focal adhesion kinases (FAKs) are specifically influenced within this culture condition. Particularly, in response to the stretch sensed from micropost-induced pore formation, stretch-related receptors such as integrins may be activated, that in turn signal certain kinases, among

such are FAKs and mitogen-activated protein kinases (MAPKs) (Pasqualini, Nesmith, Horton, Sheehy, & Parker, 2016; Stansfield et al., 2014). Signaling by these different kinases generally leads to a cascade of events, including activation of various proteins that activate transcription factors that translocate to the nucleus to ultimately affect gene transcription. Therefore, it is plausible that transcription of specific genes affected through these mechanotransduction-related pathways, in addition to available levels of related proteins, are influenced in the different chip conditions. The exact mechanism that connects micropost-guided alignment and enhanced contractile function will be a suitable subject of future study. Nevertheless, due to the combination of anisotropic structure, 3D culture, and exposure to supporting cells (CFs), tissues grown in devices with the microposts exhibit the most significant upregulation of an abundance of cardiac-specific maturation genes in comparison to D0 tissues, demonstrating with elongated CMs, striated parallel sarcomeres, localized gap junction staining, and synchronous whole-tissue contraction. Additionally, tissues within these devices demonstrate physiologically relevant functionalities, as revealed through synchronous calcium transients, and positive chronotropy in response to β -adrenergic agonist.

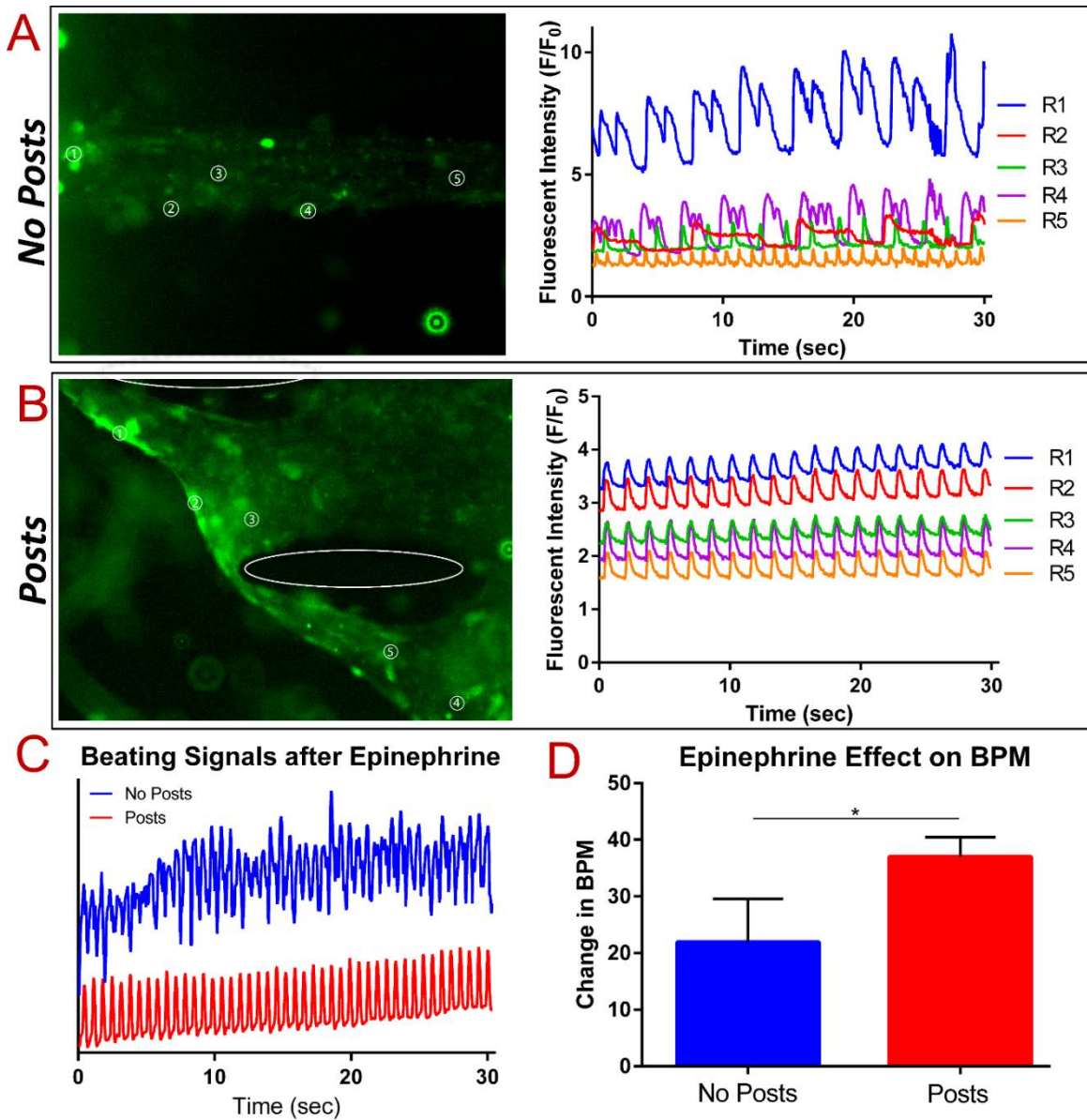


Figure 2.7: Functional assessment of human stem cell-derived cardiac tissues within devices with and without posts after 14 days of culture.

Calcium transients and extracted related frequency signals of intracellular change in concentration of Ca^{2+} for (A) devices without posts and (B) devices with posts, with R1-R5 representing regions 1-5. Responsiveness of tissues to epinephrine, with

representative beating signals in (C), and corresponding (D) changes in spontaneous BPM. Statistics were performed through two-sided, paired t-test of n=3 experiments of hiPSC-derived tissues, with p-value: $* < 0.05$.

Future works could further improve the platform for enhanced functional measurements particularly for those of great importance to cardiac tissue studies, such as contractile force measurements. In order to fulfill the needs for real-time measurement of force in disease modeling and pharmaceutical testing applications, an innate method to measure contractile force is of great importance. Future works shall investigate the use of innate, free-standing micropillar arrays, capable of force measurement, similar to the approach described in (Schaaf et al., 2011), within the microfluidic device to allow for real-time force monitoring. Additionally, to enhance the platform's ability to model the adult myocardium, such as induction of a pronounced myosin isoform switch from β to α . For example, sustained electrical conditioning has been demonstrated to enhance the electrophysiology and transcriptional signature of hPSC-derived CMs. However, a rather complicated setup is necessary to incorporate sustained external stimulation, and our model is advantageous in its low cost and ease of creation. Similarly, an enlarged version of the platform could be constructed to allow for a large cell population to select for CMs for downstream analyses, however such a platform would negate the many advantages of a microfluidic platform, i.e. high throughput, minimal cell/reagent necessary, and reduced variation with input differentiation populations. To further take advantage of the microfluidic nature of the described platform, a future work involves implantation of

continuous fluid flow through the media channels to enable enhanced nutrient supply and dynamic culture conditions, which have recently been demonstrated to enhance cardiac tissue function (Jackman et al., 2016). Thus, with the many advantages of the proposed platform, taken together with the demonstrated ability to mature and enhance cardiac tissue formation, the design presented herein has great potential to serve as a physiologically relevant model for cardiac disease and tissue studies. As this platform has been validated for use with CMs differentiated from hiPSCs, there exists the possibility in future works to model genetic diseases through CRISPR/Cas9 gene editing, as well as patient-specific diseases, through reprogramming of patient fibroblasts to hiPSCs. Additionally, the microfluidic nature of the platform allows for the implementation of precise molecular gradients, as observed throughout native tissues and organs, therefore allowing diseases derived from external insult (i.e., hypoxia, drugs, stimulants) to be modeled. The enhanced mature nature of the tissue provides a model with more physiological relevance than hPSC-derived CMs to the human myocardium.

2.5 Conclusion

In this study, we demonstrated the precise design of a microfluidic platform for successful 3D cardiac tissue formation and function, developed first with rat-derived cardiac cells, and then validated with both hESC- and hiPSC-derived cardiomyocytes. To enhance the physiological complexity, CMs were co-cultured with interstitial cardiac fibroblasts (CFs) within hydrogels embedded in the platform, resulting in cardiac tissues with a high degree of cellular interconnectivity and functionality, as demonstrated

through gap junction localization, sarcomere organization and synchronicity in spontaneous contraction. Importantly, incorporation of complex 3D micropost architecture within the tissue region of the microfluidic chip significantly enhanced the tissue organization, with the added potential for high throughput experimentation with minimal necessary cells and corresponding reagents. We demonstrated extensive characterization of co-cultured anisotropic cardiac tissues grown for two weeks within the proposed microfluidic chip design. Particularly, our results highlighted that the formed tissues within the chip exhibit mature cellular structure, protein expression as well as an upregulation of genes with roles in tissue structure, calcium handling, and electrical conduction. Interestingly, incorporation of the mesoscopic microposts led to significantly enhanced tissue function as evidenced by increased synchronicity of spontaneous beating. In summary, the 3D cardiac tissues formed within this microfluidic chip present with enhanced structure, function and physiological relevancy that surpass conventional 2D monolayer culture assays, therefore highlighting the great potential of this platform for future disease modeling and predictive drug testing studies.

CHAPTER 3

AIM 2: Incorporate the optimized microfluidic platform to create a model of cardiac ischemia on-a-chip to investigate cellular and molecular response of myocardial tissue under hypoxia

3.1 Abstract

Tissue engineering has enabled the development of advanced and physiologically relevant models of cardiovascular diseases, with advantages over conventional 2D *in vitro* assays. We have previously demonstrated development of a heart on-a-chip microfluidic model with mature 3D anisotropic tissue formation that incorporates both stem cell-derived cardiomyocytes and cardiac fibroblasts within a collagen-based hydrogel. Using this platform, we herein present a model of myocardial ischemia on-a-chip, that recapitulates ischemic insult through exposure of mature 3D cardiac tissues to hypoxic environments. We report extensive validation and molecular-level analyses of the model in its ability to recapitulate myocardial ischemia in response to hypoxia, demonstrating the 1) induction of tissue fibrosis through upregulation of contractile fibers, 2) dysregulation in tissue contraction through functional assessment, 3) upregulation of hypoxia-response genes and downregulation of contractile-specific genes through targeted qPCR, 4) transcriptomic pathway regulation of hypoxic tissues, and 5) cell toxicity in response to ischemia reperfusion injury.

3.2 Introduction

Cardiovascular diseases (CVDs) are the leading cause of death worldwide (Heidenreich et al., 2011; Virani et al., 2020), claiming the life of one person every 36 seconds in the United States ("Underlying Cause of Death, 1999-2018," 2020). During

myocardial ischemia or infarction, aside from loss of cardiomyocytes and impairment of contractile function, ventricular tachyarrhythmia can develop, a common contributor to cardiovascular-related deaths (Ghuran & Camm, 2001). Myocardial infarction (MI) commonly results from ischemia, which is defined as inadequate blood supply due to partial or full blockages of a coronary artery, leading to tissue injury or cell death when the extent of reduction of arterial flow creates an oxygen deficit for tissue energy demand (Lu, Liu, Sun, Zheng, & Zhang, 2015). When ischemic injury causes a complete cut off blood flow to the heart, MI ensues. MI is generally followed by post-infarct heart remodeling characterized by the formation of scar tissue in response to ischemic-death of cardiomyocytes (CMs). Such remodeling, an attempt to restore cardiac output after infarction, can become pathologic, worsen cardiac function, and can lead to heart failure (Nag, 1980).

Drastic changes occur in myocardial tissue in response to profound ischemia including changes in tissue functionality, electrophysiological state, and metabolism. These changes are due to severe impacts on relative energy and oxygen availability which induce a complex biological and pathological cascade of events. Ischemia causes an imbalance between oxygen demand and coronary blood flow (Crossman, 2004), resulting in abnormal metabolic state with increase in lactate production, low pH, and high intracellular Ca^{2+} (Kalogeris, Baines, Krenz, & Korthuis, 2012). Specifically, due to the lack of oxygen, cells cannot perform oxidative phosphorylation and thus rely on anaerobic metabolism, causing a loss of net intracellular ATP and an increase of intracellular H^+ . In response to the drop in pH, the Na^+/H^+ exchanger produces a large

influx of Na^+ ions into the cell as it excretes the excess H^+ . The Na^+ ions are then exchanged for Ca^{2+} by the plasmalemmal $\text{Na}^+/\text{Ca}^{2+}$ exchanger, resulting in an increase in intracellular Ca^{2+} . ATP is necessary to maintain intracellular homeostasis of Ca^{2+} , therefore intracellular Ca^{2+} remains pathologically high in ischemic conditions, due to the depletion of available ATP, resulting in detrimental effects on both cellular structure and function (Nayler, 1981).

Due to the reduction of available ATP, glycolytic enzymes are activated, causing upregulation of glycolysis and resulting in the conversion of glucose to pyruvate (Agrawal, Gupta, Qureshi, & Vishwakarma, 2016; Carmeliet, 1999). However, pyruvate dehydrogenase activity is reduced (Renstrom, Liedtke, & Nellis, 1990), so pyruvate is converted to lactate through oxidation of NADH to NAD^+ (Carmeliet, 1999). Lactate is not further metabolized in the absence of oxygen, resulting in high lactate concentrations. The upregulated levels of anaerobic glycolysis and lactate concentration produce an acidic environment, displacing calcium from its binding site on troponin (Jennings, Reimer, & Steenbergen, 1986; Katz, 1973) resulting in intracellular calcium mishandling and contractile abnormalities (Francis Stuart, De Jesus, Lindsey, & Ripplinger, 2016).

The immediate cellular changes that occur due to myocardial ischemia lead to the suppression of most genes, however a subset of genes, i.e. hypoxia-inducible genes, such as hypoxia-inducible factors (HIFs), are upregulated (Abe, Semba, & Takeda, 2017). Particularly, HIF1 signaling activates a myriad of cascades, and causes the production of angiotensin and $\text{TGF}\beta 1$, which in turn induce differentiation of resident myocardial fibroblasts into myofibroblasts. Myofibroblasts extensively deposit extracellular matrix

(ECM), resulting in the formation of scar tissue, which demarcates CMs from each other. Altogether, myocardial fibrosis and remodeling can lead to desynchronization of heart tissue causing a detrimental effect on contractility. These complex cellular cascades and pathophysiologies that occur in response to myocardial ischemia can result in arrhythmias and potentially heart failure.

Current *in vitro* and preclinical models of human myocardial ischemia present challenges in translating human physiological conditions. 2D *in vitro* assays fail to recapitulate 3D tissue structures, and results from *in vivo* animal models often fail to translate when tested in human clinical trials (Hackam & Redelmeier, 2006). Cardiovascular research has greatly expanded since the establishment and optimization of CM differentiation of human induced pluripotent stem cells (hiPSCs), which has enabled sourcing of human CMs for *in vitro* research. However, hiPSC-CMs are notoriously immature, resembling the fetal state, more so than adult (Jiang et al., 2018; Veerman et al., 2015). As fetal CMs are not sensitive to hypoxia as they rely mainly on glycolysis for their metabolism, it is pertinent to enhance the maturation state of hiPSC-CMs for physiologically relevant disease modeling (Cutts, Nikkhah, & Brafman, 2015; Esmaeili et al., 2021; Patino-Guerrero, Veldhuizen, Zhu, Migrino, & Nikkhah, 2020; Veldhuizen et al., 2019; X. Yang et al., 2014), particularly in modelling ischemic-reperfusion injury (IRI). Recent 2D models have uncovered the importance of maturation in ischemic modeling, for example, a study investigated the use of both immature and mature hiPSC-CMs to model IRI using temporal gradients in oxygen, local pH, and glucose availability (Hidalgo et al., 2018). This study demonstrated the inability of immature hiPSC-CMs to

model the physiological response to IRI. However, CMs that were matured through culture in glucose-free media for 8 days exhibited physiological cell death in response to reperfusion. Therefore, the switch from glycolysis to oxidative phosphorylation that accompanies enhanced maturation state of CMs is pertinent to accurately model their pathological response to hypoxia (Coles et al., 2005; Hidalgo et al., 2018).

To better represent the myocardial structure, 3D *in vitro* models have been used for disease modeling due to their ability to model complex cell- and tissue-level interactions. For example, a study incorporated hiPSC-CMs suspended in a 3D hydrogel among flexible pillars, inducing passive tension on the encapsulated cells (Chen & Vunjak-Novakovic, 2019). Tissues that formed in these conditions after 3 days were immature, while tissues formed for 2 weeks were deemed as mature. IRI was simulated in these constructs through culture in low pH media with high lactate and anoxic gas for 6 hours, then the constructs were supplemented with standard media to simulate reperfusion. The matured constructs responded to reperfusion with pathological cell death levels, further confirmed through increased expression of caspase-3, while the immature constructs were much less sensitive.

In order to establish the conditions for ischemia, most of the mentioned studies have incorporated low pH and/or high lactate levels, in addition to anoxia/hypoxia. While physiologically relevant, high lactate and H^+ concentrations are the metabolic consequence of ischemic conditions, not necessarily the direct insult (Graham et al., 2004). Therefore, if the concentrations are elevated before induction of hypoxia, the already high levels are likely to further increase as the cells respond to the low oxygen

environment. In extended low-flow ischemia, metabolites and waste products accumulate as duration of deprivation of flow and oxygen continues, representing a dynamic environment.

In addition, many of the currently available models incorporate a mono-culture of CMs. In the healthy heart, human cardiac fibroblasts (hCFs) are vital to sustain normal function, through preserving the structural integrity and responding to mechanical, electrical and biochemical stimuli (Porter & Turner, 2009; Talman & Ruskoaho, 2016). During injury, such as myocardial ischemia, fibroblasts are essential in the cellular response; specifically, fibroblast populations expand and become the majority of cellular constituents in the infarcted area (Talman & Ruskoaho, 2016). They differentiate into myofibroblasts and secrete ECM, express contractile proteins, and respond to autocrine and paracrine factors (Elson, Qian, Fee, & Wakatsuki, 2019; Porter & Turner, 2009; van den Borne et al., 2010; Watson et al., 2014; H. Zhao et al., 2014), resulting in tissue stiffening and remodeling within the heart that can prove averse to its function (Opie, Commerford, Gersh, & Pfeffer, 2006; Porter & Turner, 2009; Talman & Ruskoaho, 2016; van den Borne et al., 2010). Therefore, to accurately model the molecular and cellular changes that occur during myocardial ischemia, the presence of cardiac fibroblasts is essential.

In this work, our goal was to simulate ischemia-induced cardiac injury due to extended restriction in blood flow during a myocardial infarction in a heart on-a-chip platform, to serve as a potential model for downstream biological mechanistic studies. Specifically, we utilized our recently developed novel heart on-a-chip that enables

anisotropic 3D structure (Figures 3.1B,C) of human cardiac tissue within a collagen-based hydrogel. As fibroblasts are sensitive to the hypoxic environment and contribute to the pathological response of the myocardium (Johnson & Camelliti, 2018), the co-cultured nature of this system (combination of CMs differentiated from hiPSCs and hCFs) reinforces the physiological relevancy of the platform for disease modeling. To replicate native myocardial conditions during an ischemic insult, we exposed matured cardiac tissues within the microfluidic devices to various environmental oxygen conditions (Figure 3.1A). Previous studies used traditional cell culture oxygen levels to model “physioxia”, however atmospheric level of oxygen is 21%, while normal oxygen levels in the myocardium are around 5-10% (Winegrad, Henrion, Rappaport, & Samuel, 1999). Therefore, in this study, we designated a hyperoxia condition, in which tissues are exposed to normal cell culture levels, i.e., 21% O₂, in addition to a physioxia condition in which tissues were exposed to 5% O₂. Hypoxia was defined as 1% O₂. To better represent the myocardial environment in ischemia, we exposed cardiac on-a-chip tissues to these different oxygen environments for 24 hours without wash out, to simulate accumulation of metabolites for dynamic change of pH and accumulation of lactate. The resultant tissues were analyzed for differential gene expression, fibrotic response, and contractile function to characterize the effect of hypoxia within the heart on-a-chip. Further mechanistic biological studies were performed through RNA-sequencing of the mRNA transcriptome to highlight differentially regulated pathways implicated in ischemic injury. In light of the reported findings, we demonstrate our developed heart on-

a-chip as a suitable platform for modeling the pathophysiology of cardiac tissue after ischemia and demonstrate its potential for other disease modeling applications.

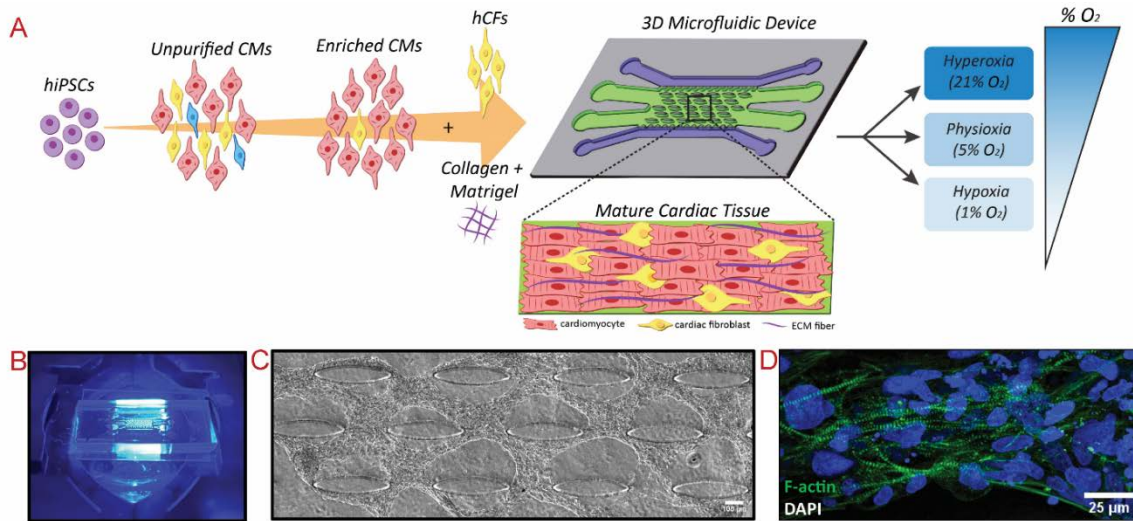


Figure 3.1: Experimental schematic of modeling myocardial ischemia within microfluidic device platform and formation of aligned cardiac tissue before disease modeling.

(A) Schematic of cardiomyocyte differentiation, co-cultured with cardiac fibroblasts, and encapsulated within a collagen: Matrigel hydrogel before injection into microfluidic device. After 13 days of culture, the cells form aligned tissues around the embedded microposts, and are further exposed to the different experimental conditions. (B) Image of microfluidic device on microscope stage. (C) Phase contrast image of aligned human cardiac tissue after 14 days of culture within microfluidic device. (D) Actin-stained tissues after 14 days of culture show well-defined, striated sarcomeres.

3.3 Materials and Methods

3.3.1 Microfluidic device fabrication

Photolithography and soft lithography techniques were utilized to create polydimethylsiloxane (PDMS)-based microfluidic devices from silicon wafers with SU8 features, consistent with our previous work (Nagaraju et al., 2018; Peela et al., 2017; D. Truong et al., 2019; D. D. Truong et al., 2019; Veldhuizen et al., 2020). Briefly, SU8 2075 was spin-coated on 4" silicon wafers to a thickness of 200 μm , then overlaid with a transparent mask with the device design and exposed to UV, using an EVG 620 aligner. The wafer was developed, prepared for soft lithography through salinization, then coated in PDMS, which was further degassed and cured at 80°C for 1.5 hours. The PDMS channels were peeled off the wafer, then prepared through creation of inlet and outlet ports. Devices were formed through bonding of PDMS channels to coverslips with oxygen plasma. The devices were sterilized through two rounds of autoclave and dehydrated at 80°C overnight before tissue culture.

3.3.2 Human cardiac fibroblast culture

hCFs (Lonza) were cultured in Fibroblast Growth Medium-3 (FGM-3) within T75 cm^2 flasks and sub-cultured with 0.05% Trypsin+EDTA up to passage 10.

3.3.3 Human stem cell culture and cardiomyocyte differentiation

hiPSCs (IMR90-4, WiCell (Yu et al., 2007)) were cultured in mTeSR1 media for 3 passages before CM differentiation. The differentiation protocol was used as described in our recent publication (Veldhuizen et al., 2020), with a range of 7-10 μM of CHIR99021 utilized to initiate differentiation through Wnt activation on Day 0. On Day 3, the Wnt pathway was inhibited with 5 μM IWP2 until Day 5. From Day 7-13, hiPSC-

CMs were cultured in RPMI+B27+insulin. On Days 13 and 16, the cells were washed with PBS 1X, then cultured in RPMI minus glucose +B27+insulin, supplemented with 4 mM lactate, to purify for hiPSC-CMs. The cells were recovered on Day 19 with culture in RPMI+B27+insulin. On Day 21, the hiPSC-CMs were replated, using TrypLE Express to dissociate, into fresh Matrigel-coated 6-well plates, to further purify the hiPSC-CMs and remove dead cells/debris. The purified hiPSC-CMs were used for 3D cardiac tissue formation within microfluidic devices after Day 23 of *in vitro* differentiation.

3.3.4 Development of 3D co-cultured anisotropic cardiac tissue on-a-chip

Co-cultured cardiac tissues encapsulated in a 3D collagen-based matrix were formed as previously described (Veldhuizen et al., 2020). Briefly, hCFs were washed with PBS 1X, incubated in Trypsin at 37°C for 4-5 minutes, then collected, buffered with an equal volume of FGM3, and centrifuged at 250 x g for 4 minutes. The supernatant was aspirated and the hCFs were resuspended in FGM3 at a density of 75×10^6 cells/mL. Similarly, hiPSC-CMs were washed with PBS 1X, incubated in TrypLE at 37°C for 10 minutes, then collected, buffered with an equal volume of RPMI+B27+insulin, and centrifuged at 300 x g for 3 minutes. The supernatant was aspirated and the hiPSC-CMs were resuspended in 5 mL of RPMI+B27+insulin, then centrifuged again at 300 x g for 3 minutes, to sufficiently wash the CMs of residual TrypLE. The supernatant was aspirated, and the hiPSC-CMs were resuspended at a density of 75×10^6 cells/mL in fresh RPMI+B27+insulin.

The CMs and CFs were mixed at a 4:1 ratio, then suspended within a 2 mg/mL collagen hydrogel, supplemented with 20% Matrigel as optimized in our previous work

(Veldhuizen et al., 2020). Then the cell:hydrogel mixture was carefully injected into the tissue channel of sterilized microfluidic devices. The devices were flipped, then incubated for 9 minutes at 37°C within larger petri dishes filled with DI water to maintain a humidified environment. After 9 minutes, the devices are placed in the hood and flipped upright, then placed back in the incubator for another 9 minutes to complete hydrogel polymerization. RPMI+B27+insulin was added to the media channels, and media was changed every day.

For 2D experiments, a 4:1 CM:CF cell suspension was seeded on Matrigel-coated coverslips within a 6-well plate for the entire experimental period. The coverslips were supplemented with RPMI+B27+insulin, and media was changed every other day. These samples served as the 2D control for BioTracker 520 Green Hypoxia Dye validation and fibrotic marker immunostaining.

3.3.5 Cardiac tissue exposure to various oxygen levels

On Day 13 of culture within the microfluidic heart on-a-chip platform, the devices were incubated for 24 hours according to the designated experimental condition. Specifically, the “hyperoxia” devices were maintained in a standard tissue culture incubator at 21% O₂, while the “hypoxia” devices were maintained in a separate tissue culture incubator at 1% O₂, both humidified with 5% CO₂. An environmental chamber was utilized with a corresponding premade gas to establish the “physioxia” condition. Specifically, the devices were placed in the environmental chamber, which was then flushed with compressed gas, with a composition of 5% O₂, 5% CO₂, and 90% N₂, for 5 minutes. The inlet and outlet ports were closed, and the entire chamber was placed in an

incubator set at 37°C for the 24 hr culture period. Within each condition, 3-4 devices were stored in each medium-sized petri dish, which were placed within a large petri dish filled with sterile DI H₂O to maintain a humidified environment.

3.3.6 Validation of oxygen levels

To verify the different levels of oxygen at the cellular level within the experimental conditions, a fluorescent imaging probe based on reductase activity, BioTracker 520 Green Hypoxia Dye, was utilized. As per the manufacturer's protocol, 25 µg of desiccated BioTracker Dye was resuspended in 43 µL of DMSO to make a 1 mM stock solution. The stock solution was further diluted in culture media, i.e. RPMI+B27+insulin, to make a 5 µM working solution. On Day 13, the 2D co-cultures of CMs and CFs were washed twice with PBS 1X, then incubated in 5 µM working solution of BioTracker for 1 hr in the designated oxygen condition. The stain was then aspirated and the cells were washed with PBS 1X, before placed in fresh RPMI+B27+insulin and incubated again for 3 hrs in the designated oxygen condition, after which they were imaged via Zeiss fluorescent microscope.

3.3.7 Reperfusion and reoxygenation

In order to study reperfusion and reoxygenation on cardiac tissues, after exposure to the varying oxygen levels, the devices were subsequently subjected to three different conditions: 1) no reperfusion, 2) 1 hour of reperfusion, or 3) 24 hours of reperfusion. For no reperfusion condition, the tissues were removed from their designated oxygen conditions, then immediately imaged or processed for their according assays. For either 1

hour or 24 hours of reperfusion, the tissues were removed from their oxygen conditions, then the media was replaced with warmed RPMI+B27+insulin and incubated in a standard tissue incubator for either 1 hour or 24 hours, respectively, then the tissues were processed for their according assays.

3.3.8 Microscopy

Phase contrast and immunofluorescence images were acquired using Zeiss Axio Observer Z1 equipped with Apotome2 (Zeiss) and ZenPro software. Time-lapse imaging of 30 seconds was recorded at 10X objective at 37°C on Day 14 to analyze spontaneous contraction of the 3D tissue inside the chip immediately after removal from experimental oxygen conditions. To calculate inter-beat interval variability of spontaneous contraction, the method described previously was utilized (Veldhuizen et al., 2020). Briefly, contraction peaks were extracted, and the time interval between peaks was determined. The standard deviation of the inter-beat interval was calculated and deemed the measure of inter-beat interval variability.

3.3.9 Immunofluorescent (IF) staining

At Day 14 of culture, samples were washed with 1X PBS and incubated in 4% paraformaldehyde (PFA) immediately after removal from experimental conditions. The devices were incubated at 37°C for 15 minutes, then were rinsed with PBS-glycine 2X for 10 minutes at room temperature (RT). The devices were washed again with PBS-Tween-20 ((PBS-Polyoxyethylene (20) sorbitan monolaurate) (0.05% (v/v) Polyoxyethylene (20) sorbitan monolaurate in PBS) for 10 minutes at RT. Then, the cells

were permeabilized with 0.1% Triton-X-100 for 30 minutes at RT, then subsequently blocked with 10% goat serum (in PBS-Tween-20) for one hour at RT. To stain for the fibrotic marker α SMA, the primary antibody (rabbit anti- α smooth muscle actin from Abcam, 1:100) was diluted in 10% goat serum and added to the samples at 4°C overnight. The next day, the samples were washed with PBS-Tween-20 three times for 20 minutes each at RT. Then, the secondary antibody, either anti-rabbit AlexaFluor488 or AlexaFluor594, was diluted in PBS-Tween-20 (1:500) and centrifuged at 14K RPM for 10 minutes, then added to the samples. After 1 hour of incubation at RT, the samples were washed with PBS-Tween-20 five times for 10 minutes each at RT.

To stain for actin cytoskeleton and nuclei, either Alexa Fluor488- or Alexa Fluor647-Phalloidin (1:40) and 4',6-diamidino-1-phenylindole (DAPI) (1:1000) were added to the samples and incubated at 4°C overnight. Samples were then washed with PBS-Tween-20 three times for 20 minutes each at RT. Antifade Mounting Medium was added to the samples (diluted 1:1 in 1X PBS), and the samples were imaged using fluorescence microscopy (Zeiss Axio Observer Z1 with the Zen Pro software suite) equipped with Apotome2 at 10X and 20X objectives. Z-stacked images were captured and reconstructed in FIJI, a version of ImageJ to form representative 3D images. Alternatively, samples were imaged with the Leica SP8 Confocal Microscope at 63X objective, with z-stacked images captured and reconstructed in FIJI to form representative 3D images.

3.3.10 Assessment of 3D tissue alignment within the microfluidic chip

Images of F-actin and DAPI stained tissues formed within the microfluidic chip were analyzed through FIJI. Fast Fourier Transform (FFT) analysis was performed on F-actin images, while DAPI images were used to assess nuclei alignment. For alignment analysis, first, images were rotated based on phase contrast to set alignment axis at 0°. The DAPI-stained image was thresholded, processed through the Watershed plugin, and particles were identified through the Analyze Particles Plugin. The proportion of nuclei was calculated for each angle, grouped in 10° increments, and graphed in histograms.

3.3.11 Live/dead viability assay

After 24 hours of exposure to the different experimental conditions, tissues in the microfluidic devices were assessed for cell viability. Specifically, devices were washed with PBS 1X twice, then incubated with 2 µM of Calcein AM and 4 µM of Ethidium homodimer-III (EthD-III) for 35 minutes at room temperature. The solution was aspirated, and the cells were incubated in fresh RPMI+B27+insulin and imaged with a fluorescent microscope. Tissue viability was calculated based on analysis of acquired images, with number of live (green) cells divided by total cell number (green plus red).

3.3.12 Nuclear viability assay in response to reperfusion

A recently optimized method for the quantification of cell viability within microfluidic 3D tissues (Ong, Zhu, Tan, & Toh, 2020) was utilized for reperfusion experiments. Specifically, nuclear staining was used, with Ethidium homodimer III (EthD-III) to identify dead cells, and DAPI to identify the total cell population. After exposure of tissues to designated oxygen conditions and their subsequent reperfusion

conditions, the devices were washed with 1X PBS, then incubated with 4 μ M EthD-III in RPMI+B27+insulin within a standard tissue incubator for 1 hour. Then, the devices were washed with PBS 1X, then fixed with 4% PFA for 20 minutes. After washing again with 1X PBS, the cells were permeabilized with IF Buffer for 30 minutes at room temperature. The cells were then incubated with 10% goat serum at room temperature for 1 hour, and finally stained with DAPI (1:1000 in PBS-Tween20) for 1 hour. Before imaging with Zeiss fluorescent microscope, the devices were washed twice with 1X PBS. Tissue viability was calculated based on analysis of acquired images, with the equation: $1 - \frac{[(\text{EthD-III}^+ \text{ and DAPI}^+ \text{ cells}) / \text{DAPI}^+ \text{ cells}]}$.

3.3.13 Real-time reverse transcriptase-PCR (qRT-PCR)

In order to extract the cells from the tissues within devices for gene expression analysis, the tissues were first washed with 1X PBS, then incubated with 2 mg/mL collagenase for 30-35 minutes to digest the ECM. The suspension was collected, and the devices were washed 2-3X with 1X PBS to maximize cell collection. The collected cell suspension pooled from multiple devices per condition was centrifuged at 300 x g for 3 minutes, and supernatant was aspirated. Next, Total RNA was extracted with Total RNA Microprep kit (Zymo) per manufacturer's protocol. RNA quality and concentration were assessed with either High Sensitivity RNA tapes and/or Epoch Spectrophotometer System. cDNA was synthesized from Total RNA using iScript Reverse Transcriptase Supermix (QuantBio). iTaq Universal SYBR Green Supermix (BioRad) was used to perform qPCR on synthesized cDNA, with 18S as the housekeeping gene. Primers were validated via melt curve and PCR product verification. For qPCR, 8 μ M dilution of

forward and reverse primers was used for 10 μ L reactions within 96-well plates, with 0.1 μ L per well of cDNA. The qPCR plates were analyzed with qTower 2.0, and the products were verified on 3% agarose gels, imaged with Azure C400.

3.3.14 RNA-seq

RNA was extracted from devices using Miniprep kit (Zymo), as described above, from tissues within microfluidic devices in the physioxia and hypoxia experimental conditions. After analyzing the RNA quality and concentration on High Sensitivity RNA Tape Station, mRNA was extracted and sequenced by Illumina NextSeq2000 at the Genomics Core Facility at ASU. FASTQ files were aligned to the human reference genome (Ensembl GRCh38 release 102) using *STAR* (v2.7.6a). and the reads that mapped to mitochondrial genes were excluded. Raw counts for 60,623 genes were then normalized by CPM and genes having read count <2 were excluded. Ensembl IDs were mapped to remove duplicate genes after arranging for gene counts from high to low, leaving 15,821 genes. Genes were considered differentially expressed for $FDR < 0.05$ and $\log_2(\text{FoldChange}) > 1$ (up-regulated) or $\log_2(\text{FoldChange}) < -1$ (down-regulated) in hypoxia. A total of 475 differentially expressed genes (DEGs) between hypoxia and physioxia samples were identified using *DESeq2* (v1.30.1) with LFC shrink set to normal. Enriched KEGG pathways were identified by performing gene set enrichment analysis by fgsea v1.60.0 on fold changes from DESEQ2 for 15,821 genes. *PathfindR* (v1.6.1) was employed for visualizing gene network and pathways to assess if DEGs in DESeq2 are associated with a pathway.

3.3.15 Statistical analysis

Paired, two-sided t-tests were used for statistical analysis of inter-beat interval variability and BPM for each condition using R. For gene expression data from qPCR, two-way ANOVA was performed on the DCT values using GraphPad Prism. Two-way ANOVA was performed using GraphPad Prism on the tissue alignment and fibrotic marker expression.

3.4 Results

3.4.1 Validation of hypoxia

Prior to proceeding to 3D on-chip tissue experiment, we validated the level of oxygen within the different environments using fluorescent imaging probe, BioTracker 520 Green Hypoxia Dye. Particularly, cells were incubated for 1 hour with the dye, then washed and fresh media added, then incubated for 3 hours in the designated environmental conditions. Appendix Figure B.1 shows the results of BioTracker 520 Green Hypoxia Dye expression for cells seeded on 2D coverslips exposed for a total of 4 hours under the different oxygen conditions. The expression of the BioTracker dye increased as the oxygen level decreased, with the highest expression demonstrated in 1% O₂ (hypoxic) conditions, as imaged at 10X (Appendix Figure B.1A) and 20X magnification (Appendix Figure B.1B). Therefore, each environmental condition accurately exposed the cultured cells to the designated oxygen level, as confirmed through increased expression of BioTracker.

Upon verifying the experimental setup, the 3D co-cultured cardiac tissues were formed within the on-chip microfluidic platform. On Day 14, after being exposed to the

different oxygen levels for 24 hours, the viability of the cardiac tissues was assessed and quantified (Figures 3.2A, C). Among all conditions, the average viability (percent live cells over total cells) was around 88-90%, with no significant differences due to oxygen level (Figure 3.2C), when tissues are immediately processed after exposure to the different oxygen levels. This finding corroborates previous findings in literature that reperfusion (i.e. reoxygenation) or a shift in pH is required for hypoxia-activated apoptosis (Webster et al., 1999).

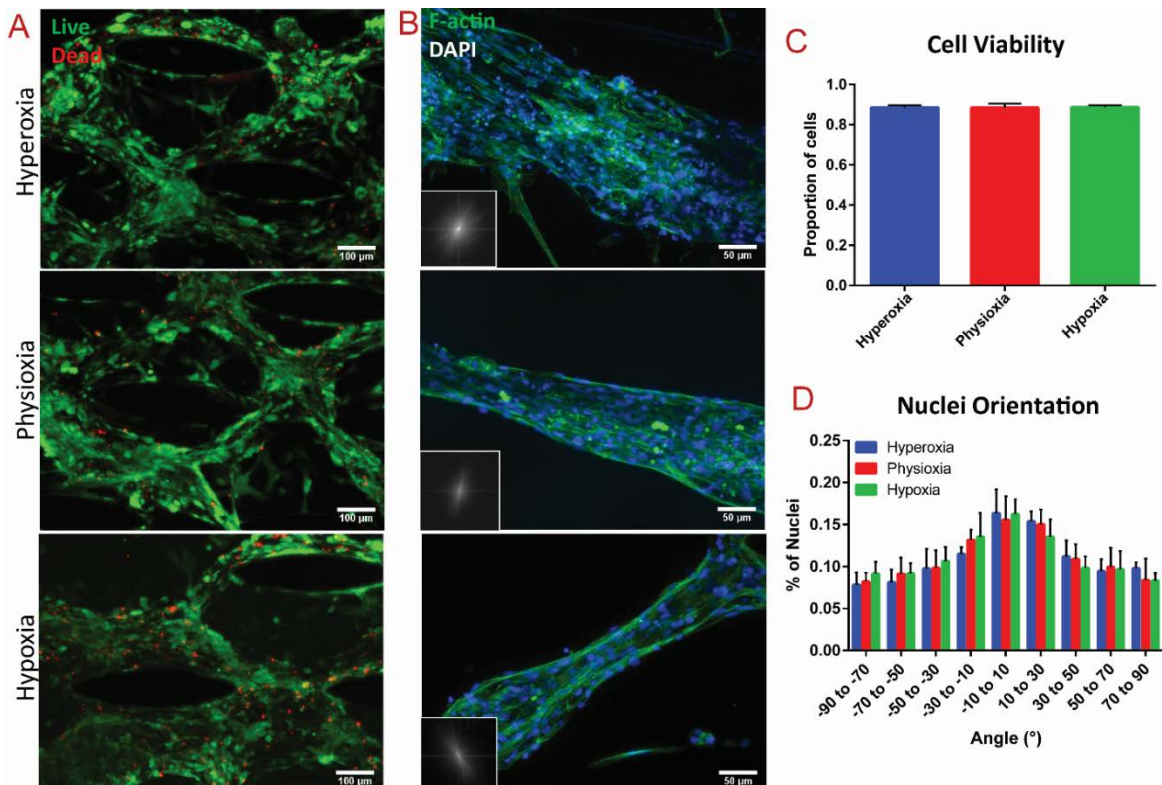


Figure 3.2: Viability and alignment assessment of cardiac tissues after exposure to varying oxygen levels

(A) Viability assay of cardiac tissues after 24 hours of exposure to different oxygen levels, with green=live and red=dead. (B) F-actin staining (green) of cardiac tissues within the vertical spacing between posts within each condition, with FFT analysis in the

lower left corner. Corresponding quantification of (C) cell viability assay and (D) nuclei alignment of the cardiac tissues in each condition, extracted from relative immunostaining.

3.4.2 Analysis of cardiac tissue alignment in response to oxygen conditions

The structural integrity and anisotropy of the cardiac tissues after exposure to the different oxygen levels was analyzed through F-actin imaging and nuclei alignment. The innate microposts within the tissue region of the microfluidic platform (Figure 3.1B) induced high levels of anisotropy, which was pertinent to promote maturation of the encapsulated stem cell-derived CMs (Veldhuizen et al., 2020). To assess whether deprivation of oxygen disrupted the tissue architecture, Fast Fourier Transform (FFT) was performed of the F-actin stained images, while analysis of nuclei alignment was performed based on DAPI staining (Figures 3.2B, D). Highly aligned areas between the vertical spacing of the microposts were analyzed (see Appendix Figure B.2 for tissues between horizontal spacing of posts), revealing no significant changes in tissue alignment in exposure to hypoxia (Figure 3.2D). To that end, our results demonstrated that the extent of hypoxia without presence of reperfusion did not alter the overall alignment of heart on-a-chip tissues.

3.4.3 Fibrotic response of 3D tissues to hypoxia

Ischemia has been shown to cause myofibroblast differentiation of resident CFs in the native myocardium (Porter & Turner, 2009; van den Borne et al., 2010). Cardiac myofibroblasts express contractile proteins, such as alpha-smooth muscle actin (α SMA) and respond to various mechanical and biochemical stimuli, particularly after ischemic

insults in the remodeling heart (Porter & Turner, 2009; Watson et al., 2014). To assess the induction of fibrotic and myofibroblast differentiation of the encapsulated CFs in response to ischemia within the microfluidic heart-on-a-chip platform, IF imaging of both α SMA expression and F-actin filaments was performed on the cardiac tissues after exposure to the various oxygen levels. The corresponding integrated density (area times mean gray value) of α SMA and F-actin filaments was measured within 2-3 images per device. Analysis of α SMA signal intensity revealed significantly increased expression of α SMA within tissues exposed to hypoxia, compared to those in the hyperoxic (i.e., standard tissue culture) condition (Figure 3.3A). To further home in on the fibrotic response of the innate tissue, the integrated density of α SMA was normalized to the integrated density of actin within each image acquisition (Figure 3.3B). When α SMA expression was normalized to abundance of F-actin fibers, there was a significantly increased fibrotic response within tissues in the hypoxic condition, as compared to both the physioxic and hyperoxic conditions (Figure 3.3B).

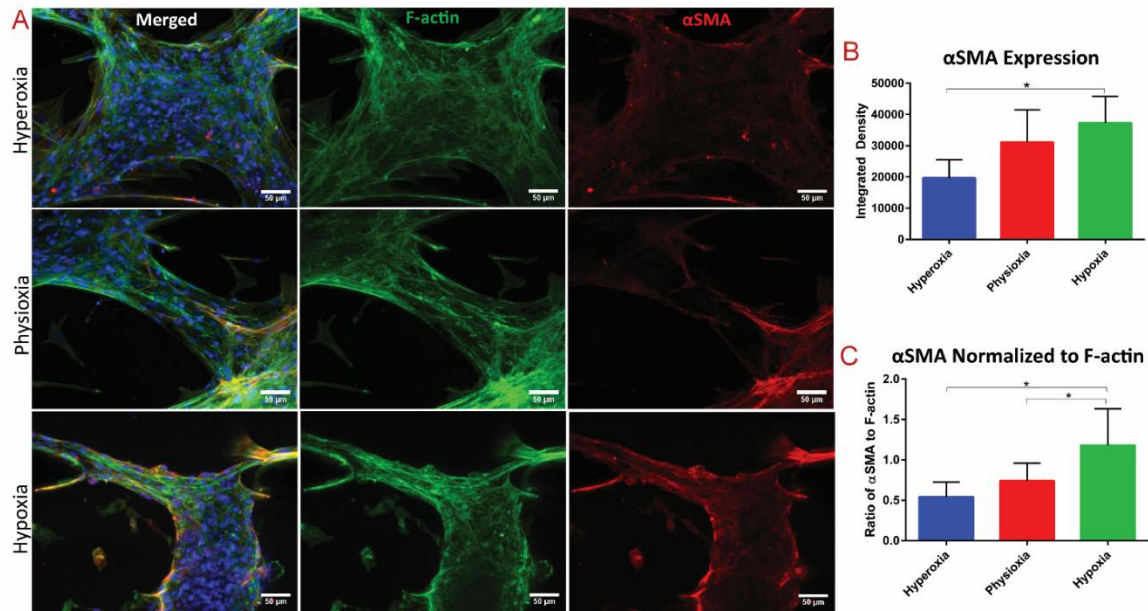


Figure 3.3: Assessment of fibrotic response in 3D tissues exposed to the varying oxygen levels

(A) Immunostaining of cardiac tissue after exposure to the different oxygen levels, with F-actin=green and α SMA=red. Quantification of (B) integrated density of α SMA stain and (C) integrated density of α SMA stain normalized to the integrated density of F-actin fibers.

To tease the role of the 3D environment on ischemic response in cardiac tissues, we investigated the effect of varying oxygen on 2D co-cultured CMs with CF that were seeded on coverslips and cultured for the 13-day experimental period. On the 13th day, the coverslips were exposed to the different levels of oxygen for 24 hours. The cells were fixed, stained for α SMA and F-actin expression (Appendix Figure B.3A), and the respective integrated density was quantified. Interestingly, there was no significant difference in α SMA expression, nor in ratio of α SMA to F-actin (Appendix Figures

B.3B, C). Only the 3D culture of CMs and CFs in collagen: Matrigel hydrogel within the microfluidic platform displayed a significant upregulated expression of α SMA due to hypoxic condition. This is presumably due to the stiff substrate of Matrigel-coated coverslips in the 2D condition (Elson et al., 2019; Li et al., 2020; H. Zhao et al., 2014), and the extended culture in this stiff condition for 13 days, that there was a baseline expression α SMA on Day 13 already. On Day 14, the relatively high level of expression of α SMA in control condition (i.e., hyperoxia) corroborates the elevated α SMA expression over the 3D control on Day 14, thereby masking any additional fibrotic effect from hypoxic conditions. These findings emphasize the necessity for 3D culture to accurately mimic human physiology (Mosqueira et al., 2018; Patino-Guerrero et al., 2020; Veldhuizen et al., 2019). Additionally, the IF findings demonstrate the utility of our heart on-a-chip model for modeling the pathophysiological fibrotic response to hypoxia.

3.4.4 Contractile functionality of 3D tissue in response to varying oxygen levels

Myocardial ischemia can result in irregular contractile patterns (Ross, 1991), i.e. arrhythmias, due to intracellular calcium mishandling and development of tissue fibrosis (Francis Stuart et al., 2016). To assess the effect of hypoxic environment on cardiac tissues' contractile response, real time videos of 30 second duration were recorded of tissue spontaneous contraction immediately after 24 hours of exposure to the different oxygen conditions. The standard deviation of these time intervals was calculated and determined as the measure of inter-beat interval variability. Contraction analysis reveals no difference between spontaneous beat rates in the various oxygen conditions (Figure

3.4B). However, there was a significant increase in inter-beat interval variability between physioxia and hypoxia (Figure 3.4C), demonstrating a decrease in synchronicity after 24 hours of exposure to hypoxic conditions. A similar detrimental effect on contractile function from hypoxia exposure was demonstrated in a recent study using cardiac organoids for MI modeling (Richards et al., 2020), altogether corresponding to the observed clinical manifestation of arrhythmias from myocardial ischemia.

3.4.5 *Transcriptional effect of hypoxia within cardiac tissues*

To further probe the effect of hypoxia on the molecular level within the 3D cardiac tissues formed in the microfluidic chip in response to varying oxygen levels, quantitative polymerase chain reaction (qPCR) was performed on an array of genes that have been implicated in response to hypoxic conditions, as well as genes involved in contractility (Figure 3.4D). Specifically, the differential expression of hypoxia-responsive genes, *ACTA2*, *ANGI*, *BNP*, *POSTN*, *TGFBI* (TGF β 1), and *VEGFA* (Figure 3.4E), and contractile-specific genes, *ATP2A2* and *RYR2* (Figure 3.4F), was assessed. During hypoxia, HIF-1 α is stabilized and binds to hypoxia-response elements of target genes, that lead to upregulation of pathways such as glycolysis (through PDK), angiogenesis (through VEGF), and erythropoiesis (EPO) (Abe et al., 2017; Chi & Karliner, 2004). Angiogenic pathways are induced in response to ischemia due to an upregulated expression of *VEGFA*, which stimulates the remodeling of blood vessels to lead to increased blood flow (Semenza, 2014). Our study demonstrated that gene expression of *VEGFA* was significantly upregulated in the 3D tissues exposed to hypoxia, as a physiological response to induce angiogenesis to counteract the cellular perception of

reduced tissue perfusion. Additionally, expression of *ACTA2*, the gene involved in fibrotic response that encodes for α SMA protein, was significantly upregulated, in comparison of physioxic tissues to hypoxic tissues (Figure 3.4E). This finding confirms the induction of fibrotic response within the hypoxic tissues, as similarly demonstrated from analysis through α SMA immunofluorescent quantification (Figure 3.3). Therefore, exposure of cardiac tissues to hypoxic environments for an extended time triggers the biological cascades for both angiogenesis and fibrosis.

It has also been clinically observed that patients secrete higher amounts of B-type natriuretic peptide (BNP) in their blood during myocardial ischemia, therefore it is commonly used as a diagnostic marker in the clinic (Bassan et al., 2005; Morita et al., 1993), and has been found to be upregulated *in vitro* in human CMs in response to hypoxia (Casals et al., 2009). Therefore, we assayed gene expression levels of *BNP* of hypoxia tissues and found an upregulation in the transcription of *BNP* compared to physioxic and hyperoxic levels, however it does not reach significant levels from n=3 experiments. Similarly, TGF β 1 protein levels have been observed to be upregulated during myocardial ischemia, serving as a transcription factor that initiates transcription to activate a cascade of events, resulting in fibrosis (G. Liu, Ma, Yang, & Zhang, 2017). Therefore, we assayed gene expression levels of *TGFBI* and found no significant difference in expression at the transcription level of *TGFBI*, nor *POSTN*, a direct target of TGF β 1 as a transcription factor (Horiuchi et al., 1999; Landry, Cohen, & Dixon, 2018), between the various oxygen conditions, despite the corresponding IF shows induction of a fibrotic response to the hypoxia. To that end, we speculate that the

observed upregulation of TGF β 1 protein may not be apparent at the transcriptional level; i.e. a mechanism is occurring either post-transcriptionally, or translationally, or post-translationally, which involves upregulation of TGF β 1 protein and induction of fibrotic responses.

Gene expression of *ANGI* (angiotensin I) was also upregulated in the hypoxic conditions, albeit not to statistical significance from n=3 experiments. Angiotensin I is the precursor to Angiotensin II, which is involved in the heart renin-angiotensin system, and has been widely implicated in myocardial infarction (Leenen, Skarda, Yuan, & White, 1999). The upregulation of *ANGI* in hypoxic tissues within our model leads to the hypothesis that *ANGI* was a major regulator of fibrosis in these tissues, as demonstrated through contractile stress fiber formation.

Contractile-specific responses are known to be downregulated in ischemia-reperfusion heart failure (F. S. Ng et al., 2014), therefore we assessed expression of *ATP2A2* (sarco-endoplasmic reticulum Ca²⁺ ATPase) and *RYR2* (ryanodine receptor), genes pertinent in calcium-handling and thus contraction. Both contractile-specific genes exhibit a trend of downregulation corresponding with decreasing oxygen levels (Figure 3.4F), with a significant downregulation of *ATP2A2* in hypoxic conditions, compared to hyperoxia. These findings, within the 3D cardiac tissue-on-chip model, correspond to the clinically observed dysregulation of contractile machinery that occurs in response to ischemia. Additionally, these findings reiterate the discovered disruption in contractile function demonstrated in hypoxic conditions, quantified through inter-beat interval variability, further underlying the adverse role of hypoxia on contractility.

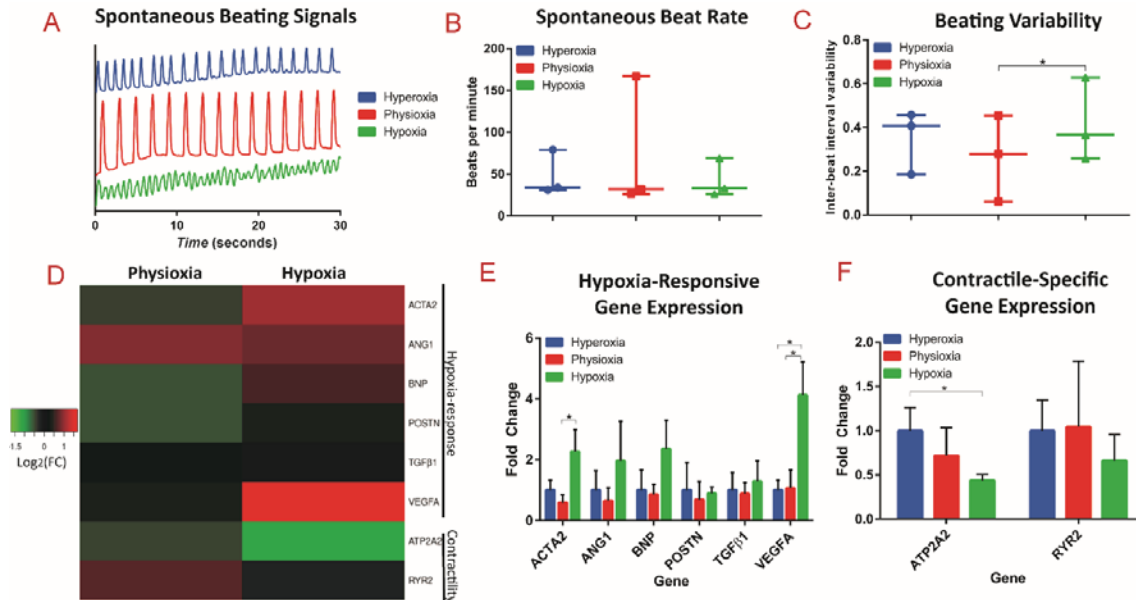


Figure 3.4: Resultant functional and gene expression analysis of 3D cardiac tissues after exposure to different oxygen levels

(A) Representative spontaneous beating signals, (B) average spontaneous beating rate, and (C) inter-beat interval variability from cardiac tissues exposed to hyperoxic, physioxia, and hypoxic conditions. (D) Heatmap of the Log_2 of the expression fold change (compared to hyperoxia) of hypoxia-responsive and contractile-specific genes. Bar graphs of the fold changes of (E) hypoxia-responsive genes and (F) contractile-specific genes are shown, with * as p -value < 0.05 .

3.4.6 Global transcriptomic response to hypoxia

To analyze the transcriptomic profile of co-cultured 3D cardiac tissue within the microfluidic chip in response to hypoxia, whole tissue RNA-seq was performed. As

qPCR analysis revealed no significant differences in expression of the assayed panel of genes for tissues exposed to hyperoxia compared to physioxia, for RNA-seq analysis, we designated the tissues in the physioxia condition as the control and compared the gene expression profiles to those of tissues exposed to hypoxia, each in duplicates. Statistical analysis between the conditions identified a total of 128 differentially expressed genes (DEGs, $|\log_2FC| > 1$ FDR < 0.05), 121 up-regulated and 7 down-regulated, and the Z scores of expression levels were plotted in a heatmap with clustered dendrogram (Figure 3.5A), demonstrating the consistent trend of gene expression regulation amongst the duplicates and between different oxygen conditions. The volcano plot (Figure 3.5B) shows global gene expression profile changes in response to hypoxia for 15,821 genes, further highlighting that hypoxia resulted in more up-regulated genes (121 genes at thresholds of $|\log_2FC| > 1$ and FDR < 0.05 , respectively) than down-regulated genes (7 genes at thresholds of $|\log_2FC| > 1$ and FDR < 0.05 , respectively) with annotation for top ten genes for $|\log_2FC| > 1$. Pathway enrichment analysis was then performed for \log_2FC scores for 15,821 genes on the KEGG (Kyoto Encyclopedia for Genes and Genomes) database to assess if DEGs, in DESeq2. Significant genes with FDR < 0.05 , associated with a pathway, as shown in Figure 3.5C, and the significant enriched pathways with FDR < 0.05 were further investigated. The most significant pathway with the highest positive normalized enrichment score (NES) was glycolysis, demonstrating the switch from oxidative phosphorylation to glycolysis during hypoxia. Additionally, other pathways involved in metabolism were upregulated in the hypoxia condition, including fructose, starch, and galactose metabolism, while oxidative phosphorylation was downregulated, altogether

further highlighting the glycolytic flux that occurs in ischemia. One of the second most upregulated pathways was HIF1 (hypoxia inducible factor 1) signaling, which is activated via hypoxia and implicated in myocardial ischemia (Semenza, 2014). As mentioned, HIF-1 α , the primary transcriptional regulator of HIF1 signaling, is involved in activation of angiogenesis, glycolysis, etc. Additionally, a vast amount of studies on the role of hypoxia in tumor biology (Begg & Tavassoli, 2020; Koshiji et al., 2005; Seo & Kinsella, 2009; To, Sedelnikova, Samons, Bonner, & Huang, 2006) has unveiled that HIF-1 α also transcriptionally downregulates DNA repair pathways, including base excision repair (BER), mismatch repair and homologous recombination. The 3D cardiac tissues demonstrated a similar trend in the downregulation of many DNA repair pathways, including homologous recombination, mismatch repair, and nucleotide excision repair, in the hypoxia condition. Consistently, a number of genes responsible for DNA replication have been demonstrated in literature to be repressed in hypoxic conditions (Hubbi et al., 2013; N. Ng, Purshouse, Foskolou, Olcina, & Hammond, 2018; Prabhakar & Semenza, 2015). Correspondingly, we demonstrated that the RNA-sequencing of physioxic vs. hypoxic exposure of the 3D cardiac tissues reveals downregulation of DNA replication in tissues exposed to hypoxia. To visualize significant genes that are involved in the top 10 enriched pathways, we performed term-gene graph analysis (Figures 3.6A,B). Many genes in the MCM (minichromosome maintenance) family are downregulated and are

shared in the downregulation of both enriched pathways of DNA replication and cell cycle, further highlighting the detrimental effect on cell division from hypoxia.

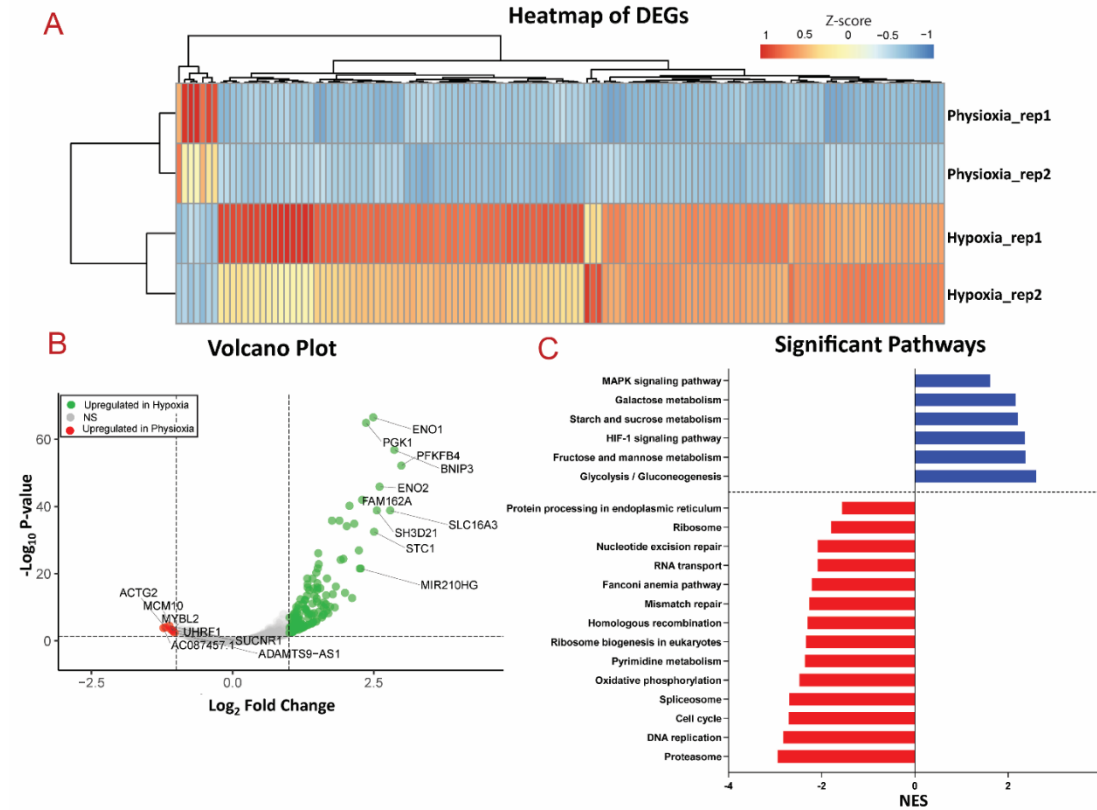


Figure 3.5: Transcriptomic analysis of physioxia and hypoxia tissues

(A) Heatmap of differentially expressed genes (DEGs) between physioxia and hypoxia conditions, with $FDR < 0.05$ of replicates from $n=2$ experiments. (B) Volcano plot of DEGs, where green= up-regulated in hypoxia, grey= not significant, red= up-regulated in physioxia, with annotation for top 10 genes with $|\log_2FC| > 1$. (C) Pathway analysis, showing downregulation (red) and upregulation (blue) of pathways with adjusted p-value < 0.05 .

Furthermore, the most highly downregulated pathway observed in hypoxic tissues compared to physioxic tissues was the proteasome pathway, with a plethora of PSM (proteasome) genes implicated (Figures 3.6A,B). Consistently, it has been previously demonstrated in mesenchymal stem cells that hypoxia causes dissociation and inactivation of 26S proteasome assembly (Abu-El-Rub et al., 2019). Our data suggests that a similar biological response is occurring in human cardiac cells in response to hypoxia, and due to inactivation of the 26S proteasome, there is a transcriptional downregulation of the genes involved in proteasome activity. Therefore, the response of the cardiac tissues to hypoxic conditions, on the transcriptomic level, greatly corresponded with previous findings on cellular response to hypoxia, as well as with clinical observations during myocardial ischemia.

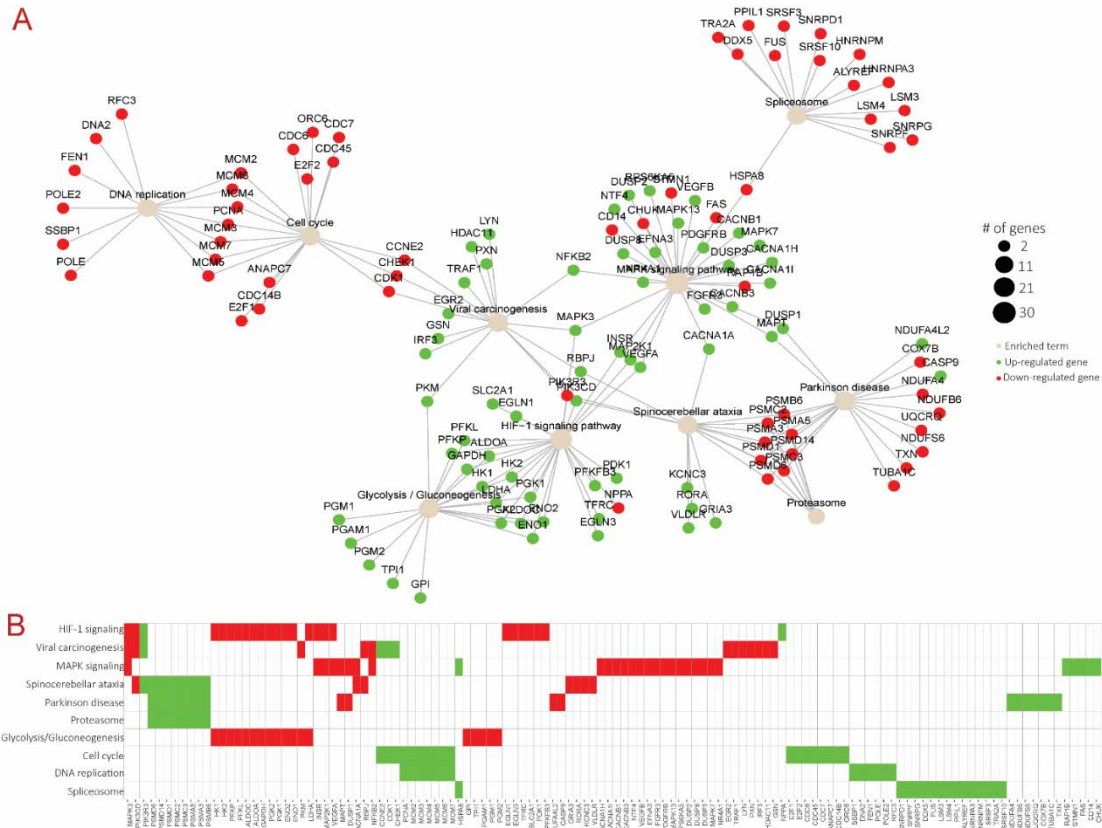


Figure 3.6: Visualization of significant genes among enriched terms from transcriptomic analysis

(A) Term-gene graph of top 10 enriched terms from RNA-sequencing of physioxic compared to hypoxic tissues, with (B) corresponding heatmap with individual genes listed.

3.4.7 Response of cardiac tissues to reperfusion

To further the physiological relevancy of this study, we investigated the effect of reperfusion on the hypoxia-exposed cardiac tissues. Specifically, after exposure of the tissues to the different oxygen conditions, they were either immediately processed (i.e.,

no reperfusion), the media was changed and devices were incubated for 1 hour (i.e., 1 hour reperfusion), or media was changed and devices were incubated for 24 hours (i.e., 24 hour reperfusion). The inter-beat interval variability remained significantly increased in the hypoxic tissues after 24 hours of reperfusion, compared to the physioxic tissues (Figure 3.7A), consistent with earlier findings of beating variability in tissues immediately after being exposed to hypoxia. It has been previously demonstrated that the reperfusion that occurs in IRI incurs a majority of the cytotoxicity observed in the heart because it results in the production of reactive oxygen species (ROS) which is a major cause of apoptosis (Webster et al., 1999). Therefore, we hypothesized that exposure of the hypoxic cardiac tissues to either short- or long-term reperfusion would induce a cytotoxic effect. To better visualize the tissue viability, we utilized a novel method to stain the cells' nuclei (Ong et al., 2020), instead of traditional methods that stain the cytoplasm, to identify dead cells and total cell population. Based on EthD-III and DAPI staining of tissues exposed to the different reperfusion conditions, cell viability was significantly decreased after both 1 hour and 24 hours of reperfusion in the hypoxia-exposed tissues, compared to both physioxic and hyperoxic tissues under reperfusion (Figures 3.7B-E). Therefore, the environmental effects that are introduced from reperfusion and reoxygenation are pertinent in the induction of cytotoxicity, similar to

clinical findings of the myocardial landscape after ischemia reperfusion injury (Frank et al., 2012).

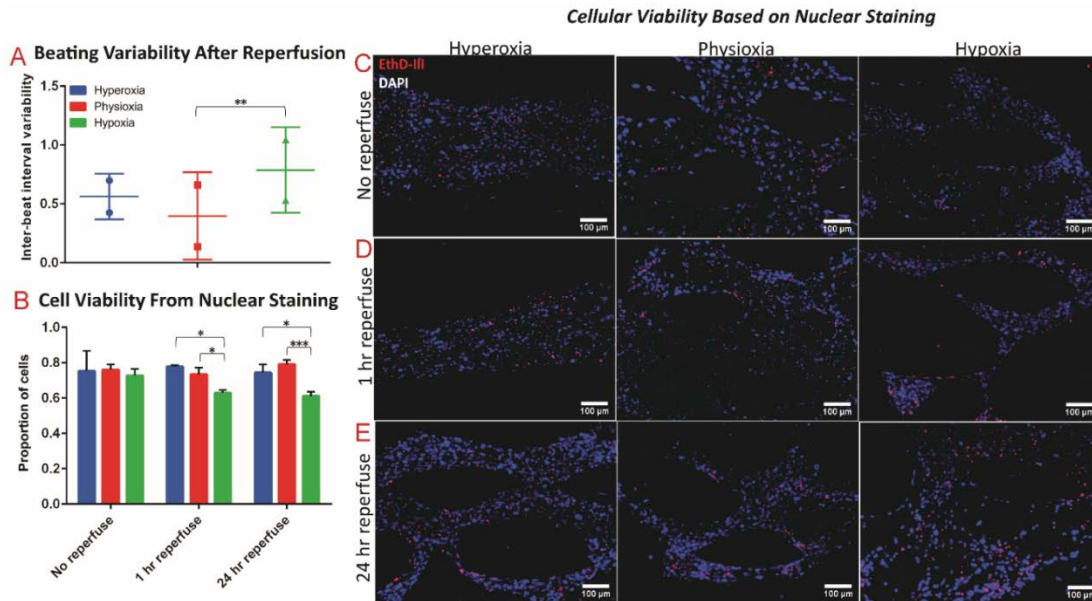


Figure 3.7: Cardiac tissue response to acute and extended reperfusion

(A) Inter-beat interval variability of cardiac tissues after 24 hours of reperfusion. (B-E) Viability quantification, based on nuclear staining, with red as Ethidium Homodimer-III (EthD-III) and blue as DAPI, of cardiac tissues after (C) no reperfusion, (D) 1 hour of reperfusion, and (E) 24 hours of reperfusion.

3.5 Discussion

Ischemic environments within the heart induce a plethora of cellular responses that in turn result in regulation of different pathways instrumental in tissue function and metabolism (Crossman, 2004; Katz, 1973; Nag, 1980). Such changes in the biological landscape of the heart tissue, specifically the myocardium, can prove detrimental and result in tachyarrhythmia, heart failure, and even death (Ghuran & Camm, 2001; Nag,

1980). To better understand the mechanisms behind hypoxia governing an ischemic injury, multiple studies exist that involve exposure of cardiac cells to hypoxic environments, including those in 2D micromodeled environments involving animal-derived cardiomyocytes (H. Liu et al., 2020; L. Ren et al., 2013) or hPSC-CMs (Oleaga et al., 2019), as well as in 3D environments involving hPSC-CMs (Acun, Nguyen, & Zorlutuna, 2019; Chen & Vunjak-Novakovic, 2019; Richards et al., 2020). Each study presents with particular novelties and advantages, including the incorporation of electrodes to study the cardiac electrophysiology real time (H. Liu et al., 2020; Oleaga et al., 2019), the utilization of a gradient to mimic *in situ* dynamics (L. Ren et al., 2013; Richards et al., 2020), and an investigation into the role of cardiac maturation or age in disease modeling (Acun et al., 2019; Chen & Vunjak-Novakovic, 2019). Here, we present the first 3D heart on-a-chip microfluidic model that we know of that incorporates a true physioxic condition for the study of myocardial ischemia with hiPSC-CMs, presenting with improvements in biological complexity and maturation over 2D models. Importantly, our studies also revealed the importance of 3D versus 2D culture, a concept that has been extensively observed in literature (Mosqueira et al., 2018; Patino-Guerrero et al., 2020; Veldhuizen et al., 2019). We demonstrated that exposure of 2D cultured CM:CFs to hypoxia resulted in no effect on α SMA expression, while there was significant upregulation of α SMA in 3D cardiac on-a-chip tissues in response to hypoxia. This finding also highlighted the potential of our developed heart on-a-chip platform in cardiac disease modeling applications, as the hypoxic tissues responded with the expected induction of fibrosis.

We also identified contractile irregularities due to exposure to hypoxia, as well as the downregulation of genes pertinent in tissue contraction. A recent study investigated the effect of hypoxia on human cardiac organoids to model myocardial infarction, induced through chronic exposure (i.e., 10 days) to 10% O₂ and norepinephrine to model the effect of partially blocked arteries for extended time on the myocardium (Richards et al., 2020). Through utilization of organoids, a gradient of oxygen was established due to diffusion limitations, so that the organoids' circumference experienced 10% O₂ while the core was near anoxic. The authors also revealed a significant downregulation of major calcium handling genes within the hypoxia-exposed organoids, corroborating our finding of contractile dysregulation in cardiac on-a-chip tissue model.

Further qPCR analysis in our study revealed the upregulation of known hypoxia-responsive genes, with significant changes in *ACTA2* and *VEGFA*. However, we did not reveal a significant change in the gene expression of *TGFBI* or *POSTN*, markers of TGFβ1 signaling. We speculate that either differential regulation of TGFβ1 may be occurring post-transcriptionally, or other types of cells in the *in vivo* environment greatly contribute to induction of TGFβ1 signaling. Although it has been found that most cells in the myocardium secrete TGFβ1, macrophages that infiltrate in response to myocardial injury release both TGFβ1 and ANGII in significant quantities (G. Liu et al., 2017; Shinde & Frangogiannis, 2014). Therefore, incorporation of macrophages to the platform, ideally introduced through media flow to model their infiltration via the bloodstream, will be the subject of future studies to better recapitulate the myocardial environment after ischemic injury.

To further analyze the clinical importance and biomimicry of this model system for disease modeling application, we performed molecular-level analyses through RNA-sequencing to unveil unbiased transcriptomic profiles of physioxic and hypoxic cardiac on-a-chip tissue. A myriad of pathways was revealed to be tightly regulated in a similar fashion as observed in literature in response to hypoxia and clinically in response to myocardial ischemia. Importantly, we investigated transcriptional alterations in the comparison of physioxic (5% O₂) to hypoxic (1% O₂) tissues. Particularly, our results demonstrate that the lack of oxygen in 1% O₂ conditions led to the downregulation of oxidative phosphorylation and thus to upregulation of glycolysis and other anaerobic metabolic pathways to fulfill ATP deficits. Additionally, the hypoxic environment resulted in the downregulation of many regulatory pathways in the cells, including DNA machinery and protein regulation. Therefore, transcriptomic analysis between physioxic and hypoxic tissues revealed a pattern in regulation of a multitude of pathways that is both parallel to observations in other cell types in literature, and also observed as clinical responses to myocardial ischemia. The use of 5% O₂ for physioxic conditions is a novelty in our study, compared to the previous studies mentioned for *in vitro* modeling of myocardial ischemia.

Our investigations into tissue integrity revealed no effect on viability nor alignment in hypoxic tissues without reperfusion, demonstrating that exposure to hypoxia does not induce necrosis or apoptosis to a significant effect. However, once the tissues are exposed to media reperfusion and tissue reoxygenation, for both short- and long-term durations (1 hour vs 24 hours), the tissues that were exposed to hypoxia exhibited

significantly decreased cell viability in comparison to hyperoxic and physioxic tissues, similar to previous observations during IRI (Webster et al., 1999). To attempt to reduce the tissue damage from IRI, ischemic pre-conditioning has been a subject of prior studies (Yadid et al., 2020). Therefore, our planned studies could further focus on the role of ischemia pre-conditioning on development of injury after reperfusion. Importantly, the microfluidic nature of the model could be leveraged in its capability for constant media flow. To advance the complexity of the model, we plan to incorporate fluid flow in the next generation to simulate blood flow through the tissue. Particularly, fluid flow would be incorporated throughout the culture of maturation of tissues (i.e., 13 days). During ischemia, the flow would be halted to allow for buildup of metabolic waste due to lack of washout, then the media flow would be reintroduced to measure reperfusion injury. Another advantage of the use of a microfluidic model is in its ability to induce a gradient of hypoxia and nutrient diffusion across the channel, to better model the differential gradient that is experienced in the various layers of the heart (i.e., epicardium, myocardium, and endocardium).

In summary, we demonstrate the development of a myocardial ischemia model using an anisotropic 3D cardiac on-a-chip platform. Additionally, the design of the platform derives great potential for future studies to enhance the clinical relevance and complexity of the described microfluidic model of myocardial ischemia on-a-chip.

3.6 Conclusion

In this work, we developed an experimentally simple model of myocardial ischemia through the exposure of 3D co-cultured cardiac tissues within optimized

microfluidic devices to varying levels of oxygen for 24 hours. In response to hypoxia, we demonstrated the induction of fibrosis through upregulation of α SMA expression within the cardiac on-a-chip tissues, which was not apparent in 2D cultured cardiac cells. Additionally, we demonstrated the detrimental effect of hypoxia on synchronous contraction, particularly in comparison of physioxic to hypoxic tissues, through quantification of inter-beat interval variability. However, neither the anisotropic nature of the cardiac tissues nor their viability was affected through exposure to hypoxic environments, suggesting the clinical role of reperfusion in ischemic injury in the induction of cytotoxicity. We further performed transcriptional analysis through qPCR to verify the biological response of hypoxic tissues, and additionally investigated the transcriptomic profiles through RNA-sequencing of hypoxic and physioxic tissues. Particularly, we identified the upregulation of glycolysis and corresponding downregulation of oxidative phosphorylation in tissues exposed to 1% O₂ compared to those exposed to 5% O₂. We also identified the downregulation of multiple regulatory pathways in response to hypoxia, including those involved in DNA replication, DNA repair, and proteasomal activity. In conclusion, the described ischemic heart on-a-chip model serves as a fundamental step for the study of ischemic cardiac tissues that result in direct response to hypoxia.

CHAPTER 4

AIM 3: Create an hiPSC line with a *KCNH2* mutation, using CRISPR/Cas9 gene-editing, and model Long QT Syndrome Type 2 on-a-chip within developed microfluidic platform

4.1 Abstract

Long QT syndrome (LQTS) is a highly prevalent CVD characterized by QT interval prolongation that can lead to sudden cardiac death due to heightened susceptibility to tachyarrhythmias. A plethora of mutations have been identified in *KCNH2*, the gene that encodes for hERG, which lead to pathological onset of LQTS type 2. Study into the different mutations in hERG has revealed extensive heterogeneity in regards to the mechanism of the mutation, adding to the complexity of the disease. Here, in this chapter, we have developed, for the first time, LQTS2 diseased tissue on-a-chip model. Specifically, we have primarily demonstrated creation of an hiPSC line with R531W mutation in *KCNH2*, implicated in the onset of LQTS2, using a novel CRISPR/Cas9 gene-editing technique termed Big-TREE. We described successful differentiation and characterization of isogenic cardiomyocytes (CMs) and cardiac fibroblasts (CFs) from WT and *KCNH2*-edited hiPSCs. A deficiency in hERG trafficking was identified in hiPSC-CMs with the *KCNH2* mutation, revealing a possible mechanism of R531W mutation in LQTS2 pathophysiology. Furthermore, we described for the first time creation of a three-dimensional (3D) LQTS2 tissue on-a-chip, using our heart-on-chip microfluidic technology, 3D hydrogel biomaterials and co-culture of edited isogenic hiPSC-CMs and hiPSC-CFs. We have extensively characterized the properties of the

mature LQTS2 tissue on-a-chip, through analysis of tissue structure, contractile function, calcium handling, and β -agonist response. Further, phenotypic rescue was attempted via pharmacological intervention, including multiple pharmaceuticals with differing mechanism of action, of LQTS2 on-a-chip tissues.

4.2 Introduction

Heart disease remains the leading cause of mortality, despite great efforts in cardiovascular research (Heidenreich et al., 2011). Among all heart disease, long QT syndrome (LQTS) is one of the most prevalent, affecting 1:2000 of healthy births (Schwartz, Ackerman, George, & Wilde, 2013). LQTS is characterized by prolongation of the QTc interval, that can lead to tachyarrhythmias, typically triggered by stress, and unfortunately lead to sudden cardiac death. Many variants of LQTS exist and are classified by the gene implicated for disease onset, with Type 2 (involving mutations in *KCNH2*) encompassing a 25-30% of LQTS cases (Alders, Bikker, & Christiaans, 2003). *KCNH2* encodes for hERG, the pore-forming subunit of the potassium channel that produces the rapid component of the delayed rectifier repolarizing current (I_{Kr}). hERG is a tetrameric channel, composed of 6 transmembrane segments, S1-S6, and an NH₂-terminal and COOH-terminal in the cytoplasm (Vandenberg et al., 2012) (Figure 4.1A). The voltage sensor domain (VSD) of the channel is from S1-S4, with S4 containing six positively charged amino acids (AA) and S1-S3 containing negatively charged amino acids that act as counter-charges (Shi, Thouta, & Claydon, 2020), while segments S5-S6 form the pore domain. The S4 region of hERG includes regularly spaced, charged AA that function together as the voltage sensor that responds to changes in membrane

potential (Witchel & Hancox, 2000). Among these important amino acids within the VSD, R531 has been demonstrated as the most critical voltage sensor residue for gating of hERG (Piper, Hinz, Tallurri, Sanguinetti, & Tristani-Firouzi, 2005). Many single-base mutations in hERG have been documented that lead to LQTS2 (Kapplinger et al., 2009) with a majority resulting in missense mutations, and are found in locations spread throughout hERG (C. L. Anderson et al., 2014). The complexity of LQTS2 disease is further exacerbated by the tetrameric nature of the channel, as heterozygous mutations can result in haploinsufficiency, negatively affecting co-assembly of the protein (Gong, Anderson, January, & Zhou, 2004). Overall, it has been found that pathological mutations in *KCNH2* generally lead to a reduction in I_{Kr} , however, the mechanism by which the mutation affects the hERG channel varies. Four phenotypic classes of mutations exist that affect I_{Kr} and lead to LQTS2, which include loss of function, gain of function, non-functional but trafficking-competent, and trafficking-deficient hERG channels (Ficker et al., 2000; Thomas, Kiehn, Katus, & Karle, 2003), or alternatively from a combination of these mechanisms (Delisle, Anson, Rajamani, & January, 2004; Paulussen et al., 2002). Altogether, the varying mechanism of mutation in pathophysiology renders pharmacological treatment of LQTS2 extremely complex and highly dependent on a particular mutation. Thus, understanding the mechanism of mutation in LQTS2 is pertinent in efficient disease treatment. Much of the culminating research in LQTS2 in the past has involved studying *KCNH2* mutations in heterologous expression systems. However, such systems lack the characteristics, both biologically and physiologically, of cardiomyocyte (CMs) (Chandra, Starmer, & Grant, 1998; Derangeon, Montnach, Baro, &

F., 2012; Friedrichs, Malan, & Sasse, 2013). The advent of deriving human induced pluripotent stem cells (hiPSCs) from patient cells has resulted in a major thrust in recent *in vitro* research to elucidate the mechanisms of particular mutations implicated using cells from patients with LQTS2 within 2D culture assays (Bellin et al., 2013; Duncan et al., 2017; Garg et al., 2018; Itzhaki et al., 2011; Kuusela et al., 2016; Lahti et al., 2012; Matsa et al., 2011; Mesquita et al., 2019; Mura et al., 2017; Yoshinaga et al., 2019). These approaches have provided significant advances in the understanding of the specific mechanisms of how different mutations result in LQTS2 pathology.

However, an inherent obstacle in the use of patient-specific cells is the innate genetic heterogeneities or unknown mutations amongst patients that may obscure dissection of the specific role of *KCNH2* in onset of LQTS2. The development of CRISPR/Cas9 gene-editing strategies renders the ability to robustly induce specific gene edits in hiPSCs allowing for the mechanistic study of the direct effect of base-level changes on cell function. Type II CRISPR (clustered regularly interspaced short palindromic repeats)/Cas (CRISPR-associated protein) is a system discovered in prokaryotes, that provides immunity against foreign viruses through incorporation of genetic material from these pathogens (Horvath & Barrangou, 2010). There is a wide family of Cas enzymes with varying functions, however Cas9 specifically has received much attention, due to its ability, guided by complementarity of guide RNA sequences, to cut double-stranded DNA at specific places in the genome. Thus, vast amounts of research have been performed recently to create precise gene-edits in various cell types

and sources, using CRISPR/Cas9, and related modified versions (Cong et al., 2013). The Cas9 system relies on the following components: the Cas9 enzyme, non-coding CRISPR RNA (crRNA), and a trans-activating crRNA (tracrRNA). The crRNA serves as the targeting RNA sequence, which will complementarily bind to the DNA sequence of the target gene. The tracrRNA serves as the RNA sequence for loading of Cas9. The Cas9 enzyme will then bind to the protospacer adjacent motif (PAM) and cut the DNA 3 bp upstream. After a double-stranded break (DSB), either non-homologous DNA end joining (NHEJ) or homology-directed repair (HDR) can occur. In order to facilitate specific gene-edits, the naturally occurring nucleotide repair system, HDR, can be used if a sequence that is homologous to the specific site of edit in the DNA is supplied with delivery of the Cas9.

The Cas9 enzyme has been modified to optimize its capability in gene editing. Specifically, the Cas9 nickase (Cas9n) was created through modification of the RuvC1 domain in the *S. pyogenes* Cas9 (spCas9) nuclease sequence, creating an amino acid substitution from an aspartate to alanine (D10A) (Cong et al., 2013). The Cas9n simply “nicks” one strand of DNA; while the nuclease creates DSBs. Cas9n requires binding to each strand of the complementary DNA in order to induce a DSB, thus significantly reducing chances of off-target mutagenesis (Ran et al., 2013). However, the success of the nickase in targeted editing hinges on efficient homology directed repair, which results in low editing efficiencies. To overcome this limitation, base editors have been fused to Cas9n that serve to introduce the desired base edit, negating the need for HDR (Anzalone, Koblan, & Liu, 2020; Eid, Alshareef, & Mahfouz, 2018; Rees & Liu, 2018;

B. Yang, Yang, & Chen, 2019; G. Yang & Huang, 2019). However, efficient selection of the cells that have incorporated the Cas9 machinery and active base editing is pertinent, and made particularly more difficult if the editing efficiency specific for the target site is low. Historically, methods involving introduction of antibiotic-resistance and/or fluorescent reporter cassettes have been described that are either permanently or temporarily introduced into the cell (Ann Ran et al., 2013; C. Ren et al., 2015). A novel approach, termed Big-TREE (Brookhouser et al., 2019; Standage-Beier et al., 2019; Tekel, Brookhouser, Standage-Beier, Wang, & Brafman, 2021), has recently been developed that involves delivery of an episomal reporter with the Cas9 system that serves as a marker for cells with active editing. Briefly, the system involves delivery of a BFP plasmid along with nickase Cas9^{D10A} fused to a cytidine deaminase. Once inside the cell, the editor will change the existing genomic C's to T's within the editing window, as well as the C's on the BFP plasmid (as guided by the sg(BFP->GFP) sequence), resulting in expression of a GFP plasmid. The BFP to GFP conversion can be used as a marker for active editing, rendering this technique particularly useful in sorting for cells to create isogenic clones.

Using CRISPR/Cas9 or other gene-editing/delivery techniques, different mutations of *KCNH2* have been studied in human stem cells (Bellin et al., 2013; Brandao et al., 2020; Mehta et al., 2014; Mesquita et al., 2019; Y. Wang et al., 2014). However, many of these studies relied on 2D culture, which limits the ability to elucidate cell-ECM and tissue-level interactions, which are pertinent to better understanding of the clinical pathophysiology of LQTS2. To address limitations of 2D platforms, organ-on-chip

technologies have been developed that enable formation of 3D, biomimetic human tissue environments within precisely engineered microfluidic platforms. To that end, we have recently described an anisotropic 3D human stem cell-derived heart on-a-chip platform, validated with three distinct cardiac cell types namely, rat, human embryonic stem cell (hESC)-derived, and hiPSC-derived. Notably, the cardiac tissue was comprised of co-culture of these cells with interstitial, isogenic cardiac fibroblasts (CFs) within a 3D biomimetic hydrogel to better mimic the physiology of the native myocardium. In-depth characterization of our heart-on-a-chip platform revealed an enhanced maturation of the 3D tissue state, through gene expression, cellular-level and tissue-level structure, calcium handling, and drug responsiveness studies (Veldhuizen et al., 2020). Our demonstrated heart on-a-chip platform has great promise in the modelling of cardiac-specific diseases, due to its physiologically relevant structure and function.

Despite the significant advances of previous research, LQTS remains widely prevalent, with the mechanism of many mutations left unknown, and thus therapeutic strategies are not well targeted. Of identified mutations in LQTS2, to our knowledge, there does not yet exist a study that involves the use of gene-edited human stem cells to investigate the mutation in the important R531 residue and corresponding pathophysiology. Furthermore, there lacks a complex, 3D *in vitro* biomimetic model of myocardial tissue that incorporates KCNH2^{R531W} edited stem cell-derived cardiac cells to truly mimic LQTS2 in a native-like 3D tissue environment.

In this chapter, we describe the development, for the first time, of a 3D human cardiac on-chip tissue microfluidic model of LQTS2. Particularly, our approach involves:

1) creation of isogenic human induced pluripotent stem cell lines with R531W mutation in *KCNH2* induced via Big-TREE gene-editing; 2) differentiation and subsequent extensive characterization of CMs and CFs from the gene-edited hiPSCs; and 3) modeling LQTS2 heart tissue in our 3D on-chip microfluidic device, recently validated for the creation of mature cardiac tissue, with *KCNH2*-edited iPSC-CMs and iPSC-CFs for the mechanistic studies of the role of R531W in LQTS2 pathology.

To study the emanation of pathological characteristics that resemble LQTS2 from introduction of a mutation in *KCNH2* into hiPSC-CMs and hiPSC-CFs, phenotypes of resultant cardiac tissues within a 3D model were analyzed. Specifically, to study the role of *KCNH2* in emanation of these phenotypes, the contractile properties of the engineered cardiac tissue composed of *KCNH2*-mutated hiPSC-CMs, both in the presence and absence of “stress”, in the form of catecholamines, were observed. The resultant beating frequency and inter-beat interval variability were recorded to assess arrhythmogenicity. Similarly, calcium transients were measured, to assess the different calcium handling characteristics of tissues with R531W in *KCNH2* and the mechanism of the mutation in arrhythmogenicity in response to catecholamines.

4.3 Materials and Methods

4.3.1 Plasmid Construction

The sgRNAs were synthesized as oligonucleotides and 5' phosphates were added by incubating 1 µg oligo nucleotide in 1X T4 DNA Ligase Buffer (New England Biolabs) and 10 units of T4 Polynucleotide Kinase (New England Biolabs), incubating at 37°C overnight. The oligonucleotides were duplexed via heating the reactions to 90°C within

aluminum blocks for 5 minutes, then the blocks and the reaction were allowed to gradually reach room temperature. Then, the sgRNA backbone was digested, using BbsI-HF in cutsmart buffer at 37°C for 1.5 hr, then purified with PCR cleanup kit (Qiagen), creating a 40 ng/μL solution of purified, digested sgRNA vector. The vector was then dephosphorylated, using 1 unit of rSAP in cutsmart buffer, at 37°C overnight, then purifying with PCR cleanup kit (Qiagen), creating a purified, dephosphorylated plasmid DNA solution at 20-40 ng/μL. This prepared plasmid sgRNA vector was ligated with the oligonucleotide duplex, using T4 DNA ligase, through incubation at room temperature for an hour. Alongside, a no insert ligation and vector only controls were created.

The ligated plasmid sgRNA vector was then transformed via mixing 5 μL of the mixture with 50 μL of competent cells on ice. After 30 minutes incubation on ice, the mixture was heatshocked at 42°C for 30 seconds, then transferred back to ice for 5 minutes. LB media, without antibiotic, was added and the samples were grown in a 37°C incubator, shaking at 220 RPM, for 1 hour. The outgrowth solution was plated on LB agar/ampicillin plates overnight at 37°C. Multiple colonies were picked the following morning and grown in 4 mL of LB with ampicillin in the shaking incubator overnight. The plasmid DNA was extracted using a Miniprep kit, then sequenced, via Sanger Sequencing at Genewiz, to ensure intact U6 promoters, sgRNA sequence, etc. After sequence confirmation, the plasmid DNA was retransformed in the competent cells via incubation of 200 μL of the starter culture in 200 mL of LB with ampicillin overnight. The plasmid DNA was then extracted using a Maxiprep kit, then concentrated using

alcohol precipitation with sodium acetate and an ultracentrifuge at 18,000 RPM for 33 minutes at 4°C. The sequence was once again verified through Sanger Sequencing.

4.3.2 HEK transfection

HEK293 cells were seeded in 24-well plates at 185K cells per well. The next day, the cells were transfected via addition of 500 ng total of DNA per well (300 ng of Cas9 plasmid, 100 ng of sgRNA plasmid, and 100 ng of BFP plasmid), 1 µL of P3000, 0.75 µL Lipofectamine 3000 and 50 µL of Opti-MEM. After 24 hours, the media was changed. Transfected HEK293 cells were imaged for BFP and GFP expression and subjected to flow cytometry 48 hours post transfection.

4.3.3 hiPSC Transfection

hiPSCs (IMR90-4; WiCell (Yu et al., 2007)) were maintained in mTeSR and passaged with 0.5 mM EDTA at least three times after thawing before transfection. To prepare cells for transfection, the hiPSCs were seeded in Matrigel-coated 12-well plates and maintained in mTeSR1 until 70-80% confluent. The transfection mastermix (MM) consisted of 100 µL OptiMEM, 4 µL LipoStem, 300 ng of BFP plasmid, 300 ng of guide plasmid, and 900 ng of base editor plasmid per well. After media change, the MM was added dropwise to each well. The media was changed the next day, and the hiPSCs were subjected to flow cytometry 48 hours post transfection.

4.3.4 Fluorescence-activated cell sorting (FACS)

Approximately 48 hours post transfection, HEK cells or hiPSCs were bulk sorted via BD FACSAria Ilu-Cell Sorter, with help from the ASU Genomics Core, into double

negative (DN), unsorted (US), BFP⁺, and BFP⁺/GFP⁺ populations. Specifically, 1000 cells were sorted directly into prepared Phire MM, consisting of 25 μ L of Phire, 5 μ L of F+R primers at 10 μ M, and 15 μ L of NF H₂O. Immediately after sorting, PCR was performed using the on-target primers listed in Supplemental Table 1, and products were then verified on 1% agarose gels. The products were subject to column purification using the QIAquick PCR purification kit (Qiagen) before sending to Genewiz for sequencing to determine editing efficiencies.

4.3.5 hiPSC base editing and clonal isolation

To determine editing efficiency, the cells sorted into PHIRE MM (n of 4 each for DN, BFP⁺, BFP⁺/GFP⁺, and US) were subject to PCR using primers flanking the edit on KCNH2 (Supplemental Table 1), then sequenced via Genewiz. The editing efficiencies were determined using MoriarityLab-EditR program. Single-cell sorting was also performed on BD FACSAria Ilu-Cell Sorter to create hiPSC clones. Specifically, BFP⁺/GFP⁺ cells were sorted as single cells into 96-well plates into a solution of CloneR (Stem Cell Technologies) and mTeSR1. The media was changed the next day with mTeSR1, then the media was changed every other day until visible colonies were observed. Viable colonies, once ~50% confluent, were passaged with accutase into one well of a 24-well plate. The cells were further expanded until culture within a 6-well plate, then the clones were subject to genotyping analysis.

4.3.6 Sequence analysis at on- and off- targets

To perform genotyping, gDNA was extracted from frozen cell pellets using the DNeasy Blood & Tissue Kit (Qiagen). PCR was performed on the gDNA using Phusion[®] High Fidelity DNA polymerase (New England Biolabs) for both on-target and off-target loci. PCR products were column purified using the QIAquick PCR purification kit (Qiagen), then sent for sequencing to Genewiz. To determine possible off-target loci, CCTop was used with input parameters set for *S. pyogenes* Cas9 against human genome reference sequence hg38 (Stemmer, Thumberger, del Sol Keyer, Wittbrodt, & Mateo, 2015), and the top 4 loci were sequenced. Similar to described above, EditR was used to quantify on- and off-target editing.

4.3.7 Karyotype analysis

To analyze the karyotype of the cell lines, cytogenetic analysis was performed (via Cell Line Genetics) using standard protocols for G-banding on 20 metaphase cells.

4.3.8 Trilineage differentiation of edited hiPSCs

Trilineage differentiation was performed on hiPSCs as embryoid bodies (EBs) to ensure maintenance of pluripotency through editing process. To form the EBs, hiPSCs were seeded at 1.5-2M cells per well of 6-well low adhesion plate and placed on orbital shaker at 100 RPM within 37C incubator. The hiPSCs were grown for 2 days on the orbital shaker, with changing mTeSR1 media each day. On Day 2, media was changed to differentiation media (DMEM/F12, 20% FBS, 1% pen/strep) and the cells were maintained on the orbital shaker for 4 more days. On Day 6, the EBs were plated on

Matrigel-coated wells, and grown for 20 more days, with media changes using the differentiation media every 1-2 days. The plated EBs were fixed on D26 and subject to IF for trilineage markers to assess pluripotency potential.

4.3.9 CM differentiation of hiPSCs

hiPSCs were differentiated into CMs using our previously described method (Veldhuizen et al., 2020). Briefly, hiPSCs were grown in mTeSR1 until 75-85% confluent, then CM differentiation was initiated via Wnt inhibition with 7-10 μ M CHIR99021 in RPMI + B27 – insulin. Wnt activation was initiated on Day 3, with supplementation of 5 μ M IWP2 in RPMI + B27 – insulin. Cardiac maturation was supported from Day 7-13 with RPMI + B27 + insulin. On Days 13 and 16, the wells were washed with PBS 1X and the cardiomyocytes were purified with RPMI no glucose + B27 + insulin, supplemented with 4 mM sodium lactate. After recovery on Day 19 with RPMI + B27 + insulin, the purified CMs were replated on Matrigel-coated plates to remove dead cells and debris. The CMs were used for all characterizations from Day 25 onward.

4.3.10 CF differentiation of hiPSCs

hiPSCs were differentiated into CFs based on a recently developed protocol from Zhang et al (J. Zhang et al., 2019). Briefly, hiPSCs were cultured in mTeSR until 75-85% confluence, then differentiation was initiated via Wnt inhibition with 7-10 μ M CHIR99021 in RPMI + B27 – insulin. On Day 1 of differentiation, media was changed to RPMI + B27 – insulin. On Day 2 of differentiation, media was changed to CFBM (cardiac fibroblast basal medium), supplemented with 75 ng/ μ L of bFGF. CFBM was

exchanged every other day until Day 20, when the hiPSC-CFs were passaged, considered as passage 0, with 0.05% Trypsin-EDTA. From P0 onward, the hiPSC-CFs were cultured in FGM3, routinely passaged with 0.05% Trypsin-EDTA, and cryopreserved in 70% FGM3, 20% FBS, and 10% DMSO. hiPSC-CFs were analyzed via qPCR to verify lack of expression of pluripotent markers and cardiomyocyte markers, and upregulation of fibroblast-specific markers. hiPSC-CFs were also stained for vimentin and TE7.

4.3.11 3D cardiac tissue formation within the microfluidic heart-on-a-chip platform

The heart on-a-chip microfluidic devices were fabricated as previously described (Veldhuizen et al., 2020; Veldhuizen & Nikkhah, 2021). Isogenic co-cultured cardiac tissues were formed at a 4:1 ratio of hiPSC-CMs:hiPSC-CFs, and encapsulated within a collagen (2mg/mL):20% Matrigel hydrogel, as previously described (Veldhuizen et al., 2020; Veldhuizen & Nikkhah, 2021). The tissues were cultured within the microfluidic devices for a total duration of 14 days.

4.3.12 Pharmaceutical treatment and assessment of WT and LQTS tissues on-a-chip

After formation of mature cardiac tissues within the microfluidic chip, the functionality of both WT and LQTS2 tissues was studied. Further, pharmacological rescue was attempted with ALLN, thapsigargin, and nicorandil and the resultant contractile function and calcium handling of the tissues was assessed. Specifically, ALLN (10 μ M) was added on Day 12 and incubated for 42 hours. Thapsigargin (1 μ M) was added on Day 13 and incubated for 24 hours. Nicorandil (1 μ M) was added on Day 14 and incubated for 30 minutes. Tissue contraction was recorded before and after

pharmaceutical treatment. Calcium transients were performed on Day 14 for all conditions, following previously defined protocol (Veldhuizen et al., 2020). Tissues were dosed with 0.2 µg/mL epinephrine in RPMI + B27 + insulin for 5 minutes at 37°C, then resultant contraction and calcium transients were recorded.

4.3.13 Microscopy

Phase contrast and immunofluorescence images were acquired using Zeiss Axio Observer Z1 equipped with Apotome2 (Zeiss) and ZenPro software. Time-lapse imaging of 15 seconds was recorded at 10X objective at 37°C on Day 14 to analyze contractile characteristics of heart on-a-chip tissues after pharmacological treatment. To calculate inter-beat interval variability of spontaneous contraction, we utilized our previously described method (Veldhuizen et al., 2020). Briefly, a custom written Matlab® code was used to extract contraction peaks and the time between peaks was calculated. The standard deviation of the duration between peaks was deemed the measure of inter-beat interval variability.

4.3.14 Immunofluorescent (IF) staining

For IF, all samples were first washed with PBS1X, then fixed with 4% PFA for 15-20 minutes at 37°C, then washed 3x with PBS-glycine. The subsequent protocol was dependent based on the target proteins.

For IF involving hERG, the samples were washed with PBS 1X 2x for 10 minute each, then permeabilized with 0.1% triton X-100 for 10 minutes at RT. The samples were incubated with 0.75M glycine in PBS for 10 minutes at RT, then washed with PBS1X.

The samples were then blocked in 10% goat serum for 30 minutes at 37°C. Following, primaries (mouse anti-sarcomeric α -actinin (SigmaAldrich), rabbit anti-connexin 43 (Abcam), mouse anti-TNNT2 (ThermoScientific), mouse anti-TE7 (SigmaAldrich), and rabbit anti-hERG (Abcam)) were diluted at 1:200 in 10% goat serum and added to the samples for 30 minutes at 37°C. Samples were washed 3x with PBS1X for 10 minutes each, then incubated with 1:1000 anti-mouse AlexaFluor488 and anti-rabbit AlexaFluor594 (in 1:1000 DAPI) for 30 minutes at 37°C. The samples were washed 3x with PBS1X before imaging.

For IF involving trilineage differentiation markers of EBs, the samples were washed 2X with PBS for 10 minutes each, then permeabilized for 30 minutes with IF buffer at 4°C. Following the samples were blocked for 1 hour with 10% goat serum at RT. Primary antibodies (mouse anti- α SMA (Santa Cruz, 1:50), rabbit anti-AFP (ThermoScientific, 1:50), mouse anti-TUJ1 (Fitzgerald, 1:1000)) were diluted in 10% goat serum and incubated at 4°C overnight. The next morning, samples were washed 3 for 10 minutes each with PBS1X. Secondaries (1:500) were diluted in 1:1000 DAPI, and added to the samples for 1 hour at RT. The samples were washed 3-5x for 10 min each w/PBS 1X before imaging.

For IF with the following antibodies: rabbit anti-Sox2 (Cell Signaling, 1:100), mouse anti-Nanog (Abcam, 1:200), rabbit anti-Vimentin (Cell-Signaling 1:200), and mouse anti-TE7 (SigmaAldrich, 1:100), samples were first washed with PBS-Tween20 for 10 minutes. Then, samples were permeabilized with IF buffer for 30 minutes at RT. Samples were blocked with 10% goat serum for 1 hour, then primaries were diluted in

10% goat serum and incubated with the samples for 1 hour at 37°C. The samples were washed 3x with PBS-Tween20 for 20 minutes each, then secondaries were added at 1:500 dilution in 1:1000 DAPI and incubated with samples for 45 minutes at 37°C. Following, samples were washed 3-5x with PBS-Tween20 for 10 minutes each, then imaged.

4.3.15 Quantitative real-time reverse transcription-PCR (qRT-PCR)

To perform gene expression, total RNA was extracted from cell samples with Total RNA Microprep kit (Zymo). RNA quality and concentration were assessed with Epoch Microplate Spectrophotometer. cDNA was synthesized from total RNA using iScript Reverse Transcriptase Supermix (BioRad) and iTaq Universal SYBR Green Supermix (BioRad) was used to perform qPCR on synthesized cDNA, with 18S as the housekeeping gene. Primers were validated via melt curve analysis and PCR product size verification. For qPCR, 8 µM dilution of forward and reverse primers was used for 10 µL reactions within 96-well plates, with 0.1 µL per of cDNA. The qPCR plates were analyzed with qTower, supplied by Dr. Barbara Smith.

4.3.16 Western Blot

To assess localization of hERG channels within CMs, the cells were lysed within their culture vessel, and the proteins were collected. Specifically, the culture plates were placed on ice, and the media was removed. The cells were washed with ice-cold PBS 1X, then 0.2 mL of ice-cold RIPA Lysis Buffer was added to each well of a 6-well plate. The cells were scrapped and collected into a chilled microcentrifuge tube. The solution was constantly agitated for 30 minutes at 4°C, then centrifuged at 12,000 RPM for 20 minutes

at 4°C. The supernatant was transferred to a new chilled microcentrifuge tube, then the protein concentration was measured with Epoch Microplate Spectrophotometer.

4.3.17 Statistical Analysis

All statistical analysis was performed using GraphPad Prism 6 and/or R Studio. Students t-test was used for Western Blot data, and two-way ANOVA was used for analysis of DCt values of gene expression data, as well as in the analysis of contractile signals and tissue alignment.

4.4 Results

4.4.1 Design of sgRNAs

To introduce a C->T edit at base 1591 to cause R531W in *KCNH2* using Big-TRIE gene editing technique, the sgRNA sequence was to be designed to place the target edit 12-18 bp upstream of a protospacer adjacent motif (PAM) that facilitates binding of spCas9, 5'-NGG-3', where N is any nucleotide. Therefore, we were limited to two different sgRNA sequences at this target that we could clone into the vector for base editing, with one 13 bp and the other 18 bp upstream from a suitable PAM sequence. Based on previously recorded editing efficiencies in relation to PAM location (Brookhouser et al., 2019), we moved forward with the sgRNA with PAM 13 bp downstream of the edit (Figure 4.1B). Within the editing window, there are two C's that may be affected: 1) the target C 13 bp upstream, and 2) bystander C 16 bp upstream. Editing at the target C would result in a change of amino acid from arginine to tryptophan (i.e., R531W), while an edit at the bystander C would be a silent mutation, as the amino acid would remain leucine.

4.4.2 Proof of principle editing R531W in *KCNH2* of HEK293

Once the guideRNAs were designed, we added bases to these oligonucleotides (Figure 4.1B) to create 5' overhangs that are compatible with BbsI digestion, as well as to allow binding of the DNA polymerase III. These sgRNA oligonucleotides were duplexed, then cloned into the sg(BFP->GFP) vector that contains two U6 promoters. After verification of sgRNA incorporation, the plasmid was transformed through *E. coli* and isolated. The plasmid (Addgene #138270) that was used to introduce the gene edit included sequences for spCas9n (Cas9(D10A)), the cytidine base editor AncBE4Max, and inhibitors of uracil DNA glycosylases (UGI) to prevent base excision repair that would change the edited U back to a C. This Cas9 plasmid, along with the sgRNA and BFP plasmids, were transfected into HEK293 cells to assess editing efficiency at the target site. 48 hours after transfection, flow cytometry was performed to analyze BFP⁺ and BFP⁺/GFP⁺ cells (with 11.9% of cells as BFP⁺/GFP⁺). Of the sorted BFP⁺/GFP⁺ cells, 6.25±2.06% incorporated the target C->T edit, and 72.5±2.38 incorporated the C->T edit at the bystander C. These reported editing efficiencies were higher than those in BFP⁺, DN, and US cells (Appendix Table E.1), highlighting the efficacy of using GFP expression as the reporter of transfection.

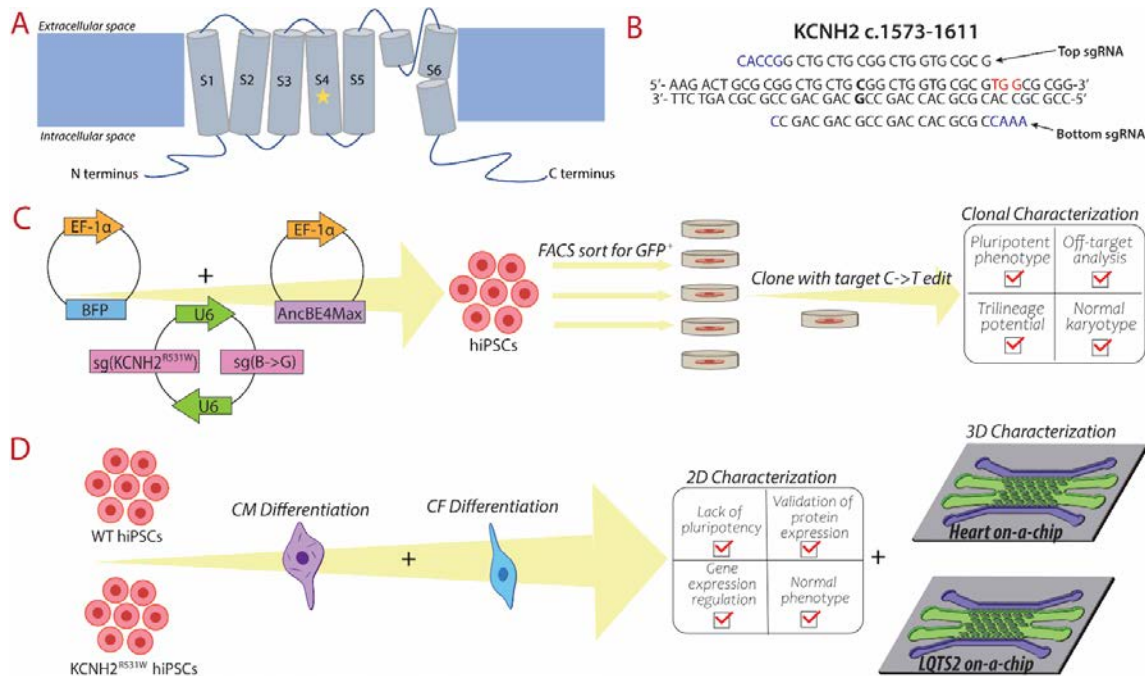


Figure 4.1: (A) Schematic of hERG channel structure. Overview of the design of (B) sgRNAs, (C) hiPSC transfection, and (D) hiPSC differentiation into cardiomyocytes and cardiac fibroblasts and subsequent characterization in 2D and 3D.

4.4.3 Generation and characterization of LQTS2 hiPSC line with R531W in KCNH2

As the gene-editing system we implemented proved capable of introducing the desired edit HEK293 cells, we moved forward to creating an edited hiPSC line. Particularly, hiPSCs were transfected through electroporation and delivery of the BFP plasmid, plasmid with the Cas9n sequence, and plasmid with the sgRNA sequences. We performed two rounds of hiPSCs transfection to ensure sufficient production of hiPSC clones. With both transfected hiPSC populations, FACS was performed, including bulk sorting to determine editing efficiencies, as well as single cell sorting of BFP⁺/GFP⁺ cells

into 96-well plates to create multiple different hiPSC clones. The clones were grown for 1-2 weeks, then passaged into 48-well plates and routinely expanded until culture in 6-well plates. The clones were cryopreserved and the gDNA analyzed at the target site to assess frequency of editing. The editing efficiency of BFP⁺/GFP⁺ hiPSCs was 4.5+/-2.08% for the target C->T edit, and 66.25+/-4.86% for the bystander C. The first round of transfection revealed 1 out of 12 viable clones that had the target heterozygous edit (deemed Clone 4), while 2 out of 17 viable clones had the edit in the second round (deemed Clones 2 and 9, Appendix Figure D.1A). Interestingly, overall, 22 out of 29 clones had a homozygous edit, and 7 out of 29 clones had a heterozygous edit, of C->T at the bystander C within the editing window, revealing the editing efficiency of Big-TREE as 100% for at least one allele at this site. The difference in editing efficiency at the target site compared to the bystander site corresponds with the finding in literature that base editing efficiency varies greatly depending on location of edit, due to a variety of confounding factors, including surrounding sequence and target base accessibility (Anzalone et al., 2020).

Detailed analysis was performed on the generated lines to assess maintenance of hiPSC characteristics and phenotype. All three generated clonal lines were subjected to pluripotency analysis, through IF and qPCR (Appendix Figure D.1B,C), revealing upregulation of pluripotency markers and thus hiPSC phenotype. Additionally, it was observed that all three clones had a lack of expression for CM as well as fibroblast expression (Appendix Figure D.1D,E). Lastly, the three clones were all differentiated into CMs to ensure cardiac differential potential even with KCNH2^{R531W}. Immunostaining for

sarcomeric α -actinin (SAA) (Appendix Figure D.2A) and gene expression analysis of cardiac genes (Appendix Figure D.2B) revealed successful CM differentiation of all generated hiPSC clones.

Of the edited $KCNH2^{R531W}$ hiPSC clones, Clone 4 was selected as the line to be used for all further experiments. We subjected this clone, hereon referred as “edited hiPSCs”, to further analysis through karyotyping, trilineage differentiation potential, and potential off-target analyses. The edited hiPSCs had high expression of pluripotency markers (Figure 4.2B), a normal euploid karyotype (Figure 4.2C), and spontaneously differentiated into the three layers (Figure 4.2E). As CRISPR/Cas9 editing techniques have the possibility to affect locations other than the target in the genome, we sought to assess potential off-target effects in our edited hiPSCs. Using CCTop, the top 4 possible offtarget loci were sequenced, including: Site 1: DSCR3, Site 2: KIAA1324, Site 3: TFR2, and Site 4: POU3F3. Primers were designed to target the particular locations on the gene where the predicted off target editing would occur (Supplemental Table 1), and no offtarget edits were found (Figure 4.2D).

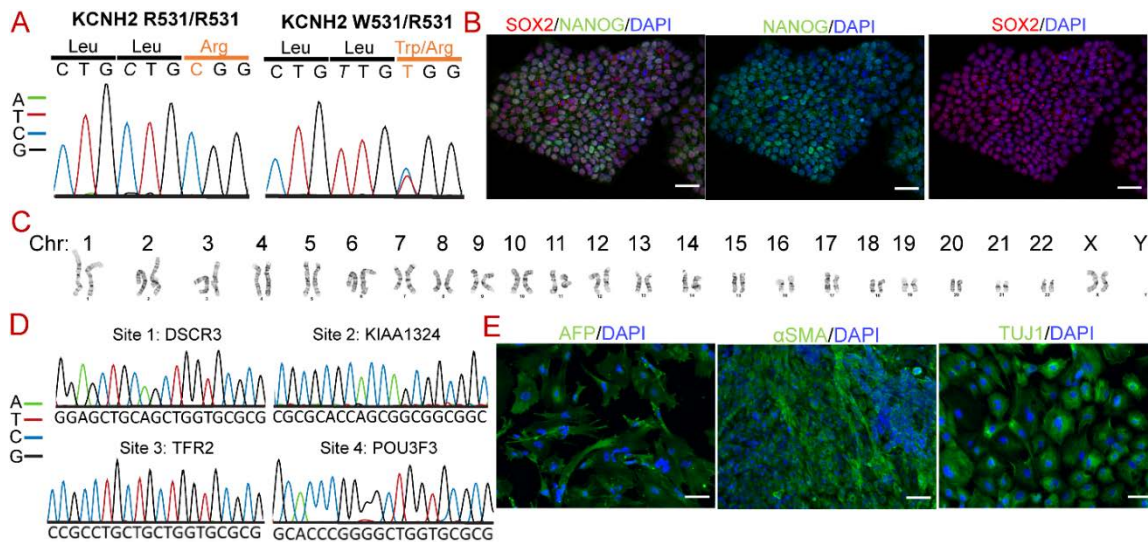


Figure 4.2: Creation and validation of hiPSCs line with R531W mutation in *KCNH2*

(A) Trace files of the target site in WT (left panel) and Edited (right panel) hiPSCs, showing a heterozygous edit that results in R531W. (B) Immunostaining of pluripotency markers, where SOX2=red and NANOG=green, (C) karyotype analysis, (D) potential off-target loci sequencing, and (E) trilineage potential of the edited hiPSC colony.

4.4.4 Characterization of isogenic stem cell-derived cardiac cells with *KCNH2*^{R531W} mutation

To investigate the pathophysiology of LQTS2 within a precisely controlled environment, we incorporated CRISPR/Cas9 gene editing techniques to introduce a point mutation in hiPSCs in *KCNH2*. To serve as control, we used the hiPSCs without the introduced mutation and deemed them as WT hiPSCs. After extensive analysis and confirmation of editing, both sets of hiPSCs were then differentiated into CMs and CFs (Figure 4.3). Both sets of CMs, and CFs were subject to characterization, via IF and

qPCR, to assess the phenotype and regulation of gene expression. CMs from both WT and KCNH2^{R531W} hiPSCs exhibit expression of striated sarcomeres and localized CX43 (Figure 4.3A), lack expression of pluripotency markers (Figure 4.3B) and demonstrate similar upregulation of an array of CM-specific genes (Figure 4.3C), with the only significant difference observed in MLC2A. As all CM-specific genes assayed had great upregulation, we suggest the difference in expression observed in MLC2A may be due to variabilities inherit in CM differentiation. Regardless, the edited hiPSCs demonstrated successful CM differentiation.

Additionally, CFs were differentiated from both WT and edited hiPSCs and their phenotypes were assessed. IF of the fibroblast markers, TE7 and vimentin (Figure 4.3D), lack of pluripotency markers (Figure 4.3E), and upregulation of ECM markers (Figure 4.3F) revealed successful CF differentiation of both types of hiPSCs. Importantly, we utilized commercially available hCFs (Lonza) as the positive control, and found no significant differences in gene expression of ECM markers of CFs differentiated from either WT or edited hiPSCs.

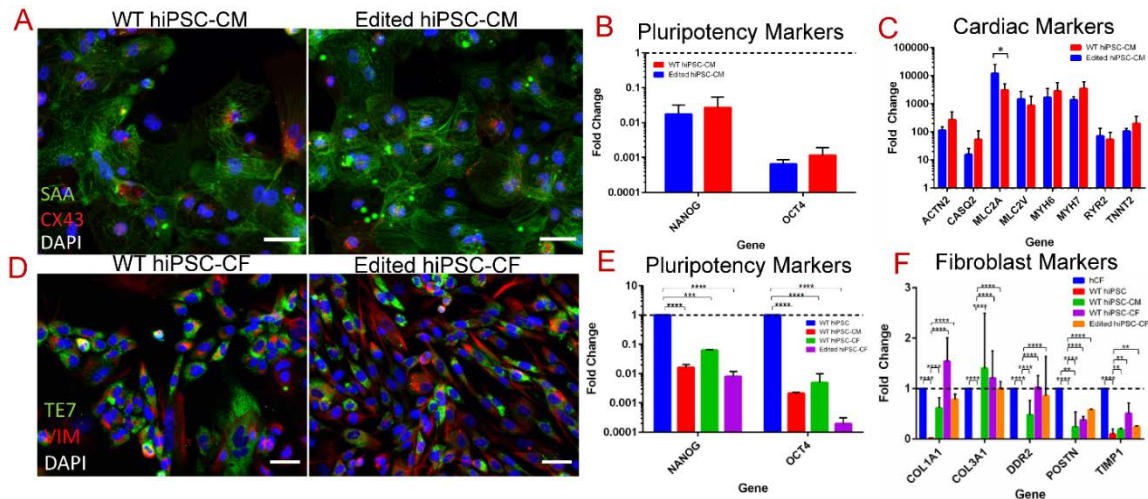


Figure 4.3: Characterization of isogenic cardiac cells differentiated from WT and Edited hiPSCs

(A-C) Characterization of CM differentiation of WT and edited hiPSCs, including (A) immunostaining for sarcomeric α -actinin (SAA), (B) lack of pluripotency marker expression, and (C) expression of CM-specific genes. (D-F) Characterization of CF differentiation of WT and edited hiPSCs, including (D) immunostaining for TE7 (green) and vimentin (red), (E) lack of pluripotency marker expression, and (F) expression of fibroblast-specific genes.

4.4.5 R531W and trafficking of hERG in stem cell-derived CMs

To study the effect of R531W mutation on hERG trafficking in stem cell-derived CMs, we performed Western Blotting for hERG1a on both WT and edited hiPSC-CMs. In normal hERG channel synthesis, the immature protein undergoes core glycosylation in the ER, resulting in a weight of 135 kDa. The immature protein is then transported to the Golgi apparatus and complex glycosylation occurs. The mature hERG channel, with a

final weight of hERG is 155 kDa, is then inserted into the plasma membrane (Thomas et al., 2003). When performing WB for hERG channels using an anti-hERG antibody, two bands occur at weights 135 kDa and 155 kDa, revealing levels of immature and mature protein, respectively. Therefore, WB has been used to identify protein trafficking defects, as evidenced by increased expression of 135kDa compared to 155 kDa hERG, that occur as a result of a mutation in *KCNH2* (C.L. Anderson et al., 2006; Delisle et al., 2003; Delisle et al., 2004; Gong et al., 2004; Mehta et al., 2014; Mesquita et al., 2019; Mura et al., 2017; Paulussen et al., 2002; Thomas et al., 2003).

In our data, we noted significantly increased expression ratio of 135kDa: 155 kDa hERG in the edited CMs compared to WT CMs (Figure 4.4A,B), suggesting the mutation has a role in protein trafficking. This finding was validated by the staining of TNNT2 and hERG of WT and edited CMs (Figure 4.4C-E), as more hERG is identified in WT CMs outside of the nucleus, while there is apparently higher expression of hERG in the nucleus of edited CMs.

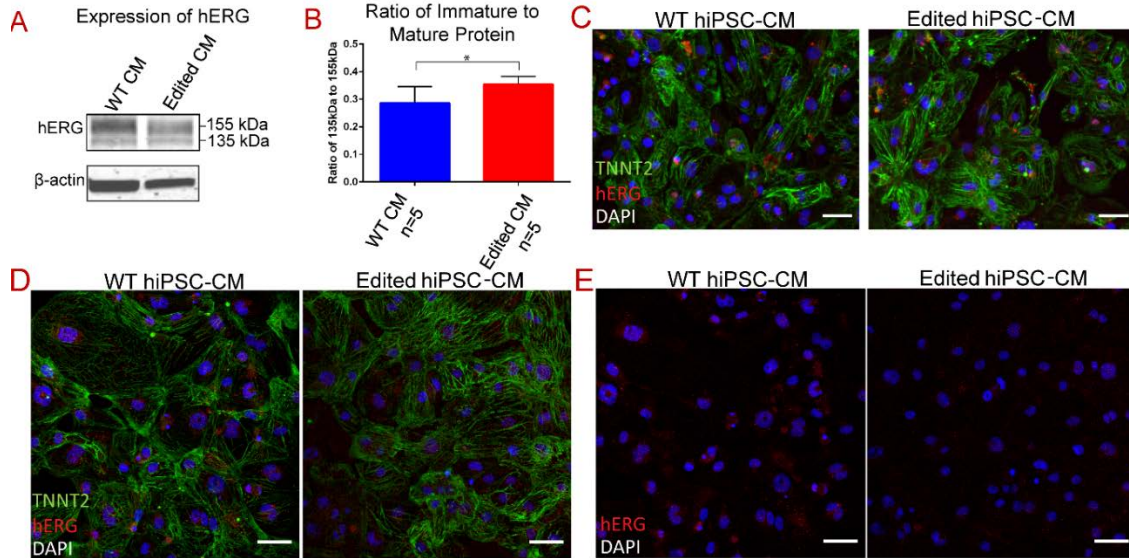


Figure 4.4: Trafficking of hERG in CMs differentiated from hiPSCs with R531W mutation in *KCNH2*. (A) Western blot for hERG1a and (B) densitometry analysis of 135 kDa to 155 kDa bands of WT and edited hiPSC-CMs. (C-D) Immunostaining of TNNT2 (green) and hERG (red) in WT and edited hiPSC-CMs, at (C) 20X, and (D) 40X. (E) Figures from (D) without TNNT2 staining to demonstrate localization of hERG in respect to nuclei of WT and edited hiPSC-CMs. * denotes p-value <0.05.

4.4.6 Development of LQTS2 tissues within 3D microfluidic chip

To model LQTS2 on-a-chip, we utilized our validated microfluidic heart on-a-chip as a platform, demonstrated to create anisotropic, 3D, mature co-cultured cardiac tissues (Veldhuizen et al., 2020). Specifically, hiPSC-CMs and hiPSC-CFs from WT and LQTS2, to form healthy cardiac tissue and LQTS2 on-a-chip, respectively, were encapsulated within a collagen-based hydrogel and injected into the microfluidic chip. The tissues were cultured within the devices for a total of 14 days. Baseline

characteristics of both WT and LQTS2-derived tissues were analyzed, via assessment of spontaneous beating parameters, calcium transients and stimulation with β -agonist (epinephrine). Analysis of alignment and cardiac markers of the tissues revealed similar tissue formation within the devices (Figure 4.5A,B). Specifically, both WT and LQTS2 tissues were aligned around the microposts within the chips, with elongated cells presenting with striated sarcomeres and abundant CX43 staining.

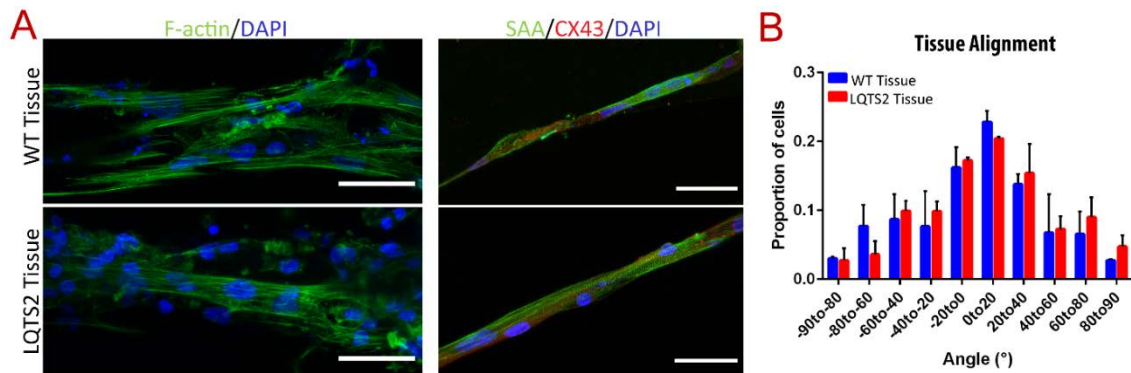


Figure 4.5: Development of Long QT Syndrome Type 2 on-a-chip. (A) Immunostaining of WT (top) and LQTS2 (bottom) tissues formed in microfluidic chip after 14 days. Left panel shows F-actin (green) and DAPI (blue) and right panel shows SAA (green), CX43 (red), and DAPI (blue). (B) Alignment analysis of nuclei within tissues at Day 14. (C-F) Representative calcium transients of 5 different ROIs in one video of WT tissue before (C) and after (E) epinephrine, and LQTS2 tissue before (D) and after (F) epinephrine. (G-H) Analysis of calcium transients from n=4 experiments, showing (G) iivRONavg and (H) iivRONstd. * denotes p-value <0.05 and ** denotes p-value <0.01.

4.4.8 Probing the rescue of LQTS2 tissues on-a-chip with pharmaceuticals

To further probe the mechanism of R531W mutation in *KCNH2* in mature hiPSC-derived cardiac tissues, we tested various pharmaceuticals, with different mechanisms of action, on the potential rescue of LQTS2 phenotype within the LQTS2 tissues on-a-chip. Specifically, in trafficking-deficient hERG channels (such as A561V (Kagan, Yu, Fishman, & McDonald, 2000; Mehta et al., 2014) and IVS9-28A/G (Mura et al., 2017)), ALLN, a proteasome inhibitor, has been found to aid in the rescue hERG trafficking due to mutation in hiPSC-CMs. If rescue with ALLN is demonstrated, then there is evidence that these particular mutations result in increased activity of proteasomes that act to degrade misfolded proteins, supporting the conclusion that the mutation disrupts protein trafficking to the plasma membrane. Another pharmaceutical, thapsigargin, has been used to probe the role of *KCNH2* mutations in hERG trafficking (Delisle et al., 2003). Thapsigargin is a sarcoplasmic/ER Ca^{2+} -ATPase (SERCA) inhibitor, which alters levels of Ca^{2+} in both the cytoplasm and the ER. Changes in Ca^{2+} levels then affect activity levels of calcium-dependent molecular chaperones in the ER, which in turn may affect protein folding. Therefore, *KCNH2* mutations (i.e., F805C (Delisle et al., 2003)) that prove responsive to thapsigargin are suggested to alter hERG trafficking through protein misfolding.

Mutations in *KCNH2* can also act in mechanisms of action different than through hERG channel trafficking, such as through production of dysfunctional hERG channels in the membrane or alteration of gating properties. Therefore, we additionally tested nicorandil, a I_{KATP} opener, that has been previously demonstrated to normalize prolonged

repolarization in LQTS2 hiPSC-CMs (Duncan et al., 2017). Specifically, nicorandil both activates potassium channels to enhance K^+ efflux and inhibits voltage-gated Ca^{2+} channels (Kukovetz, Holzmann, & Poch, 1992). It is suggested that if the phenotype of LQTS2 CMs is rescued with nicorandil, then the mechanism of action of the particular mutation is not specific to trafficking, therefore the mutation may instead act through altering hERG channel functionality.

Based on analysis of calcium transients (representative traces of WT tissues before and after epinephrine, and LQTS2 tissues before and after epinephrine can be seen in Figure 4.6A-D), important variables were extracted to assess tissues' response to pharmacological treatment and stimulation with β -agonist. To begin, the average interbeat interval variability (iiv) was determined from the 5 different ROIs within each acquired video, this variable is deemed iivRONavg and serves as a measure of overall tissue beating variability. Based on iivRONavg, treatment with ALLN causes a significantly increased variability in spontaneous beating in the ALLN-treated LQTS2 tissue when compared to control LQTS2 tissues (Figure 4.6E). After treatment with epinephrine, the LQTS2 tissues treated with thapsigargin have a significantly increased variability (iivRONavg) compared to the control LQTS2 tissues. Further, the LQTS2 tissues treated with thapsigargin and dosed with epinephrine have a significantly increased variability (iivRONavg) than the WT tissues treated with thapsigargin and dosed with epinephrine. The standard deviation of the interbeat interval variability of the 5 different ROIs per video is deemed as iivRONstd, which serves as a measure of differences/variability in the synchronicity within each ROI. Based on iivRONstd,

epinephrine causes a more arrhythmic tissue in the LQTS2 tissues, compared to the WT tissues in the control condition (Figure 4.6F). However, once any one of the pharmaceuticals are added, there is no significant difference, albeit p-values are near significant, in synchronicity (iivRONstd) between the LQTS2 and WT tissues after epinephrine dosing. This finding reveals that the treatments do serve to increase the synchronicity in the LQTS2 tissues compared to control conditions, however the LQTS2 tissues still trend with a higher variability than WT tissues in the conditions.

Interestingly, the LQTS2 tissues after treatment, before epinephrine, have a significantly increased asynchronicity (iivRONstd) in their spontaneous beating compared to WT when treated with ALLN for 42 hours. Additionally, the LQTS2 tissues after exposure to ALLN have a significantly higher asynchronicity (iivRONstd) in their spontaneous beating patterns compared to both control and nicorandil-treated LQTS2 tissues. These findings altogether suggest that a combinatorial treatment of the pharmaceuticals may serve to correct the LQTS2 tissues, therefore future experiments will investigate treating tissues simultaneously with multiple drugs.

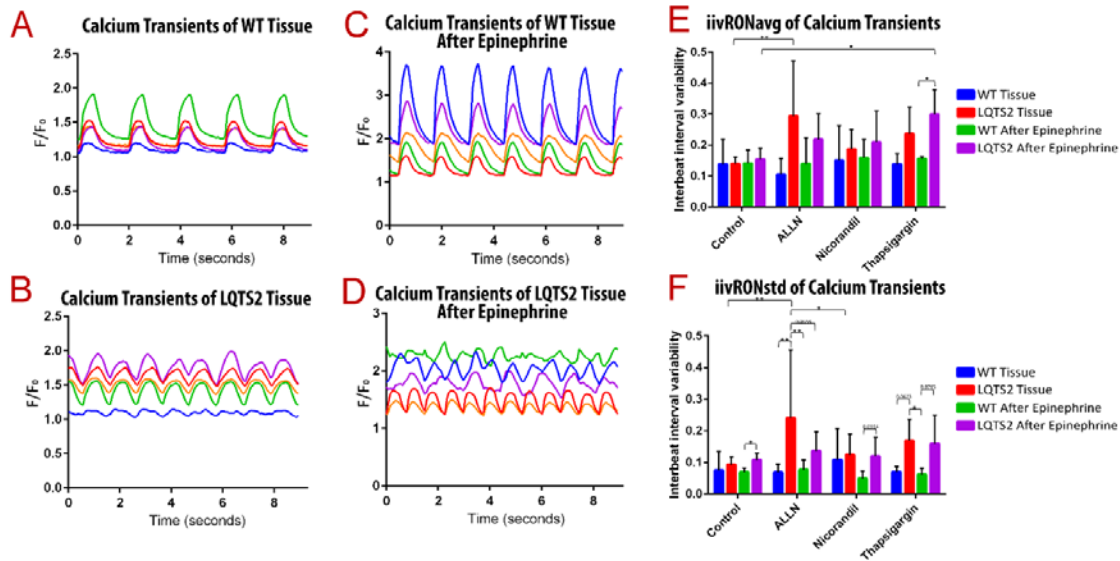


Figure 4.6: Pharmaceutical testing of Long QT Syndrome Type 2 on-a-chip. (A-D) Representative calcium transients of 5 different ROIs in one video of WT tissue before (A) and after (B) epinephrine, and LQTS2 tissue before (C) and after (D) epinephrine. (E-F) Analysis of calcium transients from $n=4$ experiments, showing (E) iivRONavg and (F) iivRONstd. * denotes p -value <0.05 and ** denotes p -value <0.01 .

4.5 Discussion

Long QT syndrome type 2 is a highly complex, and occasionally lethal, cardiac disease (Alders et al., 2003; Wallace et al., 2019). As such, much research has been completed on the implicated mutations in *KCNH2*, which encodes hERG, that result in LQTS2 to shed light on the best course of treatment for the disease (C. L. Anderson et al., 2014). Pathological mutations have been identified throughout the hERG protein, with differing mechanisms as to how the presence of the mutation leads to a decrease in I_{Kr} (Delisle et al., 2004; Ficker et al., 2000; Thomas et al., 2003). Thorough understanding of

both the identity and particular mechanism of an individual's mutation is essential for effective pharmacological treatment in LQTS2. To add to current understandings of LQTS2, we herein demonstrated study of the missense mutation R531W in *KCNH2*, introduced into hiPSCs, and how it leads to LQTS2 pathophysiology.

In this section of dissertation, we designed a gene-editing system, using Big-*TREE*, to introduce the mutation c.C1591T both in HEK293 cells, as validation, and in hiPSCs. Extensive characterization of the generated clones of edited hiPSCs revealed maintenance of hiPSC pluripotency, phenotype, and differentiation potential, as well as a lack of off-target gene-editing effects. With the validated, edited hiPSCs, we presented successful differentiation of isogenic cardiac cells (both CMs and CFs), and further characterized the role of R531W mutation in these cardiac cells.

Mutations in *KCNH2* can lead to loss of function, gain of function, non-functional, or trafficking-deficient hERG channels. In recent works, a significant amount of *KCNH2* mutations have been found to affect trafficking of hERG to the plasma membrane, leading to sequestering of functional and non-functional channels in the ER (C.L. Anderson et al., 2006; Delisle et al., 2003; Gong et al., 2004; Mehta et al., 2014; Mesquita et al., 2019; Mura et al., 2017; Paulussen et al., 2002; Thomas et al., 2003). However, most of these studies have been completed in 2D and/or in heterologous systems. In this work, we present the novel study of R531W mutation in *KCNH2* in CMs differentiated from hiPSCs, both in 2D and 3D. We found R531W mutation in *KCNH2* in hiPSC-CMs led to significantly more immature hERG (135 kDa) in a ratio to mature hERG (155 kDa) than WT hiPSC-CMs, suggesting that the mutation causes sequestration

of the immature hERG channels in the ER. A previous study focused on heterologous expression of hERG in HEK293 cells found that R531W did not appear to affect the trafficking (McBride et al., 2013). However, findings regarding LQTS2 mutations have been found to differ when expressed in hiPSC-CMs over studies previously done in heterologous systems, due to the hindering lack of accurate recapitulation of CM biology that heterologous systems offer (Paulussen et al., 2002). For example, Paulussen et al. discovered T65P in *KCNH2* not only affects channel activation, as previously found in heterologous systems, however it additionally plays a significant role in trafficking of hERG channels (Paulussen et al., 2002). Additional studies into heterologous systems have demonstrated the important role of the arginine residue at position 531 in normal gating of Kv11.1 (McBride et al., 2013; Piper et al., 2005; Piper, Rupp, Sachse, Sanguinetti, & Tristani-Firouzi, 2007; Subbiah et al., 2004; M. Zhang et al., 2005; M. Zhang, Liu, & Tseng, 2004), as introducing mutations at R531 induced the greatest perturbation in channel opening than other mutations in the S4 domain. Our findings suggest the role of R531 is crucial in hERG function, both in channel gating and trafficking to the plasma membrane.

In summary, we demonstrated the development of isogenic 3D cardiac tissues with R531W mutation in *KCNH2* within our established microfluidic device. The resultant anisotropic tissues have great potential in the study of LQTS2 on-a-chip.

4.6 Conclusion

In conclusion, this manuscript details the creation and study of LQTS2 on-a-chip. Particularly, we described creation of an hiPSC line with R531W mutation in *KCNH2*

with Big-TREE editing technique. Additionally, we thoroughly validated the hiPSC line to confirm maintenance of hiPSC characteristics, including pluripotency and trilineage differentiation potential, as well as the lack of off-target editing. Further, we differentiated the edited hiPSC line into both cardiomyocytes and cardiac fibroblasts and validated the phenotypes through gene expression and immunofluorescence of the differentiated cells. Additionally, we investigated the effect of the base mutation on hERG channel function and localization. hERG localization was analyzed through immunofluorescent staining for hERG and Western blotting for hERG protein expression. The function of the hERG channel was analyzed through patch clamp techniques to measure I_{Kr} . Further, the edited hiPSC-CMs and CFs were encapsulated in a 3D collagen-based hydrogel and incorporated in our novel microfluidic platform to create both healthy and LQTS2 heart on-a-chip tissues. The functionality of the 3D tissues was assessed, and potential rescue of the diseased phenotype was analyzed through administration of pharmaceuticals with differing mechanisms of action, to further probe the biological significance of R531W in *KCNH2* in LQTS2 onset.

CHAPTER 5

CONCLUSIONS AND FUTURE DIRECTIONS

This final chapter details achievements that have been made under each of the above specific aims and provides discussion and insights into directions for future research.

5.1 Significance and Contributions

5.1.1 Specific Aim 1

In this Aim, we described the development of a microfluidic platform for anisotropic cardiac tissue formation, notably with both rat-derived and human stem cell-derived CMs. We described the optimal conditions to form 3D tissue with co-cultured cardiac cells within the microfluidic device, which slightly vary between the rat-derived and human-derived cardiac cells. Specifically, it was determined that optimal culture conditions for rat-derived cardiac cells were 4:1 CM:CF ratio, fibrin:collagen hydrogel, 30×10^6 cells/mL cell density, and 2-week culture period within the device. The human stem cell-derived CMs had optimal culture conditions at 4:1 CM:CF ratio, collagen (2 mg/mL) hydrogel supplemented with 20% Matrigel, 35×10^6 cells/mL cell density, and 2-week culture period. Once these culture conditions were optimized, we sought to determine the optimal design of the heart on-a-chip microfluidic device, particularly in regards to the architecture of the innate microposts, to induce anisotropic cardiac tissue formation. Specifically, we tested different shapes of microposts, including hexagonal and elliptical, as well as horizontal and vertical spacing between microposts, resulting in 4 different designs. It was observed that elliptical microposts and the larger vertical post

spacing (200 μm) induced the thickest, aligned tissues, therefore we determined Design 1 to be the optimal, final design for the microfluidic devices.

Next, we sought to investigate the specific effect of the innate microposts within the microfluidic device on tissue formation, characteristics, and function. To do so, we created microfluidic devices that lack the microposts to serve as 3D isotropic controls, and we formed identical tissues within the devices with and without posts, as well as seeded cells in 24-well plates to serve as 2D controls. Overall, culture within a 3D environment (i.e., no post and post devices) results in enhanced expression in maturation genes as compared to 2D controls. Additionally, it was revealed that the innate microposts serve as mesoscopic surface topography and induce high degrees of alignment. Further, the devices with microposts induced increased beating synchronicity, highly striated sarcomeric structure, calcium transients, and responsiveness to β -agonists, as compared to devices without posts.

5.1.2 Specific Aim 2

This Aim described the use of the microfluidic device developed in Specific Aim 1 as the platform to form anisotropic 3D cardiac tissue to model ischemic disease. Specifically, this Aim focused on creating a model of myocardial infarction using the mature, human stem cell-derived cardiac tissue formed in the microfluidic device. Our particular hypothesis was that, through exposure of cardiac tissues in the device to extended hypoxia, the cardiac tissues would respond in a global manner to the ischemic insult similar to what has been demonstrated after myocardial ischemia or infarction. We also sought to investigate the use of physioxic conditions (i.e., 5% O_2), in addition to the

standard hyperoxic conditions (i.e., 21% O₂) that are normally used for *in vitro* experiments. After 24 hours of exposure to 1% O₂, we subjected the cardiac tissues to extensive analyses, revealing fibrotic response, contractile dysregulation, and transcriptomic regulation, similar to the biological events that occur in myocardial ischemia. In specifics, we found an upregulation of α SMA expression in hypoxic tissues, compared to both physioxic and hyperoxic tissues. Interestingly, we noted increased contractile dysregulation in hypoxic conditions compared to physioxic tissues. We further analyzed the transcriptional regulation of physioxic and hypoxic tissues, revealing upregulation of glycolytic pathways and downregulation of oxidative phosphorylation in tissues exposed to hypoxia. Additionally, we briefly investigated the effect of reperfusion on cell viability, with significantly increased amounts of cell death in tissues exposed to both 1 hour and 24 hours of reperfusion.

5.1.3 Specific Aim 3

In this Aim, we focused on the creation and study of LQTS2 on-a-chip with gene-edited hiPSCs. To accomplish this, we utilized CRISPR/Cas9 gene-editing to introduce a missense mutation in *KCNH2* that resulted in an amino acid change from arginine to tryptophan at codon 531 (R531W). We first demonstrated successful transfection and editing with this system on HEK293 cells, then we moved on to creating an edited hiPSC line. Specifically, we successfully transfected hiPSCs, sorted single cells and grew clones, assessed editing at target site and selected those clones with the incorporated edit. The edited hiPSC clones were thoroughly analyzed to ensure maintenance of hiPSC pluripotency, phenotype, and lack of off-target edits. The edited hiPSCs were then

successfully differentiated into both CMs and CFs. The characteristics of the differentiated cardiac cells were assessed to 1) validate the phenotypes of the differentiated cell type and 2) analyze the effect of R531W mutation in *KCNH2*. Then, the isogenic cardiac cells were combined within a 3D collagen:Matrigel hydrogel and incorporated in the demonstrated heart on-a-chip platform, developed in Specific Aim 1, to create LQTS2 on-a-chip tissues. The functionality of the tissues was assessed, in comparison to healthy cardiac tissue comprised of WT hiPSC-CMs and hiPSC-CFs. Additionally, we investigated pharmacological treatment in the rescue of disease phenotype within the heart on-a-chip platform.

5.1.4 Contributions

We present herein the collection of works based on this research that were published in peer-reviewed journals and conference presentations.

Journal Articles:

1. **Veldhuizen, J.**, Chavan, R., Moghadas, B., Park, J., Kodibagkar, V., Migrino, R.Q., Nikkhah, M., "Cardiac Ischemia on-a-Chip to Investigate Cellular and Molecular Response of Myocardial Tissue Under Hypoxia", *Biomaterials*, (Pending Revisions)
2. **Veldhuizen, J.** & Nikkhah, M., "Method to Develop 3D Organized Human Cardiac Tissue Within a Microfluidic Platform", *Journal of Visual Experiments (JoVE)*, 127, (2021)

3. **Veldhuizen, J.**, Cutts, J., Brafman, D.A., Migrino, R.Q., Nikkhah, M.,
“Engineering anisotropic human stem cell-derived three-dimensional
cardiac tissue on-a-chip”, *Biomaterials*, 256, (2020)
4. **Veldhuizen, J.**, Migrino, R.Q. & Nikkhah, M. “Three-dimensional
microengineered models of human cardiac diseases”, *Journal of Biological
Engineering*, 13, 29, (2019)
5. Patino-Guerrero, A., **Veldhuizen, J.**, Zhu, W., Migrino, R.Q., Nikkhah, M.,
“Three-dimensional scaffold-free microtissues engineered for cardiac
repair”, *J. Mater. Chem. B*, 8, (2020)
6. Saini, H., Eliato, K.R., **Veldhuizen, J.**, Zare, A., Alaam, M., Silva, C.,
Truong, D., Mouneimne, G., LaBaer, J., Ros, R., Nikkhah, M., “The Role
of Tumor-Stroma Interactions on Desmoplasia and Tumorigenicity within a
Microengineered 3D Platform”, *Biomaterials*, 247, (2020)
7. Karamanova, N., Truran, S. Serrano, G.E., Beach, T.G., Madine, J.,
Weissig, V., Davies, H.A., **Veldhuizen, J.**, Nikkhah, M., Hansen, M.,
Zhang, W., D’Souza, K., Franco, D.A., Migrino, R.Q., “Endothelial
immune activation by medin: potential role in cerebrovascular disease and
reversal by monosialoganglioside-containing nanoliposomes”, *Journal of
American Heart Association (JAHA)*, 9, (2020)

Conference Presentations:

1. **Veldhuizen, J.**, Cutts, J., Camacho, Z., Soldevila, M., Brafman, D.,
Migrino, R.Q., Nikkhah, M., “Modeling Stem Cell-Derived Human

Myocardium in a Microengineered Tissue Platform”, BMES Annual Meeting, Philadelphia, PA (Oct. 2019), Platform Presentation.

2. **Veldhuizen, J.**, Cutts, J., Camacho, Z., Brafman, D., Migrino, R.Q., Nikkhah, M., “Microengineering of a Three-Dimensional Heart on-Chip Tissue Model”, BMES Annual Meeting, Atlanta, GA (Oct. 2018), Platform Presentation

Conference Posters:

1. **Veldhuizen, J.**, Chavan, R., Moghadas, B., Park, J., Kodibagkar, V., Migrino, R.Q., Nikkhah, M., "Development of Three-Dimensional Stem Cell-Derived Cardiac Ischemia on-a-Chip", ABRC-Flinn Conference, Virtual (Feb. 2021), Poster Presentation.
2. **Veldhuizen, J.**, Truran, S., Karamanova, N., Davies, H., Madine, J., Migrino, R.Q., Nikkhah, M., “Studying Neuroinflammation Using A Novel Microfluidic Vascular Brain-On-A-Chip”, BMES Annual Meeting, Virtual (Oct. 2020), Poster Presentation.

5.2 Project Challenges

Throughout the duration of the research supporting this dissertation, we encountered a good share of challenges that were addressed to the best of our ability. For instance, the challenges faced in Aim 1 arose mostly in performing successful CM differentiation of the human stem cells. This project was the first in the lab to necessitate stem cell culture, which in itself required optimization and dynamic modifications depending on cell

morphology. Further, once we mastered stem cell culture, we attempted CM differentiation using a few different protocols defined in the literature. Through collaborations and extensive research, we were finally able to repeatedly differentiate CMs from different types of stem cells with great success. In regards to microfluidic device design, we encountered challenges in identifying the optimal device topology. Multiple design iterations of the innate microposts were studied to determine the optimal layout for anisotropic cardiac tissue formation, resulting in final micropost geometry of elliptical shape with 500 μm in length, 100 μm in width, and 200 μm of vertical post spacing. Similarly, a variety of hydrogel compositions and co-culture ratios were studied using rat-derived cardiac cells to identify the optimal variables for 3D healthy cardiac tissue formation. Once we identified the ideal design and experimental ratios, we transitioned to incorporation of human stem cell-derived CMs, where we had to again re-optimize the hydrogel composition and cell density.

Another challenge in this dissertation was encountered during completion of Aim 2. Specifically, we faced technical difficulties in regards to implementing hypoxic environments to model myocardial ischemia within the heart on-a-chip. This challenge was met once we secured collaboration, enabling the use of an incubator with the necessary gas sensors and inputs to establish the desired hypoxic environment. Likewise, we also faced the technical difficulty in maintaining the hypoxic environment of the tissue samples before and during sample preparation, as desired to prevent reperfusion/reoxygenation of tissues. To the best of our ability, we maintained the tissues

within the hypoxic environment during enzymatic digestion and fixing to collect the cells and stain the tissues, respectively.

Lastly, we encountered difficulties in the successful introduction of the particular gene-edit (c.C1591T in *KCNH2*) in hiPSCs (Aim 3). Big-TREE, the system that was used in collaboration with Dr. Brafman's lab, is highly optimized, generally reporting over 90% editing efficiency (Brookhouser et al., 2019). However, as extensively defined in literature (Anzalone et al., 2020), base editing efficiency is highly dependent on the type of base editor, accessibility of target site, and sequence of surrounding bases. We found that the location of the target base (c.C1591T) proved rather difficult to edit with BigTREE, rendering only 10.3% of sorted clones having a heterozygous edit, and no clones having a homozygous edit. However, we addressed this challenge by increasing the number of wells we sorted into, thereby increasing the chances of having more clones, to offset the low percentage of editing efficiency. By doing so, we generated a total of 29 viable clones, with 3 out of the 29 with the desired edit. We expanded and partially characterized all 3 clones to ensure normal characteristics, and to have a backup clone in case one revealed abnormal karyotype or off-target edits. Luckily, the first clone we analyzed further had a normal karyotype and no off-target effects, so we were able to use this clone for all sequential experiments.

5.3 Future Directions

5.3.1 Optimization of myocardial tissue-on-chip model

The microfluidic model presented in Chapter 2 could be further improved in future works for enhanced functional measurements particularly for those of great

importance to cardiac tissue studies, such as contractile force measurements. To address the need for real-time measurement of force in disease modeling and pharmaceutical testing applications, an innate method to measure contractile force is of great importance. Future works could investigate the use of innate, free-standing micropillar arrays, capable of force measurement, similar to the approach described in (Schaaf et al., 2011), within the microfluidic device to allow for real-time force monitoring. Additionally, methods to enhance the platform's ability to model the adult myocardium, such as induction of a pronounced myosin isoform switch from β to α , could be implemented. For example, sustained electrical conditioning has been demonstrated to enhance the electrophysiology and transcriptional signature of hPSC-derived CMs. However, a rather complicated setup is necessary to incorporate sustained external stimulation, and our model is advantageous in its low cost and ease of creation. Similarly, an enlarged version of the platform could be constructed to allow for a large cell population to select for CMs for downstream analyses, however such a platform would negate the many advantages of a microfluidic platform, i.e., high throughput, minimal cell/reagent necessary, and reduced variation with input differentiation populations. To further take advantage of the microfluidic nature of the described platform, a future work could involve implantation of continuous fluid flow through the media channels to enable enhanced nutrient supply and dynamic culture conditions, which have recently been demonstrated to enhance cardiac tissue function (Jackman et al., 2016).

5.3.2 Investigation into reperfusion after ischemic injury

To attempt to reduce the tissue damage that occurs during ischemia reperfusion injury, ischemic pre-conditioning has been a subject of prior studies (Yadid et al., 2020). The myocardial ischemic model within an anisotropic 3D cardiac on-a-chip platform that we described in Chapter 3 could be used to implement studies into the role of ischemic pre-conditioning. Therefore, future works could further focus on the role of ischemia pre-conditioning on development of injury after reperfusion. Importantly, the microfluidic nature of the model could be leveraged in its capability for constant media flow. In another regard, to advance the physiological relevancy of the model, we could incorporate fluid flow in the next generation to simulate blood flow through the tissue during cardiac tissue culture. Particularly during ischemia, the flow could be halted to allow for buildup of metabolic waste due to lack of washout, then the media flow could be reintroduced to measure reperfusion injury. Similarly, incorporation of fluid flow could be used to model introduction of immune cells to the diseased site via blood flow. Another advantage of the use of a microfluidic model is in its ability to induce a gradient of hypoxia and nutrient diffusion across the channel, to better model the differential gradient that is experienced in the various layers of the heart (i.e., epicardium, myocardium, and endocardium).

5.3.3 Further studies into rescue of LQTS2 stem cells and on-a-chip tissues

Future studies will involve more extensive investigation into the pharmacological rescue of LQTS2 on-a-chip tissues, particularly through combinatorial pharmaceutical treatment and possibly through dosage testing. We are also completing patch-clamp studies to measure the I_{K_r} current in both WT and edited hiPSC-CMs to validate the

disease phenotype through electrophysiological assessment. Additionally, there is a commercially available hiPSC line, derived from patient skin fibroblasts, that harbors the mutation R531W within *KCNH2*, however they have proven quite difficult to obtain due to regulatory issues and international sourcing. Therefore, if we are successful in the attainment of these cells, future directions could include investigating the pathological phenotypes of the patient-specific tissues and comparing to the gene-edited tissues. Additionally, we could utilize gene-editing technology to rescue the patient cells, through correcting the base mutation (c.1591) from T->C, then investigate the functionality of the formed tissues. In this method, we could explore if there are confounding factors that lead to the onset of LQTS2, or if correction of the base mutation rescues the disease phenotype.

REFERENCES:

- Abe, H., Semba, H., & Takeda, N. (2017). The Roles of Hypoxia Signaling in the Pathogenesis of Cardiovascular Diseases. *J Atheroscler Thromb*, *24*(9), 884-894. doi:10.5551/jat.RV17009
- Abu-El-Rub, E., Sequiera, G. L., Sareen, N., Yan, W., Moudgil, M., Sabbir, M. G., & Dhingra, S. (2019). Hypoxia-Induced 26s Proteasome Dysfunction Increases Immunogenicity of Mesenchymal Stem Cells. *Cell Death Dis*, *10*(2), 90. doi:10.1038/s41419-019-1359-x
- Acun, A., Nguyen, T. D., & Zorlutuna, P. (2019). In Vitro Aged, Hipscc-Origin Engineered Heart Tissue Models with Age-Dependent Functional Deterioration to Study Myocardial Infarction. *Acta Biomater*, *94*, 372-391. doi:10.1016/j.actbio.2019.05.064
- Acun, A., Vural, D. C., & Zorlutuna, P. (2017). A Tissue Engineered Model of Aging: Interdependence and Cooperative Effects in Failing Tissues. *Sci Rep*, *7*(1), 5051. doi:10.1038/s41598-017-05098-2
- Agarwal, A., Goss, J. A., Cho, A., McCain, M. L., & Parker, K. K. (2013). Microfluidic Heart on a Chip for Higher Throughput Pharmacological Studies. *Lab Chip*, *13*(18), 3599-3608. doi:10.1039/c3lc50350j
- Agrawal, V., Gupta, J. K., Qureshi, S. S., & Vishwakarma, V. K. (2016). Role of Cardiac Renin Angiotensin System in Ischemia Reperfusion Injury and Preconditioning of Heart. *Indian Heart J*, *68*(6), 856-861. doi:10.1016/j.ihj.2016.06.010
- Alders, M., Bikker, H., & Christiaans, I. (2003). Long Qt Syndrome. *GeneReviews*.
- Alford, P. W., Feinberg, A. W., Sheehy, S. P., & Parker, K. K. (2010). Biohybrid Thin Films for Measuring Contractility in Engineered Cardiovascular Muscle. *Biomaterials*, *31*(13), 3613-3621. doi:10.1016/j.biomaterials.2010.01.079
- Ameen, C., Strehl, R., Bjorquist, P., Lindahl, A., Hyllner, J., & Sartipy, P. (2008). Human Embryonic Stem Cells: Current Technologies and Emerging Industrial Applications. *Crit Rev Oncol Hematol*, *65*(1), 54-80. doi:10.1016/j.critrevonc.2007.06.012
- Anderson, C. L., Delisle, B. P., Anson, B. D., Kilby, J. A., Will, M. L., Tester, D. J., . . . January, C. T. (2006). Most Lqt2 Mutations Reduce Kv11.1 (Herg) Current by a Class 2 (Trafficking-Deficient) Mechanism. *Circulation*, *113*, 365-373.

- Anderson, C. L., Kuzmicki, C. E., Childs, R. R., Hintz, C. J., Delisle, B. P., & January, C. T. (2014). Large-Scale Mutational Analysis of Kv11.1 Reveals Molecular Insights into Type 2 Long Qt Syndrome. *Nat Commun*, 5.
- Ann Ran, F., Hsu, P. D., Wright, J., Agarwala, V., Scott, D. A., & Zhang, F. (2013). Genome Engineering Using the Crispr-Cas9 System. *Nature Protocols*, 8, 2281-2308.
- Annabi, N., Selimovic, S., Acevedo Cox, J. P., Ribas, J., Afshar Bakooshli, M., Heintze, D., . . . Khademhosseini, A. (2013). Hydrogel-Coated Microfluidic Channels for Cardiomyocyte Culture. *Lab Chip*, 13(18), 3569-3577. doi:10.1039/c3lc50252j
- Annabi, N., Tsang, K., Mithieux, S. M., Nikkhah, M., Ameri, A., Khademhosseini, A., & Weiss, A. S. (2013). Highly Elastic Micropatterned Hydrogel for Engineering Functional Cardiac Tissue. *Adv Funct Mater*, 23(39). doi:10.1002/adfm.201300570
- Anzalone, A. V., Koblan, L. W., & Liu, D. R. (2020). Genome Editing with Crispr-Cas Nucleases, Base Editors, Transposases and Prime Editors. *Nat Biotechnol*, 38(7), 824-844. doi:10.1038/s41587-020-0561-9
- Ariyasinghe, N. R., Reck, C. H., Viscio, A. A., Petersen, A. P., Lyra-Leite, D. M., Cho, N., & McCain, M. L. (2017). Engineering Micromyocardium to Delineate Cellular and Extracellular Regulation of Myocardial Tissue Contractility. *Integr Biol (Camb)*, 9(9), 730-741. doi:10.1039/c7ib00081b
- Ban, K., Bae, S., & Yoon, Y. S. (2017). Current Strategies and Challenges for Purification of Cardiomyocytes Derived from Human Pluripotent Stem Cells. *Theranostics*, 7(7), 2067-2077. doi:10.7150/thno.19427
- Bassan, R., Potsch, A., Maisel, A., Tura, B., Villacorta, H., Nogueira, M. V., . . . Moutinho, M. A. (2005). B-Type Natriuretic Peptide: A Novel Early Blood Marker of Acute Myocardial Infarction in Patients with Chest Pain and No St-Segment Elevation. *Eur Heart J*, 26, 234-240.
- Begg, K., & Tavassoli, M. (2020). Inside the Hypoxic Tumour: Reprogramming of the Ddr and Radioresistance. *Cell Death Discovery*, 6, 77.
- Bellin, M., Casini, S., Davis, R. P., D'Aniello, C., Haas, J., Ward-van Oostwaard, D., . . . Mummery, C. L. (2013). Isogenic Human Pluripotent Stem Cell Pairs Reveal the Role of a Kcnh2 Mutation in Long-Qt Syndrome. *EMBO J*, 32(24), 3161-3175. doi:10.1038/emboj.2013.240

- Benjamin, E., Blaha, M., Chiuve, S., Cushman, M., Das, S., Deo, R., de Ferranti, S., Floyd, J. (2017). *Heart Disease and Stroke Statistics-2017 Update*.
- Bergstrom, G., Christoffersson, J., Schwanke, K., Zweigerdt, R., & Mandenius, C. F. (2015). Stem Cell Derived in Vivo-Like Human Cardiac Bodies in a Microfluidic Device for Toxicity Testing by Beating Frequency Imaging. *Lab Chip*, *15*(15), 3242-3249. doi:10.1039/c5lc00449g
- Besser, R. R., Ishahak, M., Mayo, V., Carbonero, D., Claire, I., & Agarwal, A. (2018). Engineered Microenvironments for Maturation of Stem Cell Derived Cardiac Myocytes. *Theranostics*, *8*(1), 124-140. doi:10.7150/thno.19441
- Bian, W., Jackman, C. P., & Bursac, N. (2014). Controlling the Structural and Functional Anisotropy of Engineered Cardiac Tissues. *Biofabrication*, *6*(2), 024109-024109. doi:10.1088/1758-5082/6/2/024109
- Bian, W., Liao, B., Badie, N., & Bursac, N. (2009). Mesoscopic Hydrogel Molding to Control the 3d Geometry of Bioartificial Muscle Tissues. *Nat Protoc*, *4*(10), 1522-1534. doi:10.1038/nprot.2009.155
- Binah, O., Dolnikov, K., Sadan, O., Shilkrut, M., Zeevi-Levin, N., Amit, M., . . . Itskovitz-Eldor, J. (2007). Functional and Developmental Properties of Human Embryonic Stem Cells-Derived Cardiomyocytes. *J Electrocardiol*, *40*(6 Suppl), S192-196. doi:10.1016/j.jelectrocard.2007.05.035
- Birla, R. K., Borschel, G. H., Dennis, R. G., & Brown, D. L. (2005). Myocardial Engineering in Vivo: Formation and Characterization of Contractile, Vascularized Three-Dimensional Cardiac Tissue. *Tissue Eng*, *11*(5-6), 803-813. doi:10.1089/ten.2005.11.803
- Blalock, E. M., Chen, K. C., Stromberg, A. J., Norris, C. M., Kadish, I., Kraner, S. D., . . . Landfield, P. W. (2005). Harnessing the Power of Gene Microarrays for the Study of Brain Aging and Alzheimer's Disease: Statistical Reliability and Functional Correlation. *Ageing Res Rev*, *4*(4), 481-512. doi:10.1016/j.arr.2005.06.006
- Boudou, T., Legant, W. R., Mu, A., Borochin, M. A., Thavandiran, N., Radisic, M., . . . Chen, C. S. (2012). A Microfabricated Platform to Measure and Manipulate the Mechanics of Engineered Cardiac Microtissues. *Tissue Eng Part A*, *18*(9-10), 910-919. doi:10.1089/ten.TEA.2011.0341
- Braam, S. R., Tertoolen, L., van de Stolpe, A., Meyer, T., Passier, R., & Mummery, C. L. (2010). Prediction of Drug-Induced Cardiotoxicity Using Human Embryonic Stem

- Cell-Derived Cardiomyocytes. *Stem Cell Res*, 4(2), 107-116. doi:10.1016/j.scr.2009.11.004
- Brandao, K. O., Tabel, V. A., Atsma, D. E., Mummery, C. L., & Davis, R. P. (2017). Human Pluripotent Stem Cell Models of Cardiac Disease: From Mechanisms to Therapies. *Dis Model Mech*, 10(9), 1039-1059. doi:10.1242/dmm.030320
- Brandao, K. O., van den Brink, L., Miller, D. C., Grandela, C., van Meer, B. J., Mol, M. P. H., . . . Davis, R. P. (2020). Isogenic Sets of Hpsc-Cms Harboring Distinct Kcnh2 Mutations Differ Functionally and in Susceptibility to Drug-Induced Arrhythmias. *Stem Cell Reports*, 15(5), 1127-1139. doi:10.1016/j.stemcr.2020.10.005
- Bray, M. A., Sheehy, S. P., & Parker, K. K. (2008). Sarcomere Alignment Is Regulated by Myocyte Shape. *Cell Motility and the Cytoskeleton*, 65(8), 641-651. doi:10.1002/cm.20290
- Breckwoldt, K., Letuffe-Breniere, D., Mannhardt, I., Schulze, T., Ulmer, B., Werner, T., . . . Hansen, A. (2017). Differentiation of Cardiomyocytes and Generation of Human Engineered Heart Tissue. *Nat Protoc*, 12(6), 1177-1197. doi:10.1038/nprot.2017.033
- Brookhouser, N., Tekel, S. J., Standage-Beier, K., Nguyen, T., Schwarz, G., Wang, X., & Brafman, D. A. (2019). Big-Tree: Base-Edited Isogenic Hpsc Line Generation Using a Transient Reporter for Editing Enrichment. *Stem Cell Reports*, 14, 184-191.
- Brooks, W. W., & Conrad, C. H. (2009). Isoproterenol-Induced Myocardial Injury and Diastolic Dysfunction in Mice: Structural and Functional Correlates. *Comp Med*, 59(4), 339-343.
- Cahill, T. J., Ashrafian, H., & Watkins, H. (2013). Genetic Cardiomyopathies Causing Heart Failure. *Circ Res*, 113(6), 660-675. doi:10.1161/CIRCRESAHA.113.300282
- Camelliti, P., Borg, T. K., & Kohl, P. (2005). Structural and Functional Characterisation of Cardiac Fibroblasts. *Cardiovasc Res*, 65(1), 40-51. doi:10.1016/j.cardiores.2004.08.020
- Carmeliet, E. (1999). Cardiac Ionic Currents and Acute Ischemia: From Channels to Arrhythmias. *Physiol Rev*, 79(3), 917-1017. doi:10.1152/physrev.1999.79.3.917
- Carrier, L., Bonne, G., Bahrend, E., Yu, B., Richard, P., Niel, F., . . . Schwartz, K. (1997). Organization and Sequence of Human Cardiac Myosin Binding Protein C Gene

- (Mybpc3) and Identification of Mutations Predicted to Produce Truncated Proteins in Familial Hypertrophic Cardiomyopathy. *Circ Res*, 80(3), 427-434.
- Casals, G., Ros, J., Sionis, A., Davidson, M. M., Morales-Ruiz, M., & Jimenez, W. (2009). Hypoxia Induces B-Type Natriuretic Peptide Release in Cell Lines Derived from Human Cardiomyocytes. *Am J Physiol Heart Circ Physiol*, 297(2), H550-555. doi:10.1152/ajpheart.00250.2009
- Chandra, R., Starmer, C. F., & Grant, A. O. (1998). Multiple Effects of Kpq Deletion Mutation on Gating of Human Cardiac Na⁺ Channels Expressed in Mammalian Cells. *Am J Physiol*, 274(5), H1643-1654. doi:10.1152/ajpheart.1998.274.5.H1643
- Chattergoon, N. N., Giraud, G. D., Louey, S., Stork, P., Fowden, A. L., & Thornburg, K. L. (2012). Thyroid Hormone Drives Fetal Cardiomyocyte Maturation. *FASEB J*, 26(1), 397-408. doi:10.1096/fj.10-179895
- Chen, T., & Vunjak-Novakovic, G. (2019). Human Tissue-Engineered Model of Myocardial Ischemia-Reperfusion Injury. *Tissue Eng Part A*, 25(9-10), 711-724. doi:10.1089/ten.TEA.2018.0212
- Chi, N. C., & Karliner, J. S. (2004). Molecular Determinants of Responses to Myocardial Ischemia/Reperfusion Injury: Focus on Hypoxia-Inducible and Heat Shock Factors. *Cardiovasc Res*, 61(3), 437-447. doi:10.1016/j.cardiores.2003.11.033
- Chiu, L. L., Janic, K., & Radisic, M. (2012). Engineering of Oriented Myocardium on Three-Dimensional Micropatterned Collagen-Chitosan Hydrogel. *Int J Artif Organs*, 35(4), 237-250. doi:10.5301/ijao.5000084
- Chiu, L. L. Y., & Radisic, M. (2013). Cardiac Tissue Engineering. *Current Opinion in Chemical Engineering*, 2(1), 41-52. doi:10.1016/j.coche.2013.01.002
- Christdi E., H. H., Brunham L. (2018). Crispr/Cas9-Mediated Genome Editing in Human Stem Cell-Derived Cardiomyocytes: Applications for Cardiovascular Disease Modelling and Cardiotoxicity Screening. *Drug Discovery Today: Technologies*, 28.
- Coles, J. G., Boscarino, C., Takahashi, M., Grant, D., Chang, A., Ritter, J., . . . Hannigan, G. (2005). Cardioprotective Stress Response in the Human Fetal Heart. *J Thorac Cardiovasc Surg*, 129(5), 1128-1136. doi:10.1016/j.jtcvs.2004.11.055
- Cong, L., Ran, F. A., Cox, D., Lin, S., Barretto, R., Habib, N., . . . Zhang, F. (2013). Multiplex Genome Engineering Using Crispr/Cas Systems. *Science*, 339(6121), 819-823. doi:10.1126/science.1231143

- Crossman, D. C. (2004). The Pathophysiology of Myocardial Ischemia. *Heart*, 90(5), 576-580.
- Cutts, J., Nikkhah, M., & Brafman, D. A. (2015). Biomaterial Approaches for Stem Cell-Based Myocardial Tissue Engineering. *Biomark Insights*, 10(Suppl 1), 77-90. doi:10.4137/BMI.S20313
- D., R. (2008). Long-Qt Syndrome. *N Engl J Med*, 358, 169-176.
- Delisle, B. P., Anderson, C. L., Balijepalli, R. C., Anson, B. D., Kamp, T. J., & January, C. T. (2003). Thapsigargin Selectively Rescues the Trafficking Defective Lqt2 Channels G601s and F805c. *J Biol Chem*, 278(37), 35749-35754. doi:10.1074/jbc.M305787200
- Delisle, B. P., Anson, B. D., Rajamani, S., & January, C. T. (2004). Biology of Cardiac Arrhythmias: Ion Channel Protein Trafficking. *Circ Res*, 94(11), 1418-1428. doi:10.1161/01.RES.0000128561.28701.ea
- Denning, C., Borgdorff, V., Crutchley, J., Firth, K. S., George, V., Kalra, S., . . . Young, L. E. (2016). Cardiomyocytes from Human Pluripotent Stem Cells: From Laboratory Curiosity to Industrial Biomedical Platform. *Biochim Biophys Acta*, 1863(7 Pt B), 1728-1748. doi:10.1016/j.bbamcr.2015.10.014
- Derangeon, M., Montnach, J., Baro, I., & F., C. (2012). Mouse Models of Scn5a-Related Cardiac Arrhythmias. *Frontiers in Physiology*, 3.
- Dubois, N. C., Craft, A. M., Sharma, P., Elliott, D. A., Stanley, E. G., Elefanty, A. G., . . . Keller, G. (2011). Sirpa Is a Specific Cell-Surface Marker for Isolating Cardiomyocytes Derived from Human Pluripotent Stem Cells. *Nature Biotechnology*, 29(11), 1011-U1082. doi:10.1038/nbt.2005
- Duncan, G., Firth, K., George, V., Hoang, M. D., Staniforth, A., Smith, G., & Denning, C. (2017). Drug-Mediated Shortening of Action Potentials in Lqts2 Human Induced Pluripotent Stem Cell-Derived Cardiomyocytes. *Stem Cells Dev*, 26(23), 1695-1705. doi:10.1089/scd.2017.0172
- Duncker, D. J., Bakkers, J., Brundel, B. J., Robbins, J., Tardiff, J. C., & Carrier, L. (2015). Animal and in Silico Models for the Study of Sarcomeric Cardiomyopathies. *Cardiovasc Res*, 105(4), 439-448. doi:10.1093/cvr/cvv006
- Eagle, H., & Levine, E. M. (1967). Growth Regulatory Effects of Cellular Interaction. *Nature*, 1102-1106.

- Eid, A., Alshareef, S., & Mahfouz, M. M. (2018). Crispr Base Editors: Genome Editing without Double-Stranded Breaks. *Biochemical Journal*, 475, 1955-1964.
- Ellis, B. W., Acun, A., Can, U. I., & Zorlutuna, P. (2017). Human Ipsc-Derived Myocardium-on-Chip with Capillary-Like Flow for Personalized Medicine. *Biomicrofluidics*, 11(2), 024105. doi:10.1063/1.4978468
- Elson, E. L., Qian, H., Fee, J. A., & Wakatsuki, T. (2019). A Model for Positive Feedback Control of the Transformation of Fibroblasts to Myofibroblasts. *Prog Biophys Mol Biol*, 144, 30-40. doi:10.1016/j.pbiomolbio.2018.08.004
- Engelmayr, G. C., Jr., Cheng, M., Bettinger, C. J., Borenstein, J. T., Langer, R., & Freed, L. E. (2008). Accordion-Like Honeycombs for Tissue Engineering of Cardiac Anisotropy. *Nat Mater*, 7(12), 1003-1010. doi:10.1038/nmat2316
- Esmaeili, H., Patino-Guerrero, A., Hasany, M., Ansari, M. O., Memic, A., Dolatshahi-Pirouz, A., & Nikkhah, M. (2021). Electroconductive Biomaterials for Cardiac Tissue Engineering. *Acta Biomater*. doi:10.1016/j.actbio.2021.08.031
- Feinberg, A. W., Alford, P. W., Jin, H., Ripplinger, C. M., Werdich, A. A., Sheehy, S. P., . . . Parker, K. K. (2012). Controlling the Contractile Strength of Engineered Cardiac Muscle by Hierarchical Tissue Architecture. *Biomaterials*, 33(23), 5732-5741. doi:10.1016/j.biomaterials.2012.04.043
- Ficker, E., Thomas, D., Viswanathan, P. C., Dennis, A. T., Priori, S. G., Napolitano, C., . . . Brown, A. M. (2000). Novel Characteristics of a Mispromoted Mutant Herg Channel Linked to Hereditary Long Qt Syndrome. *Am J Physiol Heart Circ Physiol*, 279(4), H1748-1756. doi:10.1152/ajpheart.2000.279.4.H1748
- Francis Stuart, S. D., De Jesus, N. M., Lindsey, M. L., & Ripplinger, C. M. (2016). The Crossroads of Inflammation, Fibrosis, and Arrhythmia Following Myocardial Infarction. *J Mol Cell Cardiol*, 91, 114-122. doi:10.1016/j.yjmcc.2015.12.024
- Frank, A., Bonney, M., Bonney, S., Weitzel, L., Koeppen, M., & Eckle, T. (2012). Myocardial Ischemia Reperfusion Injury: From Basic Science to Clinical Bedside. *Semin Cardiothorac Vasc Anesth*, 16(3), 123-132. doi:10.1177/1089253211436350
- Friedrichs, S., Malan, D., & Sasse, P. (2013). Modeling Long Qt Syndromes Using Induced Pluripotent Stem Cells: Current Progress and Future Challenges. *Trends in Cardiovascular Medicine*, 23, 91-98.

- Fulop, N., Mason, M. M., Dutta, K., Wang, P., Davidoff, A. J., Marchase, R. B., & Chatham, J. C. (2007). Impact of Type 2 Diabetes and Aging on Cardiomyocyte Function and O-Linked N-Acetylglucosamine Levels in the Heart. *Am J Physiol Cell Physiol*, 292(4), C1370-1378. doi:10.1152/ajpcell.00422.2006
- Gao, X. M., Dart, A. M., Dewar, E., Jennings, G., & Du, X. J. (2000). Serial Echocardiographic Assessment of Left Ventricular Dimensions and Function after Myocardial Infarction in Mice. *Cardiovasc Res*, 45(2), 330-338.
- Garg, P., Oikonomopoulos, A., Chen, H., Li, Y., Lam, C. K., Sallam, K., . . . Wu, J. C. (2018). Genome Editing of Induced Pluripotent Stem Cells to Decipher Cardiac Channelopathy Variant. *J Am Coll Cardiol*, 72(1), 62-75. doi:10.1016/j.jacc.2018.04.041
- Ghiaseddin, A., Pouri, H., Soleimani, M., Vasheghani-Farahani, E., Ahmadi Tafti, H., & Hashemi-Najafabadi, S. (2017). Cell Laden Hydrogel Construct on-a-Chip for Mimicry of Cardiac Tissue in-Vitro Study. *Biochem Biophys Res Commun*, 484(2), 225-230. doi:10.1016/j.bbrc.2017.01.029
- Ghuran, A. V., & Camm, A. J. (2001). Ischaemic Heart Disease Presenting as Arrhythmias. *Br Med Bull*, 59, 193-210.
- Gong, Q., Anderson, C. L., January, C. T., & Zhou, Z. (2004). Pharmacological Rescue of Trafficking Defective Herg Channels Formed by Co-Assembly of Wild-Type and Long Qt Mutant N470d Subunits. *Am J Physiol Heart Circ Physiol*, 287, H652-H658.
- Graham, R. M., Frazier, D. P., Thompson, J. W., Haliko, S., Li, H., Wasserlauf, B. J., . . . Webster, K. A. (2004). A Unique Pathway of Cardiac Myocyte Death Caused by Hypoxia-Acidosis. *J Exp Biol*, 207(Pt 18), 3189-3200. doi:10.1242/jeb.01109
- Grandi, E., Pandit, S. V., Voigt, N., Workman, A. J., Dobrev, D., Jalife, J., & Bers, D. M. (2011). Human Atrial Action Potential and Ca²⁺ Model: Sinus Rhythm and Chronic Atrial Fibrillation. *Circ Res*, 109(9), 1055-1066. doi:10.1161/CIRCRESAHA.111.253955
- Grosberg, A., Alford, P. W., McCain, M. L., & Parker, K. K. (2011). Ensembles of Engineered Cardiac Tissues for Physiological and Pharmacological Study: Heart on a Chip. *Lab Chip*, 11(24), 4165-4173. doi:10.1039/c1lc20557a
- Grosberg, A., Nesmith, A. P., Goss, J. A., Brigham, M. D., McCain, M. L., & Parker, K. K. (2012). Muscle on a Chip: In Vitro Contractility Assays for Smooth and Striated

- Muscle. *J Pharmacol Toxicol Methods*, 65(3), 126-135. doi:10.1016/j.vascn.2012.04.001
- Guo, L., Abrams, R. M., Babiarz, J. E., Cohen, J. D., Kameoka, S., Sanders, M. J., . . . Kolaja, K. L. (2011). Estimating the Risk of Drug-Induced Proarrhythmia Using Human Induced Pluripotent Stem Cell-Derived Cardiomyocytes. *Toxicol Sci*, 123(1), 281-289. doi:10.1093/toxsci/kfr158
- Guyette, J. P., Charest, J. M., Mills, R. W., Jank, B. J., Moser, P. T., Gilpin, S. E., . . . Ott, H. C. (2016). Bioengineering Human Myocardium on Native Extracellular Matrix. *Circ Res*, 118(1), 56-72. doi:10.1161/CIRCRESAHA.115.306874
- Hackam, D. G., & Redelmeier, D. A. (2006). Translation of Research Evidence from Animals to Humans. *JAMA*, 296(14), 1731-1732. doi:10.1001/jama.296.14.1731
- Harris, K., Aylott, M., Cui, Y., Louttit, J. B., McMahon, N. C., & Sridhar, A. (2013). Comparison of Electrophysiological Data from Human-Induced Pluripotent Stem Cell-Derived Cardiomyocytes to Functional Preclinical Safety Assays. *Toxicol Sci*, 134(2), 412-426. doi:10.1093/toxsci/kft113
- He, J., Ma, C., Liu, W., & Wang, J. (2014). On-Chip Monitoring of Skeletal Myoblast Transplantation for the Treatment of Hypoxia-Induced Myocardial Injury. *Analyst*, 139(18), 4482-4490. doi:10.1039/c4an00697f
- Heidenreich, P. A., Trogon, J. G., Khavjou, O. A., Butler, J., Dracup, K., Ezekowitz, M. D., . . . Outcomes, R. (2011). Forecasting the Future of Cardiovascular Disease in the United States: A Policy Statement from the American Heart Association. *Circulation*, 123(8), 933-944. doi:10.1161/CIR.0b013e31820a55f5
- Herron, T. J., Rocha, A. M., Campbell, K. F., Ponce-Balbuena, D., Willis, B. C., Guerrero-Serna, G., . . . Jalife, J. (2016). Extracellular Matrix-Mediated Maturation of Human Pluripotent Stem Cell-Derived Cardiac Monolayer Structure and Electrophysiological Function. *Circ Arrhythm Electrophysiol*, 9(4), e003638. doi:10.1161/CIRCEP.113.003638
- Hidalgo, A., Glass, N., Ovchinnikov, D., Yang, S., Zhang, X., Mazzone, S., . . . Cooper-White, J. (2018). Modelling Ischemia-Reperfusion Injury (Iri) in Vitro Using Metabolically Matured Induced Pluripotent Stem Cell-Derived Cardiomyocytes. *APL Bioeng*, 2(2), 026102.
- Hinson, J. T., Chopra, A., Nafissi, N., Polacheck, W. J., Benson, C. C., Swist, S., . . . Seidman, C. E. (2015). Titin Mutations in Ips Cells Define Sarcomere Insufficiency

- as a Cause of Dilated Cardiomyopathy. *Science*, 349(6251), 982-986. doi:10.1126/science.aaa5458
- Hofker, M. H., van Vlijmen, B. J., & Havekes, L. M. (1998). Transgenic Mouse Models to Study the Role of Apoe in Hyperlipidemia and Atherosclerosis. *Atherosclerosis*, 137(1), 1-11.
- Horiuchi, K., Amizuka, N., Takeshita, S., Takamatsu, H., Katsuura, M., Ozawa, H., . . . Kudo, A. (1999). Identification and Characterization of a Novel Protein, Periostin, with Restricted Expression to Periosteum and Periodontal Ligament and Increased Expression by Transforming Growth Factor Beta. *J Bone Miner Res*, 14(7), 1239-1249. doi:10.1359/jbmr.1999.14.7.1239
- Horton, R. E., Yadid, M., McCain, M. L., Sheehy, S. P., Pasqualini, F. S., Park, S. J., . . . Parker, K. K. (2016). Angiotensin Ii Induced Cardiac Dysfunction on a Chip. *PLoS One*, 11(1), e0146415. doi:10.1371/journal.pone.0146415
- Horvath, P., & Barrangou, R. (2010). Crispr/Cas, the Immune System of Bacteria and Archaea. *Science*, 327(5962), 167-170. doi:10.1126/science.1179555
- Huang, C. P., Lu, J., Seon, H., Lee, A. P., Flanagan, L. A., Kim, H. Y., . . . Jeon, N. L. (2009). Engineering Microscale Cellular Niches for Three-Dimensional Multicellular Co-Cultures. *Lab Chip*, 9(12), 1740-1748. doi:10.1039/b818401a
- Huang, H. P., Chen, P. H., Hwu, W. L., Chuang, C. Y., Chien, Y. H., Stone, L., . . . Kuo, H. C. (2011). Human Pompe Disease-Induced Pluripotent Stem Cells for Pathogenesis Modeling, Drug Testing and Disease Marker Identification. *Hum Mol Genet*, 20(24), 4851-4864. doi:10.1093/hmg/ddr424
- Hubbi, M. E., Kshitiz, Gilkes, D. M., Rey, S., Wong, C. C., Luo, W., . . . Semenza, G. L. (2013). A Nontranscriptional Role for Hif-1 α as a Direct Inhibitor of DNA Replication. *Science Signaling*, 6(262), ra10.
- Itzhaki, I., Maizels, L., Huber, I., Zwi-Dantsis, L., Caspi, O., Winterstern, A., . . . Gepstein, L. (2011). Modelling the Long Qt Syndrome with Induced Pluripotent Stem Cells. *Nature*, 471.
- Ivashchenko, C. Y., Pipes, G. C., Lozinskaya, I. M., Lin, Z., Xiaoping, X., Needle, S., . . . Willette, R. N. (2013). Human-Induced Pluripotent Stem Cell-Derived Cardiomyocytes Exhibit Temporal Changes in Phenotype. *Am J Physiol Heart Circ Physiol*, 305(6), H913-922. doi:10.1152/ajpheart.00819.2012

- Jaalouk, D. E., & Lammerding, J. (2009). Mechanotransduction Gone Awry. *Nat Rev Mol Cell Biol*, 10(1), 63-73. doi:10.1038/nrm2597
- Jackman, C. P., Carlson, A. L., & Bursac, N. (2016). Dynamic Culture Yields Engineered Myocardium with near-Adult Functional Output. *Biomaterials*, 111, 66-79. doi:10.1016/j.biomaterials.2016.09.024
- Jennings, R. B., Reimer, K. A., & Steenbergen, C. (1986). Myocardial Ischemia Revisited. The Osmolar Load, Membrane Damage, and Reperfusion. *J Mol Cell Cardiol*, 18(8), 769-780. doi:10.1016/s0022-2828(86)80952-x
- Jiang, Y., Park, P., Hong, S. M., & Ban, K. (2018). Maturation of Cardiomyocytes Derived from Human Pluripotent Stem Cells: Current Strategies and Limitations. *Mol Cells*, 41(7), 613-621. doi:10.14348/molcells.2018.0143
- Johnson, R. D., & Camelliti, P. (2018). Role of Non-Myocyte Gap Junctions and Connexin Hemichannels in Cardiovascular Health and Disease: Novel Therapeutic Targets? *Int J Mol Sci*, 19(3), 866. doi:10.3390/ijms19030866
- Kagan, A., Yu, Z., Fishman, G. I., & McDonald, T. V. (2000). The Dominant Negative Lqt2 Mutation A561v Reduces Wild-Type Herg Expression. *J Biol Chem*, 275(15), 11241-11248. doi:10.1074/jbc.275.15.11241
- Kalogeris, T., Baines, C. P., Krenz, M., & Korthuis, R. J. (2012). Cell Biology of Ischemia/Reperfusion Injury. *Int Rev Cell Mol Biol*, 298, 229-317. doi:10.1016/B978-0-12-394309-5.00006-7
- Kapplinger, J. D., Tester, D. J., Salisbury, B. A., Carr, J. L., Harris-Kerr, C., Pollevick, G. D., . . . Ackerman, M. J. (2009). Spectrum and Prevalence of Mutations from the First 2,500 Consecutive Unrelated Patients Referred for the Familial Long Qt Syndrome Genetic Test. *Heart Rhythm*, 6(9), 1297-1303. doi:10.1016/j.hrthm.2009.05.021
- Katare, R. G., Ando, M., Kakinuma, Y., & Sato, T. (2010). Engineered Heart Tissue: A Novel Tool to Study the Ischemic Changes of the Heart in Vitro. *PLoS One*, 5(2), e9275. doi:10.1371/journal.pone.0009275
- Katz, A. M. (1973). Effects of Ischemia on the Contractile Processes of Heart Muscle. *Am J Cardiol*, 32(4), 456-460. doi:10.1016/s0002-9149(73)80036-0
- Kharaziha, M., Nikkhah, M., Shin, S. R., Annabi, N., Masoumi, N., Gaharwar, A. K., . . . Khademhosseini, A. (2013). Pgs:Gelatin Nanofibrous Scaffolds with Tunable

- Mechanical and Structural Properties for Engineering Cardiac Tissues. *Biomaterials*, 34(27), 6355-6366. doi:10.1016/j.biomaterials.2013.04.045
- Kharaziha, M. S., S.; Nikkhah, M.; Topkaya, S. N. ; Masoumi, N.; Dokmeci, M. R. ; Khademhosseini, A. (2014). Tough and Flexible Cnt–Polymeric Hybrid Scaffolds for Engineering Cardiac Constructs. *Biomaterials*, 34, 7346-7354.
- Khavjou, O., Phelps, D., Leib, A. (2016). *Projections of Cardiovascular Disease Prevalence and Costs: 2015–2035*.
- Kim, C., Majdi, M., Xia, P., Wei, K. A., Talantova, M., Spiering, S., . . . Chen, H. S. (2010). Non-Cardiomyocytes Influence the Electrophysiological Maturation of Human Embryonic Stem Cell-Derived Cardiomyocytes During Differentiation. *Stem Cells Dev*, 19(6), 783-795. doi:10.1089/scd.2009.0349
- Kim, S. B., Bae, H., Cha, J. M., Moon, S. J., Cokmeci, M. R., Croek, D. M., & Khademhosseini, A. (2011). A Cell-Based Biosensor for Real-Time Detection of Cardiotoxicity Using Lensfree Imaging. *Lab Chip*, 11(10), 1801-1807.
- Koshiji, M., To, K. K. W., Hammer, S., Kumamoto, K., Harris, A. L., Modrich, P., & Huang, L. E. (2005). Hif-1 α Induces Genetic Instability by Transcriptionally Downregulating Muts α Expression. *Molecular Cell*, 17, 793-803.
- Kothapalli, C. R., & Honarmandi, P. (2014). Theoretical and Experimental Quantification of the Role of Diffusive Chemogradients on Neuritogenesis within Three-Dimensional Collagen Scaffolds. *Acta Biomater*, 10(8), 3664-3674. doi:10.1016/j.actbio.2014.05.009
- Kukovetz, W. R., Holzmann, S., & Poch, G. (1992). Molecular Mechanism of Action of Nicorandil. *J Cardiovasc Pharmacol*, 20 Suppl 3, S1-7. doi:10.1097/00005344-199206203-00002
- Kumar, M., Kasala, E. R., Bodduluru, L. N., Dahiya, V., Sharma, D., Kumar, V., & Lahkar, M. (2016). Animal Models of Myocardial Infarction: Mainstay in Clinical Translation. *Regul Toxicol Pharmacol*, 76, 221-230. doi:10.1016/j.yrtph.2016.03.005
- Kuusela, J., Kujala, V. J., Kiviäho, A., Ojala, M., Swan, H., Kontula, K., & Aalto-Setälä, K. (2016). Effects of Cardioactive Drugs on Human Induced Pluripotent Stem Cell Derived Long Qt Syndrome Cardiomyocytes. *Springerplus*, 5, 234. doi:10.1186/s40064-016-1889-y

- Laco, F., Woo, T. L., Zhong, Q., Szmyd, R., Ting, S., Khan, F. J., . . . Oh, S. (2018). Unraveling the Inconsistencies of Cardiac Differentiation Efficiency Induced by the Gsk3beta Inhibitor Chir99021 in Human Pluripotent Stem Cells. *Stem Cell Reports*, 10(6), 1851-1866. doi:10.1016/j.stemcr.2018.03.023
- Laflamme, M. A., & Murry, C. E. (2011). Heart Regeneration. *Nature*, 473(7347), 326-335. doi:10.1038/nature10147
- Lahti, A. L., Kujala, V. J., Chapman, H., Koivisto, A., Pekkanen-Mattila, M., Kerkela, E., . . . Aalto-Setälä, K. (2012). Model for Long Qt Syndrome Type 2 Using Human Ips Cells Demonstrates Arrhythmogenic Characteristics in Cell Culture. *Disease Models and Mechanisms*, 5, 220-230.
- Landry, N. M., Cohen, S., & Dixon, I. M. C. (2018). Periostin in Cardiovascular Disease and Development: A Tale of Two Distinct Roles. *Basic Res Cardiol*, 113(1), 1. doi:10.1007/s00395-017-0659-5
- Lee, J., Razu, M. E., Wang, X., Lacerda, C., & Kim, J. J. (2015). Biomimetic Cardiac Microsystems for Pathophysiological Studies and Drug Screens. *J Lab Autom*, 20(2), 96-106. doi:10.1177/2211068214560903
- Leenen, F. H., Skarda, V., Yuan, B., & White, R. (1999). Changes in Cardiac Ang II Postmyocardial Infarction in Rats: Effects of Nephrectomy and Ace Inhibitors. *Am J Physiol*, 276(1), H317-325. doi:10.1152/ajpheart.1999.276.1.H317
- Leung, B. M., & Sefton, M. V. (2010). A Modular Approach to Cardiac Tissue Engineering. *Tissue Eng Part A*, 16(10), 3207-3218. doi:10.1089/ten.TEA.2009.0746
- Li, M., Wu, J., Hu, G., Song, Y., Shen, J., Xin, J., . . . Xiao, H. (2020). Pathological Matrix Stiffness Promotes Cardiac Fibroblast Differentiation through the Pou2f1 Signaling Pathway. *Science China Life Sciences*, 64, 242-254.
- Lian, X., Zhang, J., Azarin, S. M., Zhu, K., Hazeltine, L. B., Bao, X., . . . Palecek, S. P. (2013). Directed Cardiomyocyte Differentiation from Human Pluripotent Stem Cells by Modulating Wnt/Beta-Catenin Signaling under Fully Defined Conditions. *Nat Protoc*, 8(1), 162-175. doi:10.1038/nprot.2012.150
- Liang, P., Sallam, K., Wu, H., Li, Y., Itzhaki, I., Garg, P., . . . Wu, J. C. (2016). Patient-Specific and Genome-Edited Induced Pluripotent Stem Cell-Derived Cardiomyocytes Elucidate Single-Cell Phenotype of Brugada Syndrome. *J Am Coll Cardiol*, 68(19), 2086-2096. doi:10.1016/j.jacc.2016.07.779

- Liu, G., Ma, C., Yang, H., & Zhang, P. Y. (2017). Transforming Growth Factor B and Its Role in Heart Disease. *Exp Ther Med*, 13(5), 2123-2128.
- Liu, H., Bolonduro, O. A., Hu, N., Ju, J., Rao, A. A., Duffy, B. M., . . . Timko, B. P. (2020). Heart-on-a-Chip Model with Integrated Extra- and Intracellular Bioelectronics for Monitoring Cardiac Electrophysiology under Acute Hypoxia. *Nano Lett*, 20(4), 2585-2593. doi:10.1021/acs.nanolett.0c00076
- Liu, Y. B., Wu, C. C., Lu, L. S., Su, M. J., Lin, C. W., Lin, S. F., . . . Lee, Y. T. (2003). Sympathetic Nerve Sprouting, Electrical Remodeling, and Increased Vulnerability to Ventricular Fibrillation in Hypercholesterolemic Rabbits. *Circ Res*, 92(10), 1145-1152. doi:10.1161/01.RES.0000072999.51484.92
- Lu, L., Liu, M., Sun, R., Zheng, Y., & Zhang, P. (2015). Myocardial Infarction: Symptoms and Treatments. *Cell Biochem Biophys*, 72(3), 865-867. doi:10.1007/s12013-015-0553-4
- Lundy, S. D., Zhu, W. Z., Regnier, M., & Laflamme, M. A. (2013). Structural and Functional Maturation of Cardiomyocytes Derived from Human Pluripotent Stem Cells. *Stem Cells Dev*, 22(14), 1991-2002. doi:10.1089/scd.2012.0490
- Ma, Z., Huebsch, N., Koo, S., Mandegar, M. A., Siemons, B., Boggess, S., . . . Healy, K. E. (2018). Contractile Deficits in Engineered Cardiac Microtissues as a Result of Mybpc3 Deficiency and Mechanical Overload. *Nature Biomedical Engineering*, 2(12), 955-967. doi:10.1038/s41551-018-0280-4
- MacKenna, D., Summerour, S. R., & Villarreal, F. J. (2000). Role of Mechanical Factors in Modulating Cardiac Fibroblast Function and Extracellular Matrix Synthesis. *Cardiovasc Res*, 46(2), 257-263. doi:10.1016/s0008-6363(00)00030-4
- Mannhardt, I., Breckwoldt, K., Letuffe-Breniere, D., Schaaf, S., Schulz, H., Neuber, C., . . . Hansen, A. (2016). Human Engineered Heart Tissue: Analysis of Contractile Force. *Stem Cell Reports*, 7(1), 29-42. doi:10.1016/j.stemcr.2016.04.011
- Martherus, R. S., Vanherle, S. J., Timmer, E. D., Zeijlemaker, V. A., Broers, J. L., Smeets, H. J., . . . Ayoubi, T. A. (2010). Electrical Signals Affect the Cardiomyocyte Transcriptome Independently of Contraction. *Physiol Genomics*, 42A(4), 283-289. doi:10.1152/physiolgenomics.00182.2009
- Mastikhina, O., Moon, B., Williams, K., Hatkar, R., Gustafson, D., Mourad, O., . . . Nunes, S. S. (2019). Human Cardiac Fibrosis-on-a-Chip Model Recapitulates Disease Hallmarks and Can Serve as a Platform for Drug Testing. *Biomaterials*, 233.

- Mathur, A., Loskill, P., Hong, S., Lee, J., Marcus, S. G., Dumont, L., . . . Healy, K. E. (2013). Human Induced Pluripotent Stem Cell-Based Microphysiological Tissue Models of Myocardium and Liver for Drug Development. *Stem Cell Res Ther*, 4 Suppl 1, S14. doi:10.1186/scrt375
- Mathur, A., Loskill, P., Shao, K., Huebsch, N., Hong, S., Marcus, S. G., . . . Healy, K. E. (2015). Human Ipsc-Based Cardiac Microphysiological System for Drug Screening Applications. *Sci Rep*, 5, 8883. doi:10.1038/srep08883
- Matsa, E., Rajamohan, D., Dick, E., Young, L., Mellor, I., Staniforth, A., & Denning, C. (2011). Drug Evaluation in Cardiomyocytes Derived from Human Induced Pluripotent Stem Cells Carrying a Long Qt Syndrome Type 2 Mutation. *Eur Heart J*, 32(8), 952-962. doi:10.1093/eurheartj/ehr073
- McBride, C. M., Smith, A. M., Smith, J. L., Reloj, A. R., Velasco, E. J., Powell, J., . . . Delisle, B. P. (2013). Mechanistic Basis for Type 2 Long Qt Syndrome Caused by Kcnh2 Mutations That Disrupt Conserved Arginine Residue in the Voltage Sensor. *J Membr Biol*, 246, 355-364.
- McCain, M. L., Sheehy, S. P., Grosberg, A., Goss, J. A., & Parker, K. K. (2013). Recapitulating Maladaptive, Multiscale Remodeling of Failing Myocardium on a Chip. *Proc Natl Acad Sci U S A*, 110(24), 9770-9775. doi:10.1073/pnas.1304913110
- McCauley, M. D., & Wehrens, X. H. (2009). Animal Models of Arrhythmogenic Cardiomyopathy. *Dis Model Mech*, 2(11-12), 563-570. doi:10.1242/dmm.002840
- McLerie, M. (2003). Dominant-Negative Suppression of Ik1 in the Mouse Heart Leads to Altered Cardiac Excitability. *Journal of Molecular and Cellular Cardiology*, 35(4), 367-378. doi:10.1016/s0022-2828(03)00014-2
- Mehta, A., Sequiera, G. L., Ramachandra, C. J., Sudiby, Y., Chung, Y., Sheng, J., . . . Shim, W. (2014). Re-Trafficking of Herg Reverses Long Qt Syndrome 2 Phenotype in Human Ips-Derived Cardiomyocytes. *Cardiovasc Res*, 102(3), 497-506. doi:10.1093/cvr/cvu060
- Mesquita, F. C. P., Arantes, P. C., Kasai-Brunswick, T. H., Araujo, D. S., Gubert, F., Monnerat, G., . . . Carvalho, A. B. (2019). R534c Mutation in Herg Causes a Trafficking Defect in Ipsc-Derived Cardiomyocytes from Patients with Type 2 Long Qt Syndrome. *Sci Rep*, 9(1), 19203. doi:10.1038/s41598-019-55837-w

- Moretti, A., Bellin, M., Welling, A., Jung, C. B., Lam, J. T., Bott-Flugel, L., . . . Laugwitz, K. L. (2010). Patient-Specific Induced Pluripotent Stem-Cell Models for Long-Qt Syndrome. *N Engl J Med*, 363(15), 1397-1409. doi:10.1056/NEJMoa0908679
- Morita, E., Yasue, H., Yoshimura, M., Ogawa, H., Jougasaki, M., Matsumura, T., . . . Nakao, K. (1993). Increased Plasma Levels of Brain Natriuretic Peptide in Patients with Acute Myocardial Infarction. *Circulation*, 88(1), 82-91. doi:10.1161/01.cir.88.1.82
- Mosadegh, B., Dabiri, B. E., Lockett, M. R., Derda, R., Campbell, P., Parker, K. K., & Whitesides, G. M. (2014). Three-Dimensional Paper-Based Model for Cardiac Ischemia. *Adv Healthc Mater*, 3(7), 1036-1043. doi:10.1002/adhm.201300575
- Mosqueira, D., Mannhardt, I., Bhagwan, J. R., Lis-Slimak, K., Katili, P., Scott, E., . . . Denning, C. (2018). Crispr/Cas9 Editing in Human Pluripotent Stem Cell-Cardiomyocytes Highlights Arrhythmias, Hypocontractility, and Energy Depletion as Potential Therapeutic Targets for Hypertrophic Cardiomyopathy. *Eur Heart J*, 39(43), 3879-3892. doi:10.1093/eurheartj/ehy249
- Moss A., S. W., Wilde A., Towbin J., Zareba W., Robinson J., Qi M., Vincent G., Ackerman M., Kaufman E., Hofman N., Seth R., Kamakura S., Miyamoto Y., Goldenberg I., Andrews M., McNitt S. (2007). Clinical Aspects of Type-1 Long-Qt Syndrome by Location, Coding Type, and Biophysical Function of Mutations Involving the Kcnq1 Gene. *Circulation*.
- Mura, M., Mehta, A., Ramachandra, C. J., Zappatore, R., Pisano, F., Ciuffreda, M. C., . . . Gneccchi, M. (2017). The Kcnh2-Ivs9-28a/G Mutation Causes Aberrant Isoform Expression and Herg Trafficking Defect in Cardiomyocytes Derived from Patients Affected by Long Qt Syndrome Type 2. *Int J Cardiol*, 240, 367-371. doi:10.1016/j.ijcard.2017.04.038
- Nag, A. C. (1980). Study of Non-Muscle Cells of the Adult Mammalian Heart: A Fine Structural Analysis and Distribution. *Cytobios*, 28(109), 41-61.
- Nagaraju, S., Truong, D., Mouneimne, G., & Nikkhah, M. (2018). Microfluidic Tumor-Vascular Model to Study Breast Cancer Cell Invasion and Intravasation. *Adv Healthc Mater*, 7(9), e1701257.
- Navaei, A., Moore, N., Sullivan, R. T., Truong, D., Migrino, R. Q., & Nikkhah, M. (2017). Electrically Conductive Hydrogel-Based Micro-Topographies for the Development of Organized Cardiac Tissues. *Rsc Advances*, 7(6), 3302-3312. doi:10.1039/c6ra26279a

- Navaei, A., Rahmani Eliato, K., Ros, R., Migrino, R. Q., Willis, B. C., & Nikkhah, M. (2019). The Influence of Electrically Conductive and Non-Conductive Nanocomposite Scaffolds on the Maturation and Excitability of Engineered Cardiac Tissues. *Biomater Sci*, 7(2), 585-595. doi:10.1039/c8bm01050a
- Navaei, A., Saini, H., Christenson, W., Sullivan, R. T., Ros, R., & Nikkhah, M. (2016). Gold Nanorod-Incorporated Gelatin-Based Conductive Hydrogels for Engineering Cardiac Tissue Constructs. *Acta Biomater*, 41, 133-146. doi:10.1016/j.actbio.2016.05.027
- Navaei, A., Truong, D., Heffernan, J., Cutts, J., Brafman, D., Sirianni, R. W., . . . Nikkhah, M. (2016). Pnipaam-Based Biohybrid Injectable Hydrogel for Cardiac Tissue Engineering. *Acta Biomater*, 32, 10-23. doi:10.1016/j.actbio.2015.12.019
- Nayler, W. G. (1981). The Role of Calcium in the Ischemic Myocardium. *Am J Pathol*, 102, 262-270.
- Ng, F. S., Holzen, K. M., Koppel, A. C., Janks, D., Gordon, F., Wit, A. L., . . . Efimov, I. R. (2014). Adverse Remodeling of the Electrophysiological Response to Ischemia-Reperfusion in Human Heart Failure Is Associated with Remodeling of Metabolic Gene Expression. *Circ Arrhythm Electrophysiol*, 7(5), 875-882.
- Ng, N., Purshouse, K., Foskolou, I. P., Olcina, M. M., & Hammond, E. M. (2018). Challenges to DNA Replication in Hypoxic Conditions. *FEBS J*, 285(9), 1563-1571. doi:10.1111/febs.14377
- Nikkhah, M., Edalat, F., Manoucheri, S., & Khademhosseini, A. (2012). Engineering Microscale Topographies to Control the Cell-Substrate Interface. *Biomaterials*, 33(21), 5230-5246. doi:10.1016/j.biomaterials.2012.03.079
- Nunes, S. S., Miklas, J. W., Liu, J., Aschar-Sobbi, R., Xiao, Y., Zhang, B., . . . Radisic, M. (2013). Biowire: A Platform for Maturation of Human Pluripotent Stem Cell-Derived Cardiomyocytes. *Nat Methods*, 10(8), 781-787. doi:10.1038/nmeth.2524
- Oleaga, C., Jalilvand, G., Legters, G., Martin, C., Ekman, G., McAleer, C. W., . . . Hickman, J. J. (2019). A Human in Vitro Platform for the Evaluation of Pharmacology Strategies in Cardiac Ischemia. *APL Bioeng*, 3(3), 036103. doi:10.1063/1.5089237
- Ong, L. J. Y., Zhu, L., Tan, G. J. S., & Toh, Y. C. (2020). Quantitative Image-Based Cell Viability (Quanticv) Assay for Microfluidic 3d Tissue Culture Applications. *Micromachines (Basel)*, 11(7), 669. doi:10.3390/mi11070669

- Opie, L. H., Commerford, P. J., Gersh, B. J., & Pfeffer, M. A. (2006). Controversies in Ventricular Remodelling. *Lancet*, 367(9507), 356-367. doi:10.1016/S0140-6736(06)68074-4
- Parrag, I. C., Zandstra, P. W., & Woodhouse, K. A. (2012). Fiber Alignment and Coculture with Fibroblasts Improves the Differentiated Phenotype of Murine Embryonic Stem Cell-Derived Cardiomyocytes for Cardiac Tissue Engineering. *Biotechnol Bioeng*, 109(3), 813-822. doi:10.1002/bit.23353
- Parsa, H., Wang, B. Z., & Vunjak-Novakovic, G. (2017). A Microfluidic Platform for the High-Throughput Study of Pathological Cardiac Hypertrophy. *Lab Chip*, 17(19), 3264-3271. doi:10.1039/c7lc00415j
- Pasqualini, F. S., Nesmith, A. P., Horton, R. E., Sheehy, S. P., & Parker, K. K. (2016). Mechanotransduction and Metabolism in Cardiomyocyte Microdomains. *Biomed Res Int*, 2016, 4081638. doi:10.1155/2016/4081638
- Patino-Guerrero, A., Veldhuizen, J., Zhu, W., Migrino, R. Q., & Nikkhah, M. (2020). Three-Dimensional Scaffold-Free Microtissues Engineered for Cardiac Repair. *J Mater Chem B*, 8(34), 7571-7590. doi:10.1039/d0tb01528h
- Patten, R. D., & Hall-Porter, M. R. (2009). Small Animal Models of Heart Failure: Development of Novel Therapies, Past and Present. *Circ Heart Fail*, 2(2), 138-144. doi:10.1161/CIRCHEARTFAILURE.108.839761
- Paulussen, A., Raes, A., Matthijs, G., Snyders, D. J., Cohen, N., & Aerssens, J. (2002). A Novel Mutation (T65p) in the Pore Domain of the Human Potassium Channel Herg Results in the Long Qt Syndrome by Trafficking Deficiency. *J Biol Chem*, 277(50), 48610-48616. doi:10.1074/jbc.M206569200
- Pavesi, A., Adriani, G., Rasponi, M., Zervantonakis, I. K., Fiore, G. B., & Kamm, R. D. (2015). Controlled Electromechanical Cell Stimulation on-a-Chip. *Sci Rep*, 5, 11800. doi:10.1038/srep11800
- Peela, N., Barrientos, E. S., Truong, D., Mouneimne, G., & Nikkhah, M. (2017). Effect of Suberoylanilide Hydroxamic Acid (Saha) on Breast Cancer Cells within a Tumor-Stroma Microfluidic Model. *Int Bio*, 9(12), 988-999.
- Pilichou, K., Bezzina, C. R., Thiene, G., & Basso, C. (2011). Arrhythmogenic Cardiomyopathy: Transgenic Animal Models Provide Novel Insights into Disease Pathobiology. *Circ Cardiovasc Genet*, 4(3), 318-326. doi:10.1161/CIRCGENETICS.110.959031

- Piper, D. R., Hinz, W. A., Tallurri, C. K., Sanguinetti, M. C., & Tristani-Firouzi, M. (2005). Regional Specificity of Human Ether-a'-Go-Go-Related Gene Channel Activation and Inactivation Gating. *J Biol Chem*, 280(8), 7206-7217. doi:10.1074/jbc.M411042200
- Piper, D. R., Rupp, J., Sachse, F. B., Sanguinetti, M. C., & Tristani-Firouzi, M. (2007). Cooperative Interactions between R531 and Acidic Residues in the Voltage Sensing Module of Herg1 Channels. *Cellular Physiology and Biochemistry*, 21, 37-46.
- Porter, K. E., & Turner, N. A. (2009). Cardiac Fibroblasts: At the Heart of Myocardial Remodeling. *Pharmacology & Therapeutics*, 123, 255-278.
- Prabhakar, N. R., & Semenza, G. L. (2015). Oxygen Sensing and Homeostasis. *Physiology*, 30, 340-348.
- Radisic, M., Park, H., Chen, F., Salazar-Lazzaro, J. E., Wang, Y., Dennis, R., . . . Vunjak-Novakovic, G. (2006). Biomimetic Approach to Cardiac Tissue Engineering: Oxygen Carriers and Channeled Scaffolds. *Tissue Eng*, 12(8), 2077-2091. doi:10.1089/ten.2006.12.2077
- Radisic, M., Park, H., Gerecht, S., Cannizzaro, C., Langer, R., & Vunjak-Novakovic, G. (2007). Biomimetic Approach to Cardiac Tissue Engineering. *Philos Trans R Soc Lond B Biol Sci*, 362(1484), 1357-1368. doi:10.1098/rstb.2007.2121
- Rajamohan, D., Matsa, E., Kalra, S., Crutchley, J., Patel, A., George, V., & Denning, C. (2013). Current Status of Drug Screening and Disease Modelling in Human Pluripotent Stem Cells. *Bioessays*, 35(3), 281-298. doi:10.1002/bies.201200053
- Ran, F. A., Hsu, P. D., Lin, C. Y., Gootenberg, J. S., Konermann, S., Trevino, A. E., . . . Zhang, F. (2013). Double Nicking by Rna-Guided Cas9 for Enhanced Genome Editing Specificity. *Cell*, 154(6), 1380-1389. doi:10.1016/j.cell.2013.08.021
- Rashid, S. T., Salacinski, H. J., Hamilton, G., & Seifalian, A. M. (2004). The Use of Animal Models in Developing the Discipline of Cardiovascular Tissue Engineering: A Review. *Biomaterials*, 25(9), 1627-1637. doi:10.1016/s0142-9612(03)00522-2
- Raymond, M. J., Jr., Ray, P., Kaur, G., Singh, A. V., & Wan, L. Q. (2016). Cellular and Nuclear Alignment Analysis for Determining Epithelial Cell Chirality. *Ann Biomed Eng*, 44(5), 1475-1486. doi:10.1007/s10439-015-1431-3

- Rees, H. A., & Liu, D. R. (2018). Base Editing: Precision Chemistry on the Genome and Transcriptome of Living Cells. *Nature Reviews*, *19*, 770-788.
- Ren, C., Xu, K., Liu, Z., Shen, J., Han, F., Chen, Z., & Zhang, Z. (2015). Dual-Reporter Surrogate Systems for Efficient Enrichment of Genetically Modified Cells *Cell Mol Life Sci*, *72*, 2763-2772.
- Ren, L., Liu, W., Wang, Y., Wang, J. C., Tu, Q., Xu, J., . . . Wang, J. (2013). Investigation of Hypoxia-Induced Myocardial Injury Dynamics in a Tissue Interface Mimicking Microfluidic Device. *Anal Chem*, *85*(1), 235-244. doi:10.1021/ac3025812
- Renstrom, B., Liedtke, A. J., & Nellis, S. H. (1990). Mechanisms of Substrate Preference for Oxidative Metabolism During Early Myocardial Reperfusion. *Am J Physiol*, *259*(2 Pt 2), H317-323. doi:10.1152/ajpheart.1990.259.2.H317
- Richards, D. J., Li, Y., Kerr, C. M., Yao, J., Beeson, G. C., Coyle, R. C., . . . Mei, Y. (2020). Human Cardiac Organoids for the Modelling of Myocardial Infarction and Drug Cardiotoxicity. *Nat Biomed Eng*, *4*(4), 446-462. doi:10.1038/s41551-020-0539-4
- Ronaldson-Bouchard, K., Ma, S. P., Yeager, K., Chen, T., Song, L., Sirabella, D., . . . Vunjak-Novakovic, G. (2018). Advanced Maturation of Human Cardiac Tissue Grown from Pluripotent Stem Cells. *Nature*, *556*(7700), 239-243. doi:10.1038/s41586-018-0016-3
- Ross, J., Jr. (1991). Myocardial Perfusion-Contraction Matching. Implications for Coronary Heart Disease and Hibernation. *Circulation*, *83*(3), 1076-1083. doi:10.1161/01.cir.83.3.1076
- Sadeghi, A. H., Shin, S. R., Deddens, J. C., Fratta, G., Mandla, S., Yazdi, I. K., . . . Khademhosseini, A. (2017). Engineered 3d Cardiac Fibrotic Tissue to Study Fibrotic Remodeling. *Adv Healthc Mater*, *6*(11). doi:10.1002/adhm.201601434
- Saini, H., Navaei, A., Van Putten, A., & Nikkhah, M. (2015). 3d Cardiac Microtissues Encapsulated with the Co-Culture of Cardiomyocytes and Cardiac Fibroblasts. *Adv Healthc Mater*, *4*(13), 1961-1971. doi:10.1002/adhm.201500331
- Schaaf, S., Shibamiya, A., Mewe, M., Eder, A., Stohr, A., Hirt, M. N., . . . Hansen, A. (2011). Human Engineered Heart Tissue as a Versatile Tool in Basic Research and Preclinical Toxicology. *PLoS One*, *6*(10), e26397. doi:10.1371/journal.pone.0026397
- Schwartz P., P. M., Malliani A. (1975). The Long Qt Syndrome. *American Heart Journal*, *89*(3), 378-390.

- Schwartz, P. J., Ackerman, M. J., George, A. L., Jr., & Wilde, A. A. M. (2013). Impact of Genetics on the Clinical Management of Channelopathies. *J Am Coll Cardiol*, 62(3), 169-180. doi:10.1016/j.jacc.2013.04.044
- Semenza, G. L. (2014). Hypoxia-Inducible Factor 1 and Cardiovascular Disease. *Annu Rev Physiol*, 76, 39-56.
- Seo, Y., & Kinsella, T. J. (2009). Essential Role of DNA Base Excision Repair on Survival in an Acidic Tumor Microenvironment. *Cancer Res*, 69(18), 7285-7293. doi:10.1158/0008-5472.CAN-09-0624
- Shadrin, I. Y., Allen, B. W., Qian, Y., Jackman, C. P., Carlson, A. L., Juhas, M. E., & Bursac, N. (2017). Cardiopatch Platform Enables Maturation and Scale-up of Human Pluripotent Stem Cell-Derived Engineered Heart Tissues. *Nat Commun*, 8(1), 1825. doi:10.1038/s41467-017-01946-x
- Sharma, A., Li, G., Rajarajan, K., Hamaguchi, R., Burridge, P. W., & Wu, S. M. (2015). Derivation of Highly Purified Cardiomyocytes from Human Induced Pluripotent Stem Cells Using Small Molecule-Modulated Differentiation and Subsequent Glucose Starvation. *Jove-Journal of Visualized Experiments*(97). doi:ARTN e5262810.3791/52628
- Shi, Y. P., Thouta, S., & Claydon, T. W. (2020). Modulation of Herg K(+) Channel Deactivation by Voltage Sensor Relaxation. *Front Pharmacol*, 11, 139. doi:10.3389/fphar.2020.00139
- Shinde, A. V., & Frangogiannis, N. G. (2014). Fibroblasts in Myocardial Infarction: A Role in Inflammation and Repair. *J Mol Cell Cardiol*, 70, 74-82. doi:10.1016/j.yjmcc.2013.11.015
- Sidorov, V. Y., Samson, P. C., Sidorova, T. N., Davidson, J. M., Lim, C. C., & Wikswo, J. P. (2017). I-Wire Heart-on-a-Chip I: Three-Dimensional Cardiac Tissue Constructs for Physiology and Pharmacology. *Acta Biomater*, 48, 68-78. doi:10.1016/j.actbio.2016.11.009
- Snir, M., Kehat, I., Gepstein, A., Coleman, R., Itskovitz-Eldor, J., & Livne, E. G., L. (2003). Assessment of the Ultrastructural and Proliferative Properties of Human Embryonic Stem Cell-Derived Cardiomyocytes. *Am J Physiol Heart Circ Physiol*, 285, 2355-2363.

- Song, H., Zandstra, P. W., & Radisic, M. (2011). Engineered Heart Tissue Model of Diabetic Myocardium. *Tissue Eng Part A*, 17(13-14), 1869-1878. doi:10.1089/ten.TEA.2010.0617
- Spencer, T. M., Blumenstein, R. F., Pryse, K. M., Lee, S.-L., Glaubke, D. A., Carlson, B. E., . . . Genin, G. M. (2016). Fibroblasts Slow Conduction Velocity in a Reconstituted Tissue Model of Fibrotic Cardiomyopathy. *ACS Biomaterials Science & Engineering*, 3(11), 3022-3028. doi:10.1021/acsbiomaterials.6b00576
- Splawski, I., Timothy, K. W., Sharpe, L. M., Decher, N., Kumar, P., Bloise, R., . . . Keating, M. T. (2004). Ca(V)1.2 Calcium Channel Dysfunction Causes a Multisystem Disorder Including Arrhythmia and Autism. *Cell*, 119(1), 19-31. doi:10.1016/j.cell.2004.09.011
- Standage-Beier, K., Tekel, S. J., Brookhouser, N., Schwarz, G., Nguyen, T., Wang, X., & Brafman, D. A. (2019). A Transient Reporter for Editing Enrichment (Tree) in Human Cells. *Nucleic Acids*, 47, e120.
- Stansfield, W., Ranek, M., Pendse, A., Schisler, J., Wang, S., Pulinilkunnil, T., & Willis, M. (2014). The Pathophysiology of Cardiac Hypertrophy and Heart Failure *Cellular and Molecular Pathobiology of Cardiovascular Disease* (pp. 51-78): Academic Press.
- Stemmer, M., Thumberger, T., del Sol Keyer, M., Wittbrodt, J., & Mateo, J. L. (2015). Cctop: An Intuitive, Flexible and Reliable Crispr/Cas9 Target Prediction Tool. *PLOS ONE*, 10.
- Stengl, M. (2010). Experimental Models of Spontaneous Ventricular Arrhythmias and of Sudden Cardiac Death. *Physiol Res*, 59 Suppl 1, S25-31.
- Stohr, A., Friedrich, F. W., Flenner, F., Geertz, B., Eder, A., Schaaf, S., . . . Eschenhagen, T. (2013). Contractile Abnormalities and Altered Drug Response in Engineered Heart Tissue from Mybpc3-Targeted Knock-in Mice. *J Mol Cell Cardiol*, 63, 189-198. doi:10.1016/j.yjmcc.2013.07.011
- Subbiah, R. N., Clarke, C. E., Smith, D. J., Zhao, J., Campbell, T. J., & Vandenberg, J. I. (2004). Molecular Basis of Slow Activation of the Human Ether-a-Go-Go Related Gene Potassium Channel. *J Physiol*, 558(Pt 2), 417-431. doi:10.1113/jphysiol.2004.062588
- Sun, N., Yazawa, M., Liu, J., Han, L., Sanchez-Freire, V., Abilez, O. J., . . . Wu, J. C. (2012). Patient-Specific Induced Pluripotent Stem Cells as a Model for Familial

- Dilated Cardiomyopathy. *Sci Transl Med*, 4(130), 130ra147. doi:10.1126/scitranslmed.3003552
- Talman, V., & Ruskoaho, H. (2016). Cardiac Fibrosis in Myocardial Infarction-from Repair and Remodeling to Regeneration. *Cell Tissue Res*, 365(3), 563-581. doi:10.1007/s00441-016-2431-9
- Tekel, S. J., Brookhouser, N., Standage-Beier, K., Wang, X., & Brafman, D. A. (2021). Cytosine and Adenosine Base Editing in Human Pluripotent Stem Cells Using Transient Reporters for Editing Enrichment. *Nat Protoc*, 16, 3596-3624.
- Thomas, D., Kiehn, J., Katus, H. A., & Karle, C. A. (2003). Defective Protein Trafficking in Herg-Associated Hereditary Long Qt Syndrome (Lqt2): Molecular Mechanisms and Restoration of Intracellular Protein Processing. *Cardiovasc Res*, 60(2), 235-241. doi:10.1016/j.cardiores.2003.08.002
- Tiburcy, M., Hudson, J. E., Balfanz, P., Schlick, S., Meyer, T., Chang Liao, M. L., . . . Zimmermann, W. H. (2017). Defined Engineered Human Myocardium with Advanced Maturation for Applications in Heart Failure Modeling and Repair. *Circulation*, 135(19), 1832-1847. doi:10.1161/CIRCULATIONAHA.116.024145
- To, K. W., Sedelnikova, O. A., Samons, M., Bonner, W. M., & Huang, L. E. (2006). The Phosphorylation Status of Pas-B Distinguishes Hif-1 α from Hif-2 α in Nbs1 Repression. *Eur Mol Bio Org*, 25, 4784-4794.
- Tohyama, S., Hattori, F., Sano, M., Hishiki, T., Nagahata, Y., Matsuura, T., . . . Fukuda, K. (2013). Distinct Metabolic Flow Enables Large-Scale Purification of Mouse and Human Pluripotent Stem Cell-Derived Cardiomyocytes. *Cell Stem Cell*, 12(1), 127-137. doi:10.1016/j.stem.2012.09.013
- Truong, D., Fiorelli, R., Barrientos, E. S., Melendez, E. L., Sanai, N., Mehta, S., & Nikkhah, M. (2019). A Three-Dimensional (3d) Organotypic Microfluidic Model for Glioma Stem Cells - Vascular Interactions. *Biomaterials*, 198, 63-77. doi:10.1016/j.biomaterials.2018.07.048
- Truong, D., Puleo, J., Llave, A., Mouneimne, G., Kamm, R. D., & Nikkhah, M. (2016). Breast Cancer Cell Invasion into a Three Dimensional Tumor-Stroma Microenvironment. *Sci Rep*, 6, 34094. doi:10.1038/srep34094
- Truong, D. D., Kratz, A., Park, J. G., Barrientos, E. S., Saini, H., Nguyen, T., . . . Nikkhah, M. (2019). A Human Organotypic Microfluidic Tumor Model Permits Investigation of the Interplay between Patient-Derived Fibroblasts and Breast Cancer Cells. *Cancer Research*, 79(12), 3139-3151. doi:10.1158/0008-5472.Can-18-2293

- Underlying Cause of Death, 1999-2018. (2020). from Centers for Disease Control and Prevention
- Uosaki, H., Fukushima, H., Takeuchi, A., Matsuoka, S., Nakatsuji, N., Yamanaka, S., & Yamashita, J. K. (2011). Efficient and Scalable Purification of Cardiomyocytes from Human Embryonic and Induced Pluripotent Stem Cells by Vcam1 Surface Expression. *PLoS One*, *6*(8), e23657. doi:10.1371/journal.pone.0023657
- Valderrabano, M. (2007). Influence of Anisotropic Conduction Properties in the Propagation of the Cardiac Action Potential. *Prog Biophys Mol Biol*, *94*(1-2), 144-168. doi:10.1016/j.pbiomolbio.2007.03.014
- van den Borne, S. W., Diez, J., Blankesteyn, W. M., Verjans, J., Hofstra, L., & Narula, J. (2010). Myocardial Remodeling after Infarction: The Role of Myofibroblasts. *Nat Rev Cardiol*, *7*(1), 30-37. doi:10.1038/nrcardio.2009.199
- van Spreeuwel, A. C. C., Bax, N. A. M., van Nierop, B. J., Aartsma-Rus, A., Goumans, M. T. H., & Bouten, C. V. C. (2017). Mimicking Cardiac Fibrosis in a Dish: Fibroblast Density Rather Than Collagen Density Weakens Cardiomyocyte Function. *J Cardiovasc Transl Res*, *10*(2), 116-127. doi:10.1007/s12265-017-9737-1
- Vandenberg, J. I., Perry, M. D., Perrin, M. J., Mann, S. A., Ke, Y., & Hill, A. P. (2012). Herg K(+) Channels: Structure, Function, and Clinical Significance. *Physiol Rev*, *92*(3), 1393-1478. doi:10.1152/physrev.00036.2011
- Vandenburg, H., Shansky, J., Benesch-Lee, F., Barbata, V., Reid, J., Thorrez, L., . . . Crawford, G. (2008). Drug-Screening Platform Based on the Contractility of Tissue-Engineered Muscle. *Muscle Nerve*, *37*(4), 438-447. doi:10.1002/mus.20931
- Veerman, C. C., Kosmidis, G., Mummery, C. L., Casini, S., Verkerk, A. O., & Bellin, M. (2015). Immaturity of Human Stem-Cell-Derived Cardiomyocytes in Culture: Fatal Flaw or Soluble Problem? *Stem Cells Dev*, *24*(9), 1035-1052. doi:10.1089/scd.2014.0533
- Veldhuizen, J., Cutts, J., Brafman, D. A., Migrino, R. Q., & Nikkhah, M. (2020). Engineering Anisotropic Human Stem Cell-Derived Three-Dimensional Cardiac Tissue on-a-Chip. *Biomaterials*, *256*, 120195. doi:10.1016/j.biomaterials.2020.120195
- Veldhuizen, J., Migrino, R. Q., & Nikkhah, M. (2019). Three-Dimensional Microengineered Models of Human Cardiac Diseases. *J Biol Eng*, *13*, 29. doi:10.1186/s13036-019-0155-6

- Veldhuizen, J., & Nikkhah, M. (2021). Developing 3d Organized Human Cardiac Tissue within a Microfluidic Platform. *JoVE*, 172.
- Verhulsel, M., Vignes, M., Descroix, S., Malaquin, L., Vignjevic, D. M., & Viovy, J. L. (2014). A Review of Microfabrication and Hydrogel Engineering for Micro-Organs on Chips. *Biomaterials*, 35(6), 1816-1832. doi:10.1016/j.biomaterials.2013.11.021
- Virani, S. S., Alonso, A., Benjamin, E. J., Bittencourt, M. S., Callaway, C. W., Carson, A. P., . . . Stroke Statistics, S. (2020). Heart Disease and Stroke Statistics-2020 Update: A Report from the American Heart Association. *Circulation*, 141(9), e139-e596. doi:10.1161/CIR.0000000000000757
- Vyas, H., Hejlik, J., & Ackerman, M. J. (2006). Epinephrine Qt Stress Testing in the Evaluation of Congenital Long-Qt Syndrome: Diagnostic Accuracy of the Paradoxical Qt Response. *Circulation*, 113(11), 1385-1392. doi:10.1161/CIRCULATIONAHA.105.600445
- Wallace, E., Howard, L., Liu, M., O'Brien, T., Ward, D., Shen, S., & Prendiville, T. (2019). Long Qt Syndrome: Genetics and Future Perspective. *Pediatr Cardiol*, 40(7), 1419-1430. doi:10.1007/s00246-019-02151-x
- Wang, C., Lu, H., & Schwartz, M. A. (2012). A Novel in Vitro Flow System for Changing Flow Direction on Endothelial Cells. *J Biomech*, 45(7), 1212-1218. doi:10.1016/j.jbiomech.2012.01.045
- Wang, G., McCain, M. L., Yang, L., He, A., Pasqualini, F. S., Agarwal, A., . . . Pu, W. T. (2014). Modeling the Mitochondrial Cardiomyopathy of Barth Syndrome with Induced Pluripotent Stem Cell and Heart-on-Chip Technologies. *Nat Med*, 20(6), 616-623. doi:10.1038/nm.3545
- Wang, Y., Liang, P., Lan, F., Wu, H., Lisowski, L., Gu, M., . . . Wu, J. C. (2014). Genome Editing of Isogenic Human Induced Pluripotent Stem Cells Recapitulates Long Qt Phenotype for Drug Testing. *J Am Coll Cardiol*, 64(5), 451-459. doi:10.1016/j.jacc.2014.04.057
- Watson, C. J., Collier, P., Tea, I., Neary, R., Watson, J. A., Robinson, C., . . . Baugh, J. A. (2014). Hypoxia-Induced Epigenetic Modifications Are Associated with Cardiac Tissue Fibrosis and the Development of a Myofibroblast-Like Phenotype. *Hum Mol Genet*, 23(8), 2176-2188. doi:10.1093/hmg/ddt614
- Webster, K. A., Discher, D. J., Kaiser, S., Hernandez, O., Sato, B., & Bishopric, N. H. (1999). Hypoxia-Activated Apoptosis of Cardiac Myocytes Requires

- Reoxygenation or a Ph Shift and Is Independent of P53. *J Clin Invest*, 104, 239-252.
- Wei, H., Zhang, X. H., Clift, C., Yamaguchi, N., & Morad, M. (2018). Crispr/Cas9 Gene Editing of Ryr2 in Human Stem Cell-Derived Cardiomyocytes Provides a Novel Approach in Investigating Dysfunctional Ca(2+) Signaling. *Cell Calcium*, 73, 104-111. doi:10.1016/j.ceca.2018.04.009
- Winegrad, S., Henrion, D., Rappaport, L., & Samuel, J. L. (1999). Self-Protection by Cardiac Myocytes against Hypoxia and Hyperoxia. *Circ Res*, 85(8), 690-698. doi:10.1161/01.res.85.8.690
- Witchel, H. J., & Hancox, J. C. (2000). Familial and Acquired Long Qt Syndrome and the Cardiac Rapid Delayed Rectifier Potassium Current. *Clin Exp Pharmacol Physiol*, 27(10), 753-766. doi:10.1046/j.1440-1681.2000.03337.x
- Yadid, M., Lind, J. U., Ardon, H. A. M., Sheehy, S. P., Dickinson, L. E., Eweje, F., . . . Parker, K. K. (2020). Endothelial Extracellular Vesicles Contain Protective Proteins and Rescue Ischemia-Reperfusion Injury in a Human Heart-on-Chip. *Sci Transl Med*, 12(565), eaax8005. doi:10.1126/scitranslmed.aax8005
- Yang, B., Yang, L., & Chen, J. (2019). Development and Application of Base Editors. *CRISPR J*, 2(2), 91-104. doi:10.1089/crispr.2019.0001
- Yang, G., & Huang, X. (2019). Methods and Applications of Crispr/Cas System for Genome Editing in Stem Cells. *Cell Regen*, 8(2), 33-41. doi:10.1016/j.cr.2019.08.001
- Yang, X., Pabon, L., & Murry, C. E. (2014). Engineering Adolescence: Maturation of Human Pluripotent Stem Cell-Derived Cardiomyocytes. *Circ Res*, 114, 511-523.
- Yazawa, M., Hsueh, B., Jia, X., Pasca, A. M., Bernstein, J. A., Hallmayer, J., & Dolmetsch, R. E. (2011). Using Induced Pluripotent Stem Cells to Investigate Cardiac Phenotypes in Timothy Syndrome. *Nature*, 471(7337), 230-234. doi:10.1038/nature09855
- Yokoo, N., Baba, S., Kaichi, S., Niwa, A., Mima, T., Doi, H., . . . Heike, T. (2009). The Effects of Cardioactive Drugs on Cardiomyocytes Derived from Human Induced Pluripotent Stem Cells. *Biochem Biophys Res Commun*, 387(3), 482-488. doi:10.1016/j.bbrc.2009.07.052
- Yoshinaga, D., Baba, S., Makiyama, T., Shibata, H., Hirata, T., Akagi, K., . . . Heike, T. (2019). Phenotype-Based High-Throughput Classification of Long Qt Syndrome

- Subtypes Using Human Induced Pluripotent Stem Cells. *Stem Cell Reports*, *13*, 394-404.
- Yu, J., Vodyanik, M. A., Smuga-Otto, K., Antosiewicz-Bourget, J., Frane, J. L., Tian, S., . . . Thomson, J. A. (2007). Induced Pluripotent Stem Cell Lines Derived from Human Somatic Cells. *Science*, *318*(5858), 1917-1920. doi:10.1126/science.1151526
- Zaragoza, C., Gomez-Guerrero, C., Martin-Ventura, J. L., Blanco-Colio, L., Lavin, B., Mallavia, B., . . . Egado, J. (2011). Animal Models of Cardiovascular Diseases. *J Biomed Biotechnol*, *2011*, 497841. doi:10.1155/2011/497841
- Zhang, D., Shadrin, I. Y., Lam, J., Xian, H. Q., Snodgrass, H. R., & Bursac, N. (2013). Tissue-Engineered Cardiac Patch for Advanced Functional Maturation of Human Esc-Derived Cardiomyocytes. *Biomaterials*, *34*(23), 5813-5820. doi:10.1016/j.biomaterials.2013.04.026
- Zhang, J., Tao, R., Campbell, K. F., Carvalho, J. L., Ruiz, E. C., Kim, G. C., . . . Kamp, T. J. (2019). Functional Cardiac Fibroblasts Derived from Human Pluripotent Stem Cells Via Second Heart Field Progenitors. *Nat Commun*, *10*(1), 2238. doi:10.1038/s41467-019-09831-5
- Zhang, M., Liu, J., Jiang, M., Wu, D. M., Sonawane, K., Guy, H. R., & Tseng, G. N. (2005). Interactions between Charged Residues in the Transmembrane Segments of the Voltage-Sensing Domain in the Herg Channel. *J Membr Biol*, *207*, 169-181.
- Zhang, M., Liu, J., & Tseng, G. N. (2004). Gating Charges in the Activation and Inactivation Processes of the Herg Channel. *J Gen Physiol*, *124*(6), 703-718. doi:10.1085/jgp.200409119
- Zhao, H., Li, X., Zeng, Y., Zhao, L., Ding, H., Sun, W., & Du, Y. (2014). Microengineered in Vitro Model of Cardiac Fibrosis through Modulating Myofibroblast Mechanotransduction. *Biofabrication*, *6*, 045009.
- Zhao, M. T., Chen, H., Liu, Q., Shao, N. Y., Sayed, N., Wo, H. T., . . . Wu, J. C. (2017). Molecular and Functional Resemblance of Differentiated Cells Derived from Isogenic Human Ipscs and Scent-Derived Escs. *Proc Natl Acad Sci U S A*, *114*(52), E11111-E11120. doi:10.1073/pnas.1708991114
- Zhao, Y., Rafatian, N., Feric, N. T., Cox, B. J., Aschar-Sobbi, R., Wang, E. Y., . . . Radisic, M. (2019). A Platform for Generation of Chamber-Specific Cardiac Tissues and Disease Modeling. *Cell*, *176*(4), 913-927 e918. doi:10.1016/j.cell.2018.11.042

Zimmermann, W. H., Schneiderbanger, K., Schubert, P., Didie, M., Munzel, F., Heubach, J. F., . . . Eschenhagen, T. (2002). Tissue Engineering of a Differentiated Cardiac Muscle Construct. *Circ Res*, *90*(2), 223-230.

Zuppinger, C. (2019). 3d Cardiac Cell Culture: A Critical Review of Current Technologies and Applications. *Front Cardiovasc Med*, *6*, 87. doi:10.3389/fcvm.2019.00087

APPENDIX A

SUPPLEMENTARY FIGURES FOR CHAPTER 2

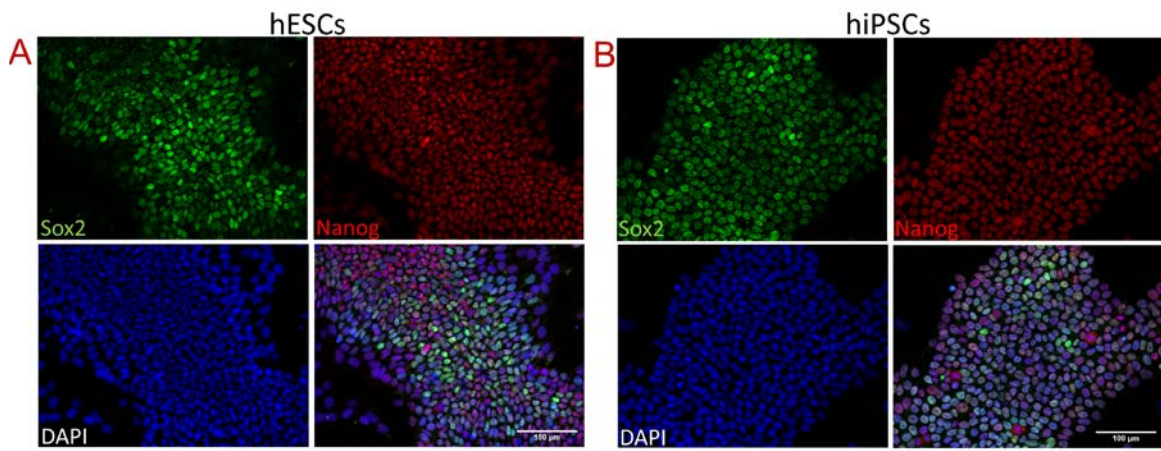


Figure A.1: Pluripotency characterization of human stem cells. Immunostaining of Sox2 (green) and Nanog (red) and DAPI (blue) of human embryonic stem cells (A) and human induced pluripotent stem cells (B).

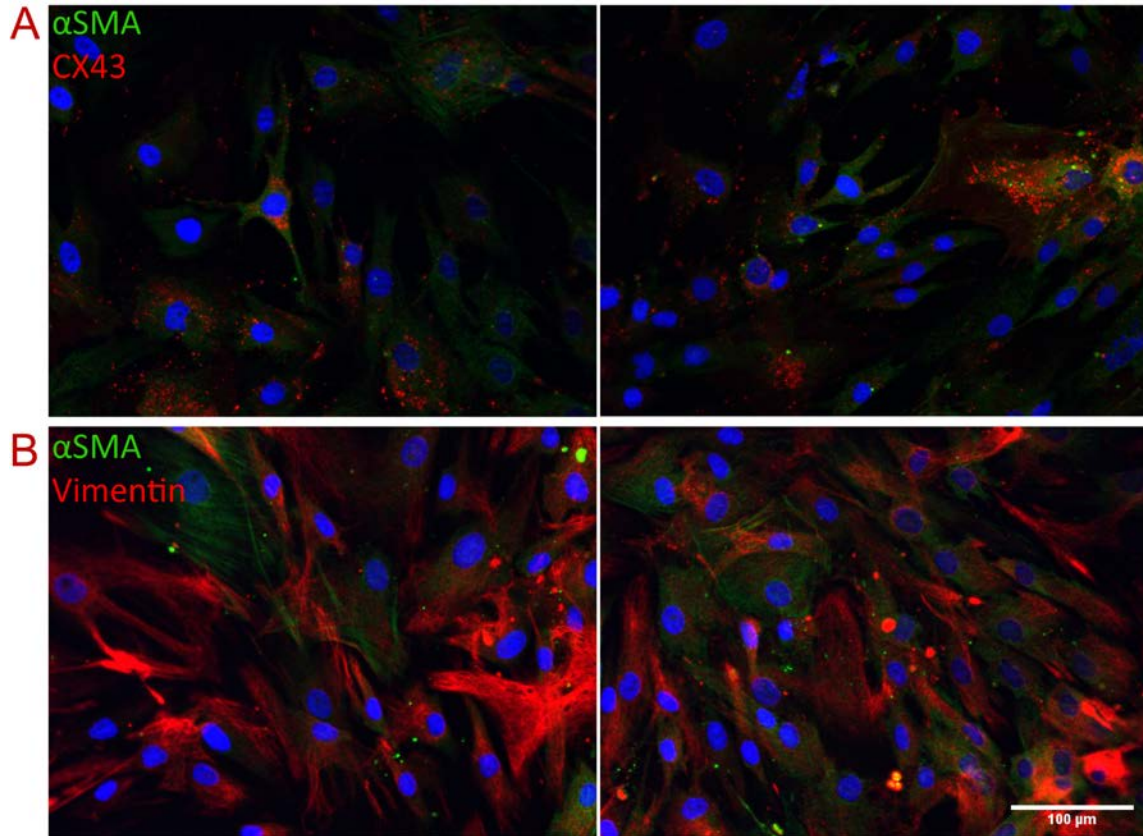


Figure A.2: Characterization of human cardiac fibroblasts (hCFs). (A-B) Representative IF staining of hCFs, showing minimal positive α -smooth muscle actin staining (green) and positive connexin43 expression (A), and abundant vimentin expression (B).

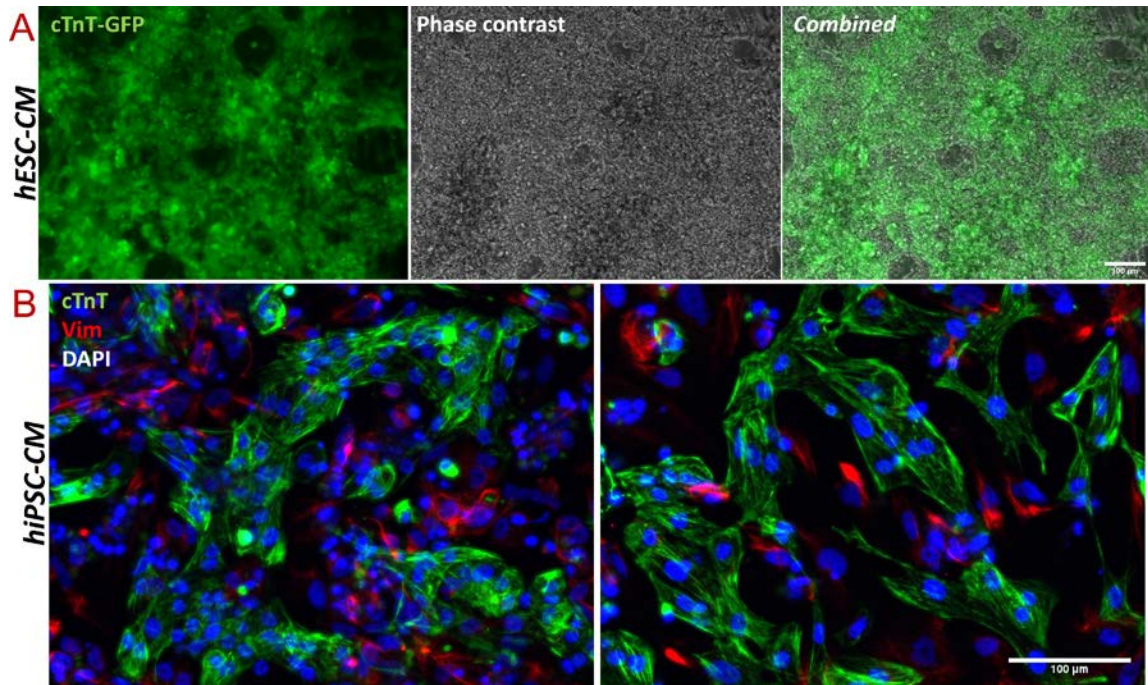


Figure A.3: Additional characterization of hPSC-derived CMs. (A) Expression of cTnT in hESC-derived CM population, with cTnT-GFP expression in left panel, phase contrast in middle panel, and combined in right panel. (B) Expression of cTnT (green), vimentin (red), and DAPI (blue) of fixed hiPSC-derived CM populations.

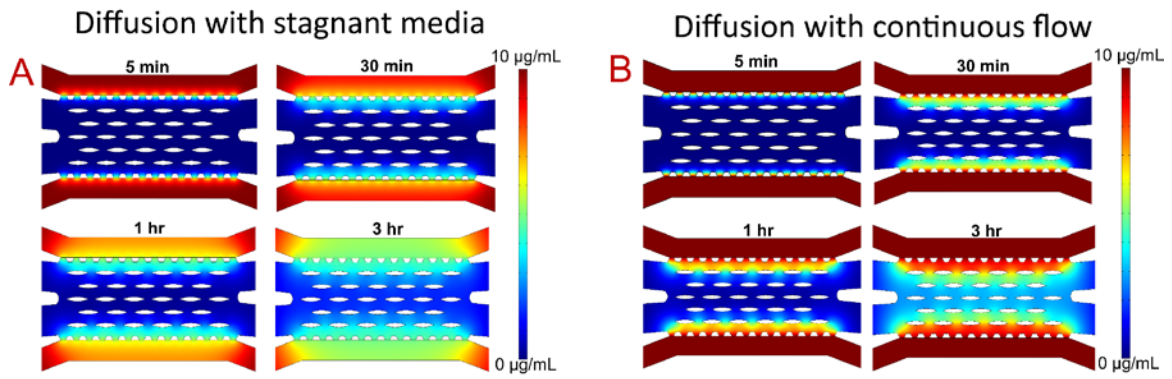


Figure A.4: Simulation of 10kDa dextran diffusion from media to tissue channels. Concentration gradient established over time with (A) stagnant conditions, and (B) under continuous flow.

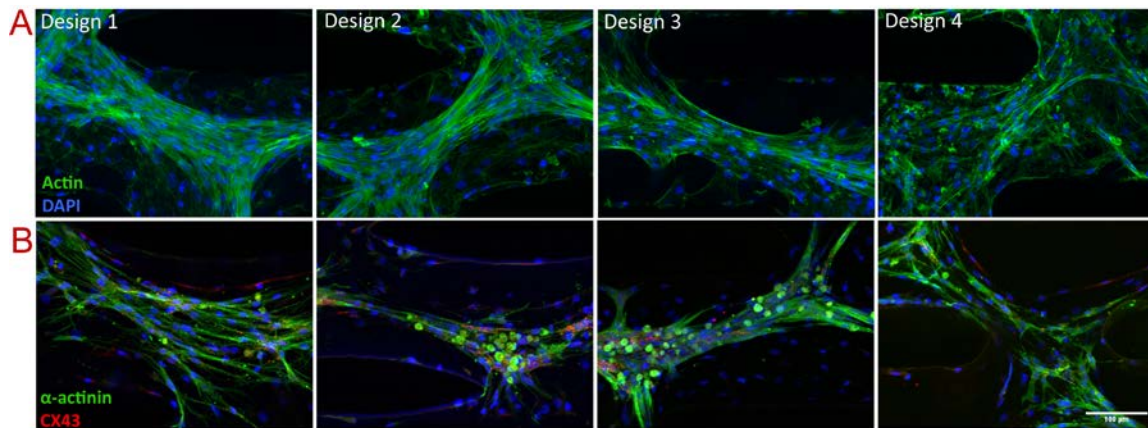


Figure A.5: Additional immunostaining of rat-derived cardiac tissues with the different device designs. (A) Cytoskeletal staining (F-actin=green, DAPI=blue) and (B) cardiac-specific marker staining (sarcomeric α -actinin=green, connexin 43=red, DAPI=blue) of rat-derived cardiac tissues within various microfluidic chip designs.

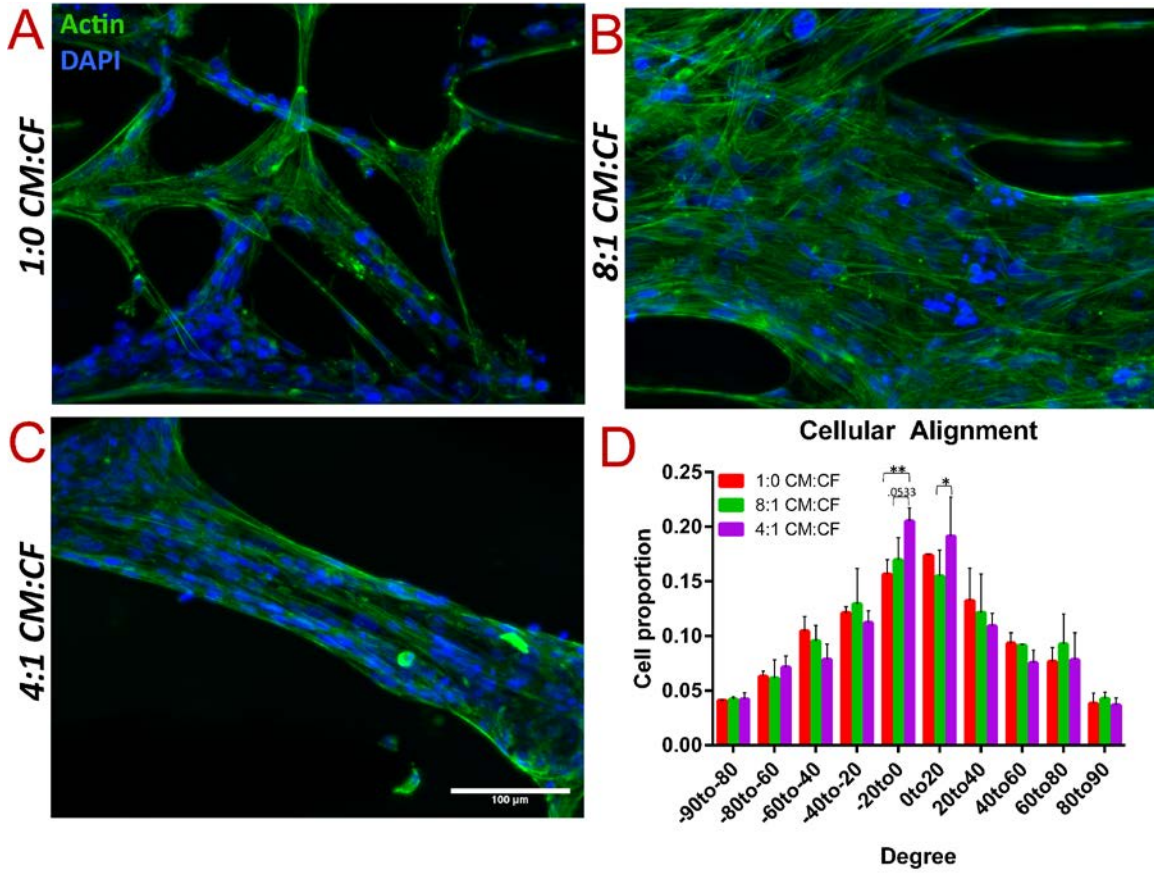


Figure A.6: Alignment comparison of tissues with varying cell compositions of human CM:CF. Cytoskeletal staining shown of (A) 1:0 CM:CF, (B) 8:1 CM:CF, and (C) 4:1 CM:CF tissues formed after 14 days within device with posts, and quantification of cell alignment in (D). Statistics performed through ANOVA of n=2-4 experiments of hiPSC-derived tissues, with p-values: * <0.05 , ** <0.01 .

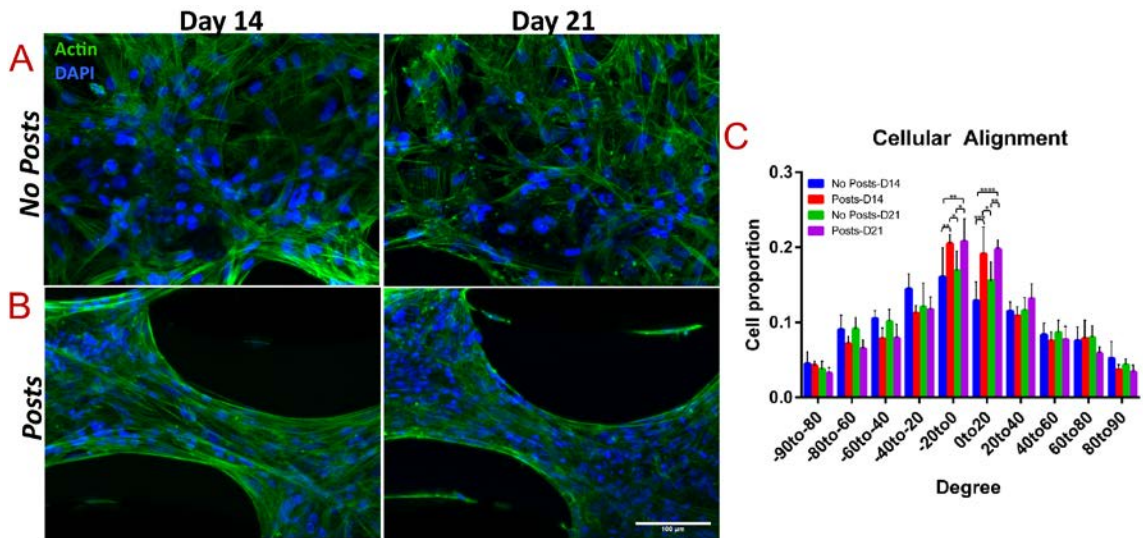


Figure A.7: Alignment comparison of extended culture. Cytoskeletal staining of hiPSC-derived tissues formed within (A) devices without posts and (B) devices with posts, with Day 14 in the left panel and Day 21 on the right panel, and corresponding quantification of cell alignment in (C). Statistics performed through ANOVA of n=3-4 experiments of hiPSC-derived tissues, with p-values: * <0.05 , ** <0.01 , *** <0.001 .

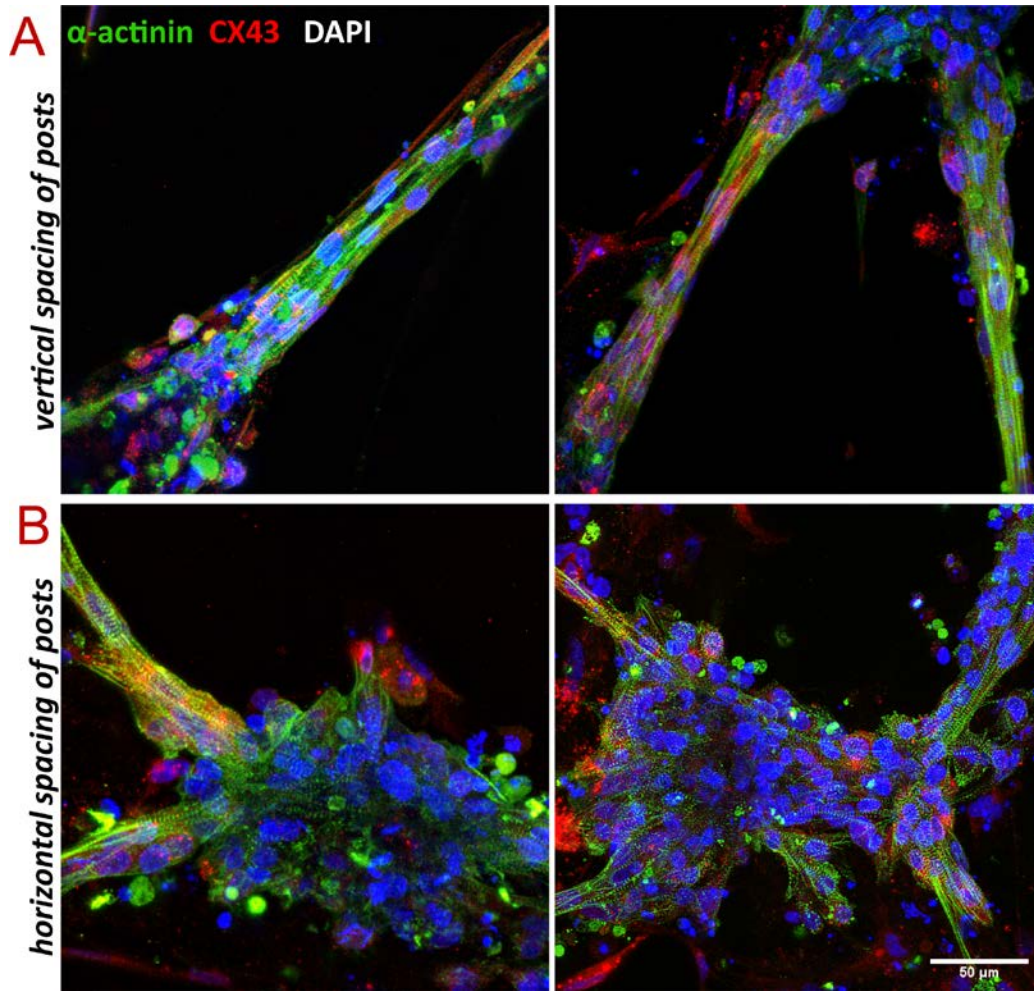


Figure A.8: Additional human cardiac tissue characterization within devices with posts. (A) Tissues formed between the vertical spacing of posts, and (B) tissues formed between the horizontal spacing of posts. (sarcomeric α -actinin=green, connexin 43=red, DAPI=blue)

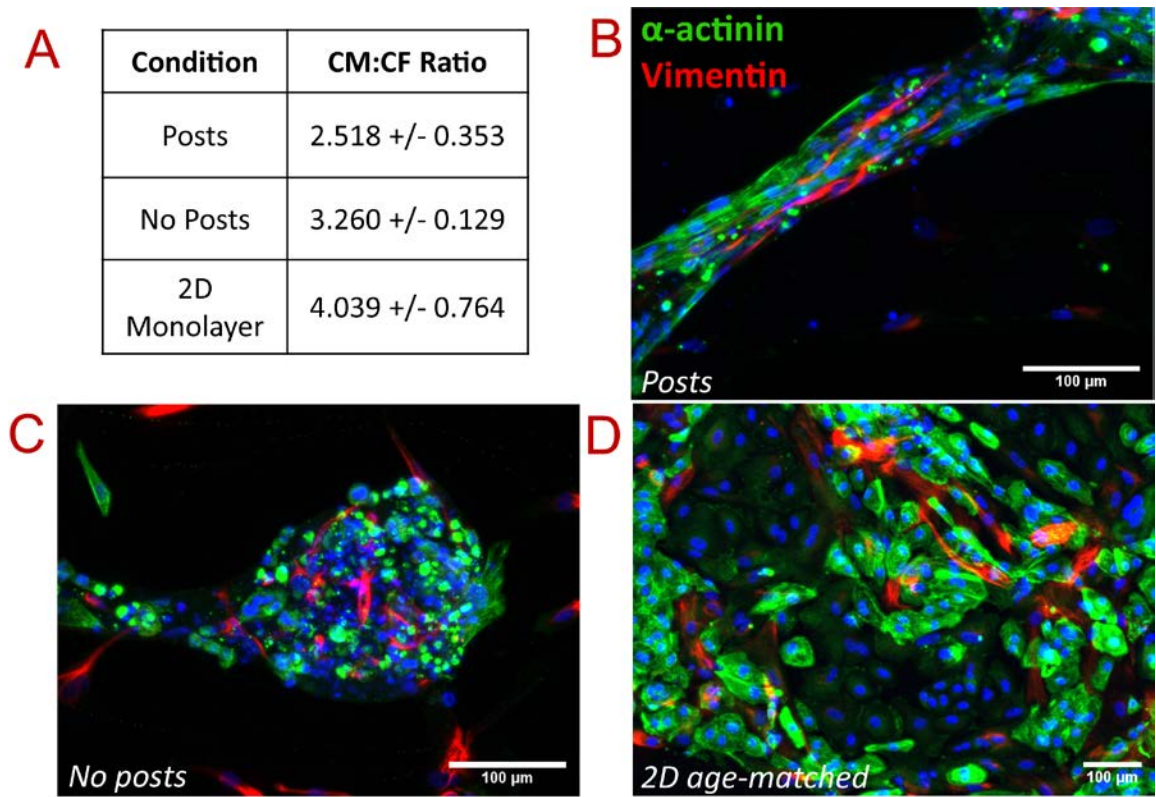


Figure A.9: Analysis of cardiac tissue composition within stem cell-derived cardiac tissue in age-matched monolayer and devices. (A) Table of calculated CM:CF ratios based on sarcomeric α -actinin and vimentin staining at Day 14. (B-D) Corresponding immunostaining images for CM:CF quantification, with SAA (green) and vimentin (red): (B) 3D tissue in devices with posts at 20X, (C) 3D tissue in devices without posts at 20X, and (D) age-matched monolayer at 10X.

APPENDIX B

SUPPLEMENTARY FIGURES FOR CHAPTER 3

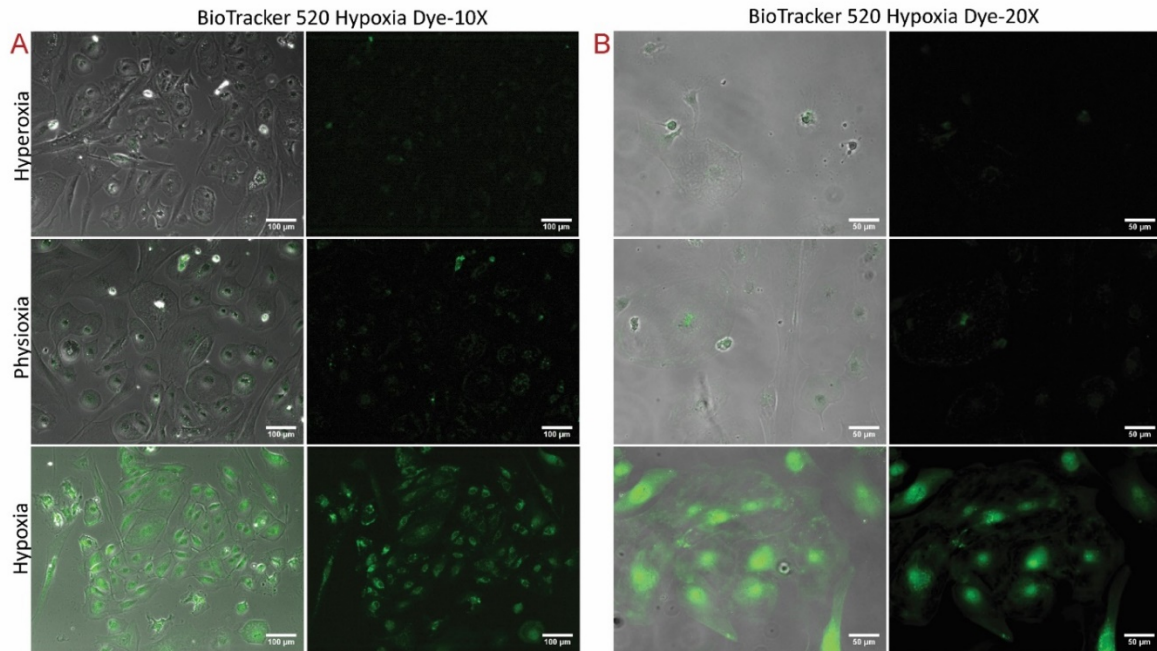


Figure B.1: Validation of oxygen levels in the experimental setup. 2D co-cultures of CM:CF were incubated with BioTracker 520 Green Dye then exposed to the different oxygen conditions, for a total duration of 4 hours, then imaged for Biotracker dye intensity, with (A) 10X and (B) 20X magnification.

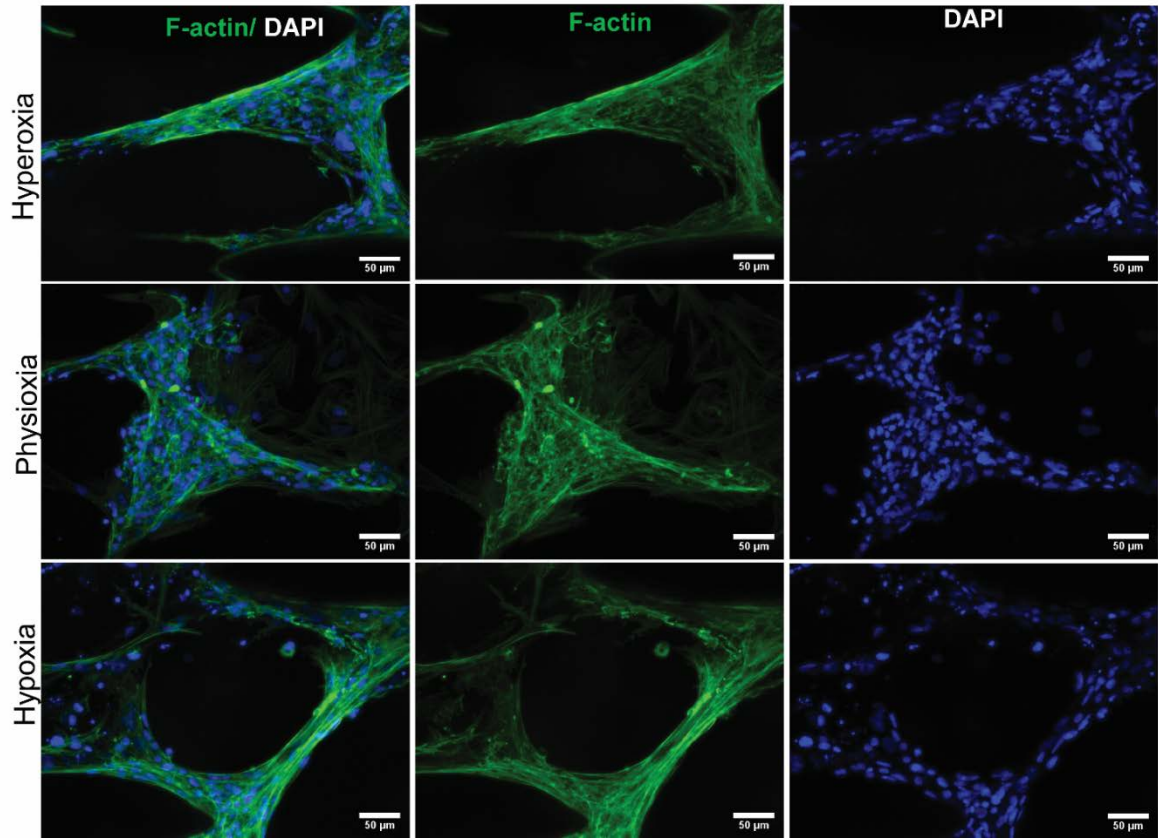


Figure B.2: Additional F-actin staining of 3D cardiac tissues. Immunostaining of F-actin fibers (green) of cardiac tissues within horizontal spacing between posts.

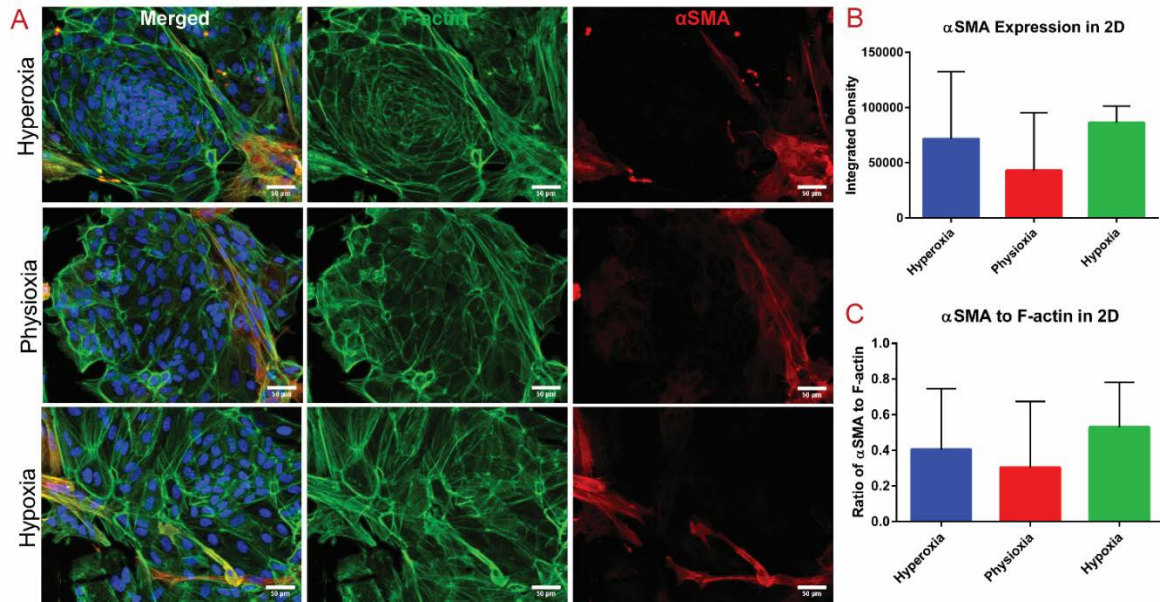


Figure B.3: Assessment of fibrotic response in 2D tissues exposed to the varying oxygen levels.

(A) Immunostaining of cardiac tissue after exposure to the different oxygen levels, with F-actin=green and α SMA=red. Quantification of (B) integrated density of α SMA stain and (C) integrated density of α SMA stain normalized to the integrated density of F-actin fibers.

APPENDIX C

SUPPLEMENTARY FIGURES FOR CHAPTER 4

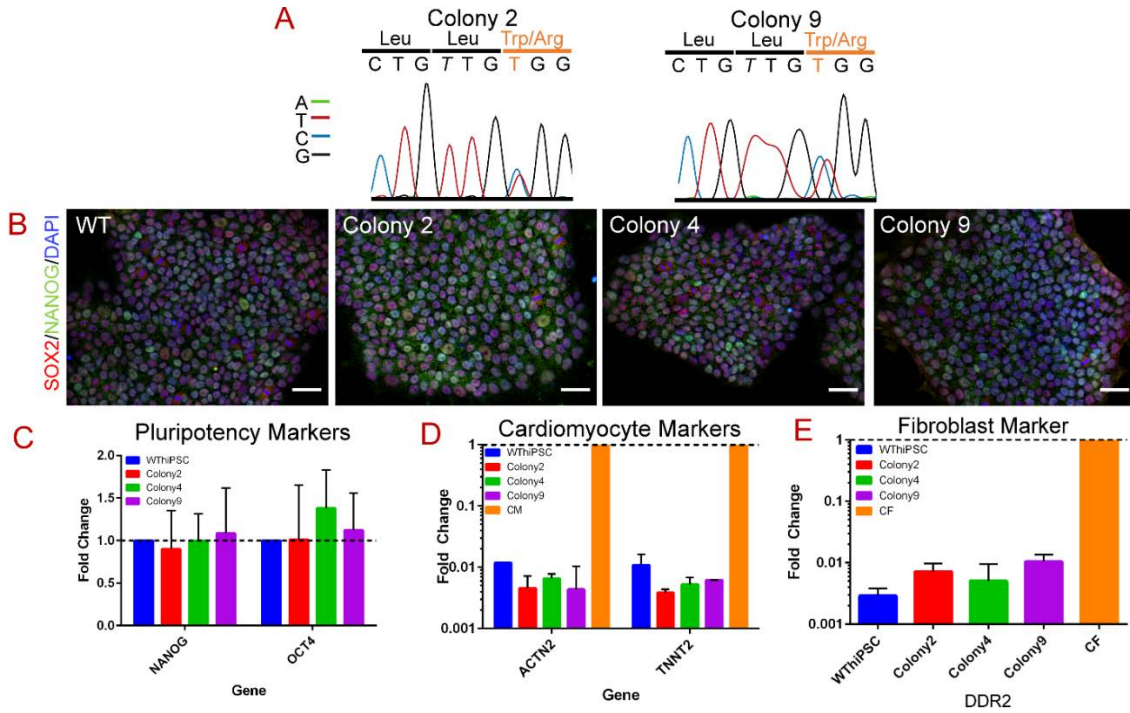


Figure C.1: Characterization of hiPSC clones with R531W edit in KCNH2

(A) Trace files of the target site in Colony 2 and Colony 9, showing a heterozygous edit in c.C1591T. (B) Immunostaining of pluripotency markers, where SOX2=red and NANOG=green, for all edited colonies and WT hiPSCs. Gene expression analysis of (C) pluripotency, (D) cardiomyocyte, and (E) fibroblast markers of edited colonies, normalized to the respective positive control.

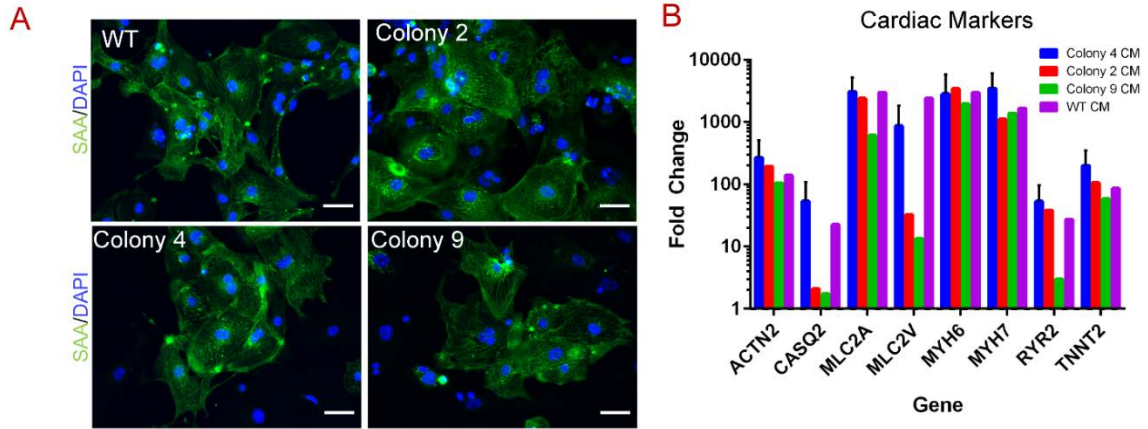


Figure C.2 Cardiomyocyte differentiation potential of hiPSC clones with R531W edit in

KCNH2

(A) Immunostaining of sarcomeric α -actinin and (B) gene expression analysis of an array

of cardiac markers of cardiomyocytes differentiated from edited colonies and WT

hiPSCs.

APPENDIX D

LIST OF SUPPLEMENTARY VIDEOS

Supplementary videos are readable using media players in Windows operating system.

Chapter 2:

Movie A.1: Rat-derived cardiac tissue after 14 days in device of Design 1.

Movie A.2: Rat-derived cardiac tissue after 14 days in device of Design 2.

Movie A.3: Rat-derived cardiac tissue after 14 days in device of Design 3.

Movie A.4: Rat-derived cardiac tissue after 14 days in device of Design 4.

Movie A.5: Human stem cell-derived cardiac tissue after 14 days in device of Design 1.

Movie A.6: Human stem cell-derived cardiac tissue after 14 days in no post device.

Movie A.7: Human stem cell-derived cardiac tissue after 14 days within expanded tissue region.

Movie A.8: Spontaneous calcium transients of human stem cell-derived cardiac tissues within devices without posts

Movie A.9: Spontaneous calcium transients of human stem cell-derived cardiac tissues within devices with posts

Chapter 3:

Movie B.1: Human stem cell-derived cardiac tissue after 24 hours of exposure to hyperoxia conditions.

Movie B.2: Human stem cell-derived cardiac tissue after 24 hours of exposure to physioxia conditions.

Movie B.3: Human stem cell-derived cardiac tissue after 24 hours of exposure to hypoxia conditions.

APPENDIX E

LIST OF SUPPLEMENTARY TABLES

Table E.1 Editing efficiencies of C->T conversion of *KCNH2* at bystander and target bases

HEK293 Transfection		
	Bystander C	Target C
US	32.5+/-0.71	0.5+/-0.71
DN	18.5+/-2.12	2.5+/-0.71
BFP ⁺	41 +/-7.07	5.5+/-2.12
BFP ⁺ /GFP ⁺	72.5+/-2.38	6.15+/-2.06
hiPSC Transfection		
	Bystander C	Target C
US	11.5+/-6.24	1+/-0.82
DN	14.25+/-4.86	2+/-0
BFP ⁺	50.25+/-14.17	2.5+/-0.58
BFP ⁺ /GFP ⁺	66.25+/-4.86	4.5+/-2.08

APPENDIX F
COPYRIGHT PERMISSIONS

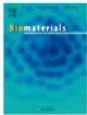
Three-dimensional microengineered models of human cardiac diseases



Author: Jaimeson Veldhuizen et al
Publication: Journal of Biological Engineering
Publisher: Springer Nature
Date: Apr 3, 2019
Copyright © 2019. The Author(s)

Creative Commons

This is an open access article distributed under the terms of the Creative Commons CC BY license, which permits unrestricted use, distribution, and reproduction in any medium, provided the original work is properly cited.
You are not required to obtain permission to reuse this article.
CC0 applies for supplementary material related to this article and attribution is not required.



Engineering anisotropic human stem cell-derived three-dimensional cardiac tissue on-a-chip

Author: jaimeson Veldhuizen,Joshua Cutts,David A. Brafman,Raymond Q. Migrino,Mehdi Nikkhal
Publication: Biomaterials
Publisher: Elsevier
Date: October 2020
© 2020 Elsevier Ltd. All rights reserved.

Journal Author Rights

Please note that, as the author of this Elsevier article, you retain the right to include it in a thesis or dissertation, provided it is not published commercially. Permission is not required, but please ensure that you reference the journal as the original source. For more information on this and on your other retained rights, please visit: <https://www.elsevier.com/about/our-business/policies/copyright#Author-rights>

BACK

CLOSE WINDOW